

**Measurement of Heavy Flavor Yield
and Azimuthal Anisotropy at Forward
Angles in $Cu + Au$ Collisions at a
Center-of-Mass Collision Energy Per
Nucleon of 200 GeV**

A Dissertation Presented for the

Doctor of Philosophy

Degree

The University of Tennessee, Knoxville

Brandon Kyle Schmoll

August 2017

Abstract

Heavy flavor quarks are produced early in heavy ion collisions and will experience the full evolution of the Quark Gluon Plasma (QGP). Measurements at forward rapidity may be influenced as much, or more, by the cold nuclear matter effects as by the hot nuclear matter effects associated with a QGP. As the medium evolves, the initial spatial anisotropy of participants is converted to an azimuthal anisotropy in the momentum space of outgoing particles. Therefore, the momentum spectra modification and anisotropy parameters provide useful information about the heavy quark interaction with the bulk medium.

Asymmetric heavy ion collisions, such as Cu+Au, provide a unique geometry with which to study the dynamics of the heavy quarks, relative to that in symmetric collisions. In particular, asymmetries in the yields between the Cu-going and Au-going directions may help unentangle the so-called cold nuclear matter effects from the hot nuclear matter effects indicative of a QGP. In addition, the parameters v_2 and v_3 may be modified in asymmetric collisions relative to the symmetric collisions due to the unique geometry provided in mid-central Cu+Au collisions.

This dissertation presents the measurement of the yield and azimuthal anisotropy of single muons originating from heavy flavor decays in $\sqrt{s_{NN}}$ [center-of-mass energy per nucleon] = 200 GeV Cu+Au collisions.

Table of Contents

1	Introduction	1
1.1	The Standard Model	1
1.2	Quantum Chromodynamics	4
1.2.1	Perturbative QCD	5
1.2.2	Lattice QCD	7
1.2.3	QCD phase diagram	8
1.3	Relativistic Heavy-Ion Collisions	9
1.3.1	Parton Distribution Functions	10
1.3.2	Thermalization	13
1.3.3	Hadronization	13
1.4	QGP Signatures	14
1.4.1	Nuclear Modification Factor	14
1.4.2	Azimuthal Anisotropy and Hydrodynamic Flow	16
1.5	Heavy Flavor and Hard Probes	21
1.5.1	Factorization	21
1.5.2	Energy Loss	22
1.5.3	Semi-leptonic and Hadronic Decay	24
1.6	Motivation	28
1.6.1	Forward Rapidity Measurements	28
1.6.2	Asymmetric Collisions	30
2	Survey of Previous Experimental Results	31
2.1	Heavy Flavor Spectra	31

2.2	Heavy Flavor Flow	40
3	The PHENIX Experiment	46
3.1	The Relativistic Heavy Ion Collider	46
3.2	PHENIX	48
3.2.1	Central Arms	50
3.2.2	Muon Arms	51
3.2.3	FVTX	56
3.2.4	Global Detectors	57
3.3	Event Classification	58
3.3.1	Centrality	58
3.3.2	Collision Vertex	61
3.3.3	Triggers	62
3.4	Track Reconstruction	62
3.4.1	Tracking in the MuID	62
3.4.2	Tracking in the MuTr	63
3.5	Data Aquisition	64
4	The Single Muon Analysis	67
4.1	Overview	67
4.2	Data Quality Assurance	70
4.3	Narrow Vertex Trigger Efficiency Correction	71
4.4	Matching Data and Monte Carlo	74
4.5	Track Cuts	74
4.5.1	Analysis Variables	76
4.5.2	Analysis Cuts	78
4.6	Background Subtraction	79
4.6.1	Hadron Cocktail	80
4.6.2	Analysis Improvements	88
4.6.3	$p\delta\theta$ Distributions	89
4.7	Acceptance and Efficiency Correction	90

4.8	Heavy Flavor Signal	93
5	Azimuthal Anisotropy	94
5.1	Overview	94
5.2	Event Plane Method	95
5.3	Data Quality Assurance	98
5.4	Fitting Azimuthal Distributions	104
5.5	Hadron Flow	105
5.6	Background Subtraction	107
5.7	Heavy Flavor Flow	109
6	Systematic Errors	111
6.1	Uncertainty in Single Muon Yield	111
6.1.1	Type-B Systematics	112
6.1.2	Type-C Systematics	115
6.2	Uncertainty in Nuclear Modification Factor	116
6.3	Uncertainty in R_{CP}	116
6.4	Uncertainty in Azimuthal Anisotropy	117
7	Results and Discussion	120
7.1	Heavy Flavor Single Muon Spectra	120
7.2	Heavy Flavor Single Muon R_{AA}	123
7.3	Heavy Flavor Single Muon R_{CP}	126
7.4	Heavy Flavor Single Muon v_2	130
7.5	Heavy Flavor Single Muon v_3	131
7.6	Discussion	132
7.6.1	Nuclear Modification Factor R_{AA}	132
7.6.2	v_2	139
8	Summary and Conclusions	141
Bibliography		143

Appendices	150
A Selected Data Tables	151
Vita	156

List of Tables

1.1	Table of Heavy Flavor Meson Decay Lengths.	26
4.1	Simulation matching criteria.	87
6.1	Table of Type B Point-to-Point Systematic Uncertainties in Single Muon Yield, Centrality 0%–20%.	112
6.2	Table of Type C Global Systematic Uncertainties in Single Muon Yield.	112
6.3	Table of Systematic Uncertainties in R_{AA}	116
6.4	Table of Systematic Uncertainty in Azimuthal Anisotropy.	117
A.1	Table for Figure 7.1 (centrality 0%–20%)	152
A.2	Table for Figure 7.2 (centrality 20%–40%)	153
A.3	Table for Figure 7.3 (centrality 40%–60%)	154
A.4	Table for Figure 7.4 (centrality 60%–100%)	155

List of Figures

1.1	Fundamental particles of The Standard Model [27].	3
1.2	QCD coupling as a function of momentum transfer [16].	6
1.3	Energy density over T^4 as a function of T in units of the phase transition temperature, T_C . The steep increase represents an opening of degrees of freedom indicating a transition to a phase of deconfinement [34].	7
1.4	QCD phase diagram [18].	8
1.5	Stages of a heavy ion collisions [57].	10
1.6	Parton distribution functions for up quarks, down quarks, sea quarks, and gluons. The x-axis, x, is the momentum fraction and the y-axis, xf, is the product of the momentum fraction and parton distribution function, f [47].	12
1.7	Nuclear parton distribution functions. The left panel shows the Nuclear PDF for valence quarks. The middle panel shows the Nuclear PDF for sea quarks. The right panel shows the Nuclear PDF for gluons [35].	12
1.8	Nuclear modification factor R_{AA} for direct photons and π_0 as a function of N_{part} [12].	16
1.9	Collision geometry.	17
1.10	Fourier coefficients [3].	18
1.11	Diagram of pressure gradient equipotentials.	19
1.12	Quark scaling of azimuthal anisotropy [9].	20
1.13	Nuclear modification factor and elliptic flow measurements for neutral pions and heavy flavor electrons [10].	20

1.14 Upper plot: invariant differential cross sections of electrons from heavy-flavor decays [26]. The error bars (bands) represent the statistical (systematic) errors. The curves are FONLL calculations. Lower plot: ratio of the data to the FONLL calculation. The upper and lower curves represent the upper and lower limits of the FONLL uncertainty band. An overall normalization uncertainty of 10% is not shown [22].	23
1.15 Nuclear modification factor R_{AA} for heavy flavor single muons in Cu+Cu collisions [11].	24
1.16 Heavy Flavor Decay [31].	25
1.17 Pythia study of correlations of decay muons to their parent mesons [52].	27
1.18 Distribution of logarithm of momentum fraction x values in the north and south arm [56].	29
1.19 Illustration depicting a peripheral Cu+Au collision [1].	30
2.1 Charm cross section measured in p+p collisions at 200 GeV [53]. The PYTHIA prediction is represented by the dotted line. A FONLL calculation is also plotted, represented by the black line with the yellow band representing systematics. The x-axis starts at 1 GeV with 500 MeV intervals.	32
2.2 Charm cross section measured in p+p collisions at 200 GeV [11].	33
2.3 Nuclear modification factor as a function of N_{part} . The red points are the measurement published in PPG117, while the blue points are the nuclear modification factor for single electrons in Au+Au collisions [11].	33
2.4 The nuclear modification factor R_{dA} , for negatively charged heavy-flavor muons in d+Au collisions for the (a) 60%–88%, (b) 0%–20%, and (c) 0%–100% most central collisions. The black boxes on the right side indicate the global scaling uncertainty. The red dashed (blue solid) lines in each panel are calculations at forward (backward) rapidity based on the EPS09s nPDF set [6].	35
2.5 R_{AA} of heavy-flavor electrons as a function of N_{coll} in various collision systems [5].	36

2.6	R_{AA} versus p_T (left) and y (right) for J/ψ production in the most central Cu+Cu collisions [23].	37
2.7	R_{AA} versus N_{part} for J/ψ production in Cu+Cu and Au+Au collisions. (c) Forward/mid-rapidity R_{AA} ratio. The curves are predictions from ad-hoc fits to d+Au data [23].	38
2.8	The nuclear modification factor R_{dA} for J/ψ and heavy-flavor muons for the 0%–20% centrality class. The global systematic uncertainty on each distribution is shown as a percentage in the legend [6].	39
2.9	Nuclear modification factor, R_{AA} , measured as a function of collision centrality (N_{part}). Values for J/ψ at forward (Cu-going) rapidity are shown as open circles and at backward (Au- going) rapidity as closed circles. For reference, Au+Au data are also shown, averaged over forward and backward rapidities, as red squares [24].	40
2.10	Comparison of heavy flavor single electron v_2 with various theoretical models [21].	41
2.11	Comparison of heavy flavor single electron v_2 with a model calculation from Gossiaux and Aichelin [21].	42
2.12	Measured v_2 for D0 compared to that of light hadrons [37].	42
2.13	The second-order Fourier coefficients v_2 for charged hadrons is shown as a function of pT . Cu+Cu data points plotted in green, Cu+Au is in red, and Au+Au is blue. Statistical uncertainty is plotted with bars and systematic uncertainty with shaded boxes. The top left panel shows the 0-10% centrality interval and subsequent panels show increasingly peripheral collisions in 10% intervals [51].	44
2.14	In each panel, the $v_3(p_T)$ coefficients are compared for the same centrality class, as marked in the figure. The symbols represent the measured $v_3(p_T)$ values, the uncertainty bars show the statistical uncertainties, and the shaded boxes indicate the systematic uncertainties for Cu+Au. The blue bounding lines show the systematic uncertainties for the Au+Au measurement. Cu+Au is represented with red data points and Au+Au with blue [51].	44

2.15 p_T -differential elliptic flow of muons from heavy-flavour decays, v_{HF} , in $2.5 < y < 4$ and various centrality intervals, in Pb+Pb collisions at $s_{NN} = 2.76$ TeV. The symbols are placed at the centre of the p_T interval and, for visibility, the points from two-particle Q cumulants and Lee-Yang zeros with product generating function are shifted horizontally [19].	45
3.1 Aerial view of RHIC.	47
3.2 A cut-away view of the PHENIX detector [25].	48
3.3 Phenix coordinate system.	49
3.4 Beam line view illustration of the PHENIX central arms circa 2012.	50
3.5 Elevation view illustration of the PHENIX muon arms circa 2012.	51
3.6 Close-up view of two octants of cathode strips before installation.	52
3.7 MuTr schematic diagram showing the position of the stations with respect to the interaction point and the beam line.	53
3.8 A MuID two-pack.	54
3.9 MuID panels.	55
3.10 Integrated interaction length as a function of distance from interaction point [28].	56
3.11 An illustration depicting the participants and spectators of a heavy ion collision. The participants remain mostly in the interaction region as they interact, while the spectators continue along the z-axis [32].	58
3.12 Charge density distributions for nuclei used at RHIC [40].	59
3.13 A plot showing a charged particle multiplicity distribution with various illustrations depicting the centrality of collisions. Peripheral collisions are more common, hence the rise in final-state yield for decreasing centrality [40].	60
3.14 Z-vertex distribution in the run 12 Cu+Au data set.	61
3.15 Illustrated depiction of a track within the MuTr. The blue lines represent cathode strips within an octant of each station [31].	64
3.16 An illustration depicting the flow of data from the detectors to permanent storage on tape [57].	65

4.1	Illustrated schematic depicting the different components of the inclusive yield [57].	69
4.2	Tracks per event versus run number for Run-12.	70
4.3	Collision rate versus run number for Run-12.	71
4.4	Event z_{vtx} distributions for various centralities. The distributions show an increasing shift away from zero for increasingly central collisions [4].	72
4.5	Corrected (blue) and uncorrected (red) event z_{vtx} distributions for centrality 0-20%.	73
4.6	Corrected (blue) and uncorrected (red) event z_{vtx} distributions for centrality 20-40%.	73
4.7	Rapidity distributions for Monte Carlo (red) and data (blue). The plots are ordered from left to right by the tracks last gap (2,3,4). The top panels show the south arm and the bottom panels show the north arm.	74
4.8	p_z distributions for Monte Carlo (red) and data (blue) in ascending ordered p_T bins.	75
4.9	Phi distributions for Monte Carlo (red) and data (blue) in the north arm. Note the missing octant. The Monte Carlo shown here was injected with a non-zero v_2 . The red points over estimate the data at $\phi = 0, \pi$ and under estimate the data at $\phi = \pi/2, 3\pi/2$ due to the injected v_2	75
4.10	Illustration of the $p\delta\theta$ variable [31].	76
4.11	Illustration of the r_{ref} variable [11].	77
4.12	Illustration of the $DG0$ and $DDG0$ variables [11].	78
4.13	Distribution of transverse momentum versus pseudorapidity for π^+ in cocktail input.	80
4.14	Longitudinal momentum distribution, p_Z , for data and simulation in MuID Gap 3 of the south arm.	81
4.15	Gap 3 yields for Monte Carlo (open) and data (closed) (centrality 20-40 %). The bottom panel shows the data over simulation fraction.	83
4.16	Gap 2 yields for Monte Carlo (open) and data (closed) (centrality 20-40 %). The bottom panel shows the data over simulation fraction.	83

4.17	Gap 4 south slopes for Monte Carlo (red) and data (black) (centrality 20-40 %).	85
4.18	Gap 4 north slopes for Monte Carlo (red) and data (black) (centrality 20-40 %).	85
4.19	Acceptance times efficiency correction in the south arm.	91
4.20	Acceptance times efficiency correction in the south arm.	91
4.21	Tracks-per-event percent drop in the south arm between part A and part B of the Cu+Au run.	92
4.22	Tracks-per-event percent drop in the north arm between part A and part B of the Cu+Au run.	92
4.23	Heavy flavor signal, uncorrected for acceptance and efficiency.	93
5.1	FVTX south dead map for run 373139.	99
5.2	FVTX north dead map for run 373139.	99
5.3	FVTX raw versus calibrated event plane distributions for run 373139, segment 5 [43].	100
5.4	FVTX event plane QA plot for a good run (left) and a bad run (right).	101
5.5	χ^2/NDF versus run number for FVTX South (left) and FVTX North (right).	102
5.6	χ^2/NDF distributions for FVTX South.	103
5.7	χ^2/NDF distributions for FVTX North.	103
5.8	$\phi - \Psi$ fits for different pT bins, Gap 4 North, EP: FVTX S, centrality 10%-15%.	104
5.9	$\phi - \Psi$ fits for different pT bins, Gap 4 South, EP: FVTX N, centrality 10%-15%.	105
5.10	Momentum distribution of v_2 for Gap 2 and Gap 3 tracks, South Arm.	106
5.11	Momentum distribution of v_2 for Gap 2 and Gap 3 tracks, North Arm.	106
5.12	Momentum distribution of v_2 for Decay Muons and Punchthrough Tracks in Gap 2 and Gap 3, South Arm centrality 20%-40%.	108
5.13	Momentum distribution of v_2 for Decay Muons and Punchthrough Tracks in Gap 2 and Gap 3, North Arm centrality 20%-40%.	108
5.14	Momentum distribution of v_2 for input and reconstructed distributions of tracks, South Arm (left) and North Arm (right) centrality 20%-40%.	109

5.15 Momentum distribution of v_2 for Gap2+3 and Gap 4 tracks, South arm (left) adn North arm (right) centrality 20%–40%	110
5.16 Heavy Flavor Single Muon v_2 , South arm (left) and North arm (right) centrality 20%–40%	110
6.1 Tuned cocktail using different reweighting parameters in the south arm. Open points are made using a relative ratio of 1:1:1 for parameters a:b:c. The closed points use a relative ratio of 1:1:2 for parameters a:b:c. The ratio in the bottom panel is the closed points divided by the open points.	113
6.2 Tuned cocktail using different reweighting parameters in the north arm. Open points are made using a relative ratio of 1:1:1 for parameters a:b:c. The closed points use a relative ratio of 1:1:2 for parameters a:b:c. The ratio in the bottom panel is the closed points divided by the open points.	114
6.3 Momentum distribution of v_2 using BBC and FVTX event planes, South arm.	118
6.4 Momentum distribution of v_2 using BBC and FVTX event planes, North arm.	118
6.5 The left hand panel shows v_2 before the correction is applied. The right hand panel shows the corrected v_2 . [49]	119
7.1 Heavy flavor single muon invariant differential yields for south (black) and north (red) arms (Centrality 0-20%). Error bars represent the Type-A statistical uncertainty. Error bands represent the Type-B systematic uncertainty. A Type-C global uncertainty of $\approx 15\%$ underlays the measurement.	121
7.2 Heavy flavor single muon invariant differential yields for south (black) and north (red) arms (Centrality 20-40%). Error bars represent the Type-A statistical uncertainty. Error bands represent the Type-B systematic uncertainty. A Type-C global uncertainty of $\approx 15\%$ underlays the measurement.	121
7.3 Heavy flavor single muon invariant differential yields for south (black) and north (red) arms (Centrality 40-60%). Error bars represent the Type-A statistical uncertainty. Error bands represent the Type-B systematic uncertainty. A Type-C global uncertainty of $\approx 15\%$ underlays the measurement.	122

7.4 Heavy flavor single muon invariant differential yields for south (black) and north (red) arms (Centrality 60-93%). Error bars represent the Type-A statistical uncertainty. Error bands represent the Type-B systematic uncertainty. A Type-C global uncertainty of $\approx 15\%$ underlays the measurement.	123
7.5 Heavy flavor single muon R_{AA} for south (black) and north (red) arms (Centrality 0-20%). Error bars represent the Type-A statistical uncertainty. Error bands represent the Type-B systematic uncertainty. A Type-C global uncertainty of $\approx 15\%$ (from the HF yield) and an uncertainty of $\approx 9\%$ due to the statistical fluctuations in N_{coll} underlay the measurement (indicated in legend).	124
7.6 Heavy flavor single muon R_{AA} for south (black) and north (red) arms (Centrality 20-40%). Error bars represent the Type-A statistical uncertainty. Error bands represent the Type-B systematic uncertainty. A Type-C global uncertainty of $\approx 15\%$ (from the HF yield) and an uncertainty of $\approx 10\%$ due to the statistical fluctuations in N_{coll} underlay the measurement (indicated in legend).	124
7.7 Heavy flavor single muon R_{AA} for south (black) and north (red) arms (Centrality 40-60%). Error bars represent the Type-A statistical uncertainty. Error bands represent the Type-B systematic uncertainty. A Type-C global uncertainty of $\approx 15\%$ (from the HF yield) and an uncertainty of $\approx 12\%$ due to the statistical fluctuations in N_{coll} underlay the measurement (indicated in legend).	125
7.8 Heavy flavor single muon R_{AA} for south (black) and north (red) arms (Centrality 60-93%). Error bars represent the Type-A statistical uncertainty. Error bands represent the Type-B systematic uncertainty. A Type-C global uncertainty of $\approx 15\%$ (from the HF yield) and an uncertainty of $\approx 19\%$ due to the statistical fluctuations in N_{coll} underlay the measurement (indicated in legend).	125

7.9 Heavy flavor single muon R_{CP} for south (black) and north (red) arms (Centrality 0-20%). Error bars represent the Type-A statistical uncertainty. Error bands represent the Type-B systematic uncertainty. A Type-C global uncertainty of $\approx 20\%$ due to the statistical fluctuations in N_{coll} underlay the measurement (indicated in legend).	126
7.10 Heavy flavor single muon R_{CP} for south (black) and north (red) arms (Centrality 20-40%). Error bars represent the Type-A statistical uncertainty. Error bands represent the Type-B systematic uncertainty. A Type-C global uncertainty of $\approx 21\%$ due to the statistical fluctuations in N_{coll} underlay the measurement (indicated in legend).	127
7.11 Heavy flavor single muon R_{CP} for south (black) and north (red) arms (Centrality 40-60%). Error bars represent the Type-A statistical uncertainty. Error bands represent the Type-B systematic uncertainty. A Type-C global uncertainty of $\approx 23\%$ due to the statistical fluctuations in N_{coll} underlay the measurement (indicated in legend).	127
7.12 Ratio of $R_{CP}(\text{Cu-going})$ to $R_{CP}(\text{Au-going})$ (centrality 0%-20%).	128
7.13 Ratio of $R_{CP}(\text{Cu-going})$ to $R_{CP}(\text{Au-going})$ (centrality 20%-40%).	128
7.14 Ratio of $R_{AA}(\text{Cu-going})$ to $R_{AA}(\text{Au-going})$ (centrality 0%-20%).	129
7.15 Ratio of $R_{AA}(\text{Cu-going})$ to $R_{AA}(\text{Au-going})$ (centrality 20%-40%).	129
7.16 Heavy flavor single muon v_2 for the Au-going (left) and Cu-going (right) directions (centrality 20%-40%). Error bars represent the Type-A statistical uncertainty. Error bands represent the Type-B systematic uncertainty.	130
7.17 Heavy flavor single muon v_3 for the Au-going (left) and Cu-going (right) directions (centrality 20%-40%). Error bars represent the Type-A statistical uncertainty. Error bands represent the Type-B systematic uncertainty.	131
7.18 Heavy flavor single muon R_{AA} for south (black) and north (red) arms (centrality 0%-20%). The green points are results for heavy flavor muon production at forward rapidity in Cu+Cu collisions [11].	133

7.19 Heavy flavor single muon R_{AA} for south (black) and north (red) arms (centrality 0%–20%). The blue points are results for heavy flavor electron production at mid-rapidity in Cu+Cu collisions [7].	133
7.20 Heavy flavor single muon R_{AA} for Au-going (black) and Cu-going (red) directions (centrality 20%–40%). The green points are results for heavy flavor muon production at forward rapidity in Cu+Cu collisions [11].	134
7.21 Heavy flavor single muon R_{AA} for Au-going (black) and Cu-going (red) directions (centrality 20%–40%). The blue points are results for heavy flavor electron production at mid-rapidity in Cu+Cu collisions [7].	134
7.22 Illustration of the $Bjorken - x$ regions of colliding partons within their respective nuclei [2].	136
7.23 Heavy flavor single muon R_{AA} for Au-going (black) and Cu-going (red) directions (centrality 20%–40%). The green (Au-going) and blue (Cu-going) points are results for ϕ meson production at forward rapidity in Cu+Au collisions.	138
7.24 Nuclear modification for the single non-photonic electrons in central Au+Au and Cu+Cu collisions at RHIC. Data is from PHENIX and STAR collaborations [48].	139
7.25 pT-differential elliptic flow of muons from heavy-flavour decays in $2.5 < y < 4$ [19].	140
7.26 Hadron v_2 (blue) for the Au-going (left) and Cu-going (right) directions (centrality 20%–40%) and previous PHENIX combined-arms analysis (red). Error bars represent the Type-A statistical uncertainty. Error bands represent the Type-B systematic uncertainty.	140

Chapter 1

Introduction

1.1 The Standard Model

The currently well-accepted theory of matter and its interactions in the Universe is known as *The Standard Model*. The Standard Model describes three of the four known forces, excluding the *gravitational force* which is covered by Albert Einstein's *General Theory of Relativity*. The *electromagnetic force* is well known and its effects are apparent in everyday life. It is the reason why matter doesn't simply pass right through itself, an example being a basketball hitting the floor and bouncing back instead of falling to the center of the Earth (thanks to gravity). Indeed, it is the force which is responsible for the common states of matter (on Earth), *solid*, *liquid*, and *gaseous*, as well as the less common *electromagnetic plasma*. Likewise, it is responsible for the phase transitions between these states. The interactions of the lesser known forces, the *weak nuclear force* and the *strong nuclear force*, are not as obvious. Their effects are restricted to very short distances, on the order of 10^{-15} meters. Nevertheless, they play an equally important role in the construction and evolution of the Universe as we know it. The weak force is responsible for all beta decays observed in the Universe. It is the source of proton-proton fusion, the main mechanism by which stars produce energy. Much, if not all, of life on Earth has developed by using energy from the Sun. In this way, the weak force has a crucial role in the genesis of life on Earth. The strong force is equally involved in the emergence of life. The strong force is responsible for the stability of nuclei. The stability of heavy elements such as carbon (the basis of all known

life) is necessary for complex carbon based life forms to exist. It is not only the existence of these three forces (as well as gravity) that leads to a Universe like the one we live in. The intricate way in which matter and the forces of nature interact is essential to the current structure of reality.

The Standard Model is a quantum field theory based on the $SU(3)\times SU(2)\times U(1)$ gauge group. It is a rather robust theory based on a few assumptions about symmetries observed in nature. One fundamental requirement of The Standard Model is that of *gauge invariance*. Gauge invariance refers to the invariance of the Lagrangian under certain types of transformations. In particular, the Lagrangian can undergo any transformation that leaves the equations of motion invariant. These transformations are referred to as *gauge transformations*. The requirement of gauge invariance of The Standard Model necessitates massless fields in the Lagrangian. For example, $U(1)$ requires a single massless field. Similarly, $SU(2)$ requires three massless fields while $SU(3)$ requires eight massless fields. Actually, it is even more complicated than that, as the massless fields associated with $SU(2)\times U(1)$ interact with another field, known as the Higgs, which give three of them mass, leaving one massless. That, however, is not part of the scope of this thesis. Collectively, the carriers of these fields are known as the *gauge bosons*.

The fundamental particles (fields) of The Standard Model are *fermions* (*leptons* and *quarks*) and gauge bosons. The leptons and quarks make up the matter in the Universe, while the gauge bosons mediate the interactions between this matter. They are classified by their various charges. The electromagnetic force governs interactions between *electrically charged* particles. It is described by the theory of Quantum Electrodynamics (QED). The mediator of the electromagnetic force is the massless *photon*, which does not carry electric charge. The weak force governs interactions between all quarks and leptons. This interaction has its own conserved charge, the *weak isospin*. The mediators are the massive weak bosons, the electrically charged W and the electrically neutral Z. Together, these two forces make up what is called the *Electroweak Force*, represented by the $SU(2)\times U(1)$ gauge group.

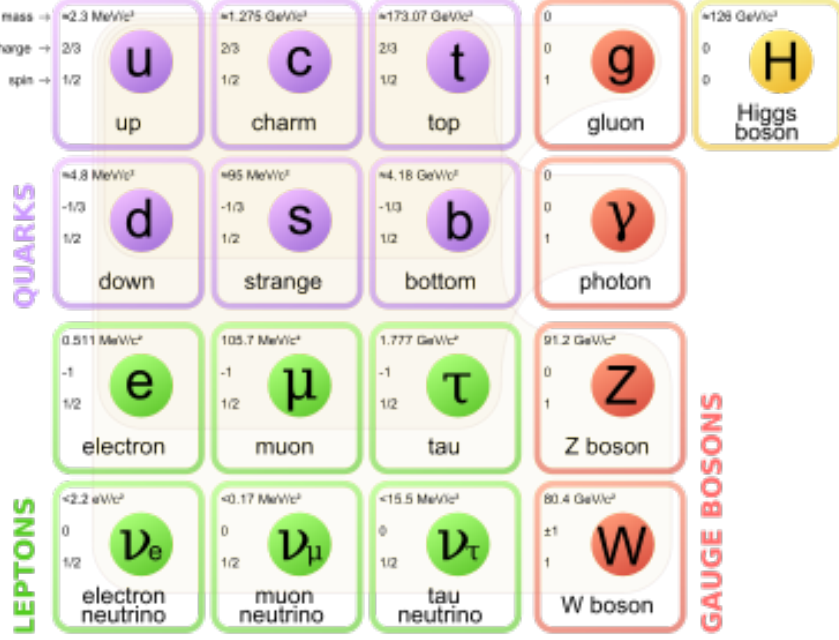


Figure 1.1: Fundamental particles of The Standard Model [27].

The strong force is described by the theory of Quantum Chromodynamics (QCD), represented by the $SU(3)$ gauge group. It governs the interactions between *colored* particles. *Color* is a property of quarks and gluons, analogous to the electric charge of the electromagnetic force. In the case of strong interactions, there are three color charges (red, blue, and green) and eight mediators, the gluons. The required gauge invariance of QCD means the gluons carry color and participate in the same interaction they mediate. This leads to gluon-gluon interactions, of which there is no analogy in QED, meaning QCD is a non-abelian theory. For this reason, calculations of strong processes are more complicated than calculations of, e.g., electromagnetic processes. However, methods have been developed to perform calculations under certain constraints.

The quarks and leptons are further classified by a property known as *flavor* (see Figure 1.1). Quarks are described by quark flavor and, naturally, leptons by lepton flavor. Each quark flavor has a different mass and a different flavor quantum number. A given quark's corresponding anti-quark will have the same flavor quantum number with opposite sign. That is, a charm quark has charm of 1, while a charm anti-quark has charm of -1. Flavor is a property of quarks which is conserved in strong interactions but not in weak interactions. This means that in a strong interaction, any particular flavor quantum number must be

conserved. If a charm quark is created via the strong interaction, a charm anti-quark must also have been created. Weak interactions, on the other hand, do not conserve flavor quantum numbers. So quarks of a particular flavor can decay into lighter quarks of a different flavor via the weak interaction. In this dissertation, the term *Heavy Flavor* will refer to charm and bottom quarks. While top quarks are indeed heavy, they are not created in any significant abundance at the energies we will discuss.

The prediction of the existence of quarks owes its inception to Murray Gell-Mann, as well as many others. In the 1950's, experiments revealed the existence of hadrons which exhibited a seemingly new quantum number, *strangeness*. In Gell-Mann's attempts to understand and describe strangeness and hadron dynamics in general, he eventually postulated that hadrons were not elementary particles. Instead, hadrons were composite particles made up of quarks. The existence of quarks had been suggested by a number of different measurements. Robert Hofstadter won a Nobel prize in 1961 for his elastic scattering experiments, which showed that the proton is not a point particle, but instead has finite size [14]. Friedman, Kendall, and Taylor won a Nobel prize in 1990 for their work on deep inelastic scattering [44]. Their experiments at SLAC showed that the proton was indeed a composite structure, and furthermore, that the components were point like particles. This is considered the first experimental evidence for quarks. At this time, there were only three proposed quarks, the up, down, and strange quarks. Since then, three more quarks have been discovered, the charm (1974), bottom (1977), and top (1995) quarks.

1.2 Quantum Chromodynamics

Research in the field of Relativistic Heavy Ion Physics is dedicated to further study and confirmation of the predictions of Quantum Chromodynamics, the theory of strong interactions. QCD's principles of *asymptotic freedom* and *confinement* are central to this research. These concepts emerge from the non-abelian gluon-gluon interactions discussed previously. The running coupling constant, α_s , which describes the strength of the strong interaction is inversely proportional to the energy scale of a given interaction. Therefore, at high momentum transfer (Q^2) the strong interaction gets weaker. This is known as

asymptotic freedom. In this limit, we can renormalize the theory in order to cope with the non-linearities which make calculations so difficult. Perturbation methods can be used, if the coupling constant is small enough, to accurately calculate physical observables within the context of QCD. Conversely, for low momentum transfer the coupling constant is large. In this case the colored particles are bound inside color neutral objects called *hadrons*. This phenomenon is referred to as confinement. At these low energies, perturbation methods are ineffective. Alternatively, calculations can be done on a discrete space-time lattice. Therefore, in our field, we aim to observe interactions between matter at very high energies and that take place over very short distances, so that the colored quarks are *deconfined*. In this case we have a novel phase of matter, which will be discussed in the next section, called the *Quark-Gluon Plasma* (QGP). Experimental measurements of the QGP are compared to predictions of both perturbative QCD and lattice QCD in an attempt to distinguish between various theories.

1.2.1 Perturbative QCD

The energy dependence of the coupling constant, α_s , is given by the β -function such that

$$Q^2 \frac{\delta \alpha_s(Q^2)}{\delta(Q^2)} = -\beta_0 \alpha_s^2(Q^2) - \beta_1 \alpha_s^3(Q^2) - \beta_2 \alpha_s^4(Q^2) - \beta_3 \alpha_s^5(Q^2) + \mathcal{O}(\alpha_s^6(Q^2)) \quad (1.1)$$

with the β -constants proportional to the number of quark flavors that are active at the momentum scale, Q^2 , as well as the SU(3) group constants, C_F and C_A [16]. This differential equation can be solved numerically provided α_s is known at a particular reference scale, commonly taken to be the mass of the Z-boson. This reference is measured by fitting to data taken in a variety of different experiments, including deep inelastic scattering, electron-positron annihilation, as well as others. The solution is made up of increasing powers of

$$\frac{1}{\ln Q^2/\Lambda^2} \quad (1.2)$$

where Λ defines the scale at which α_s diverges. Figure 1.2 shows measurements of the energy dependence of α_s [16]. The distributions are calculated using the world average measured value of $\alpha_s(M_Z)$ and solving equation 1.1 neglecting terms of order $\alpha_s^6(Q^2)$ and higher.

For small values of the coupling constant, α_s , perturbative QCD can be used to make realistic predictions which can be compared with experimental measurements. Feynman diagrams used to calculate the cross section for a given process will include a factor of α_s for every vertex in the diagram.

$$\sigma_{QCD} = \sum_{n=1}^{\infty} C_n \alpha_s^n \quad (1.3)$$

If α_s is sufficiently small, $\alpha_s \ll 1$, then higher order diagrams will include many factors of α_s and all but the lowest order diagrams will be suppressed. Higher order diagrams can be disregarded, however, the number of diagrams that are disregarded determines the extent to which the calculation reflects reality.

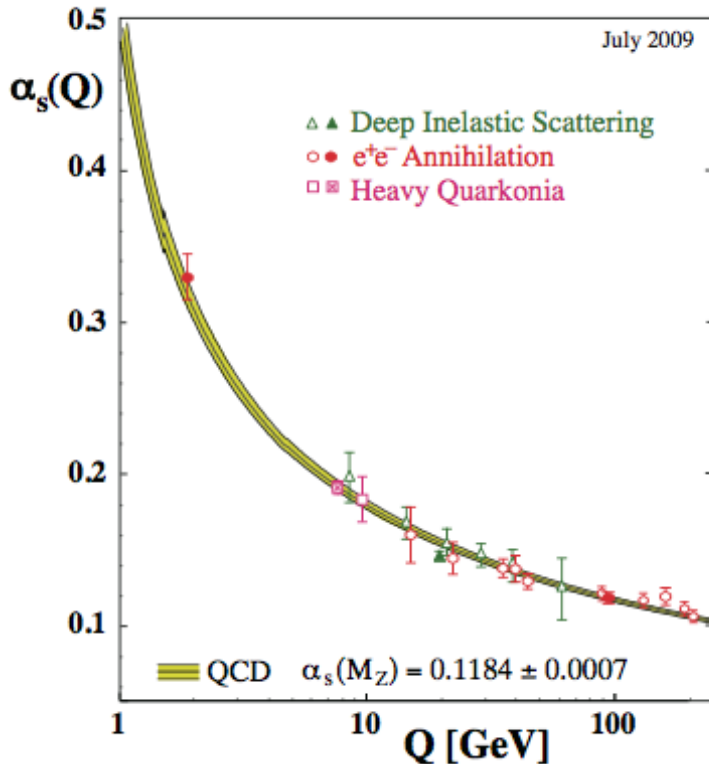


Figure 1.2: QCD coupling as a function of momentum transfer [16].

1.2.2 Lattice QCD

For low values of Q^2 , α_s becomes large such that higher order terms in α_s give larger and larger values. In this case, the expansion cannot be truncated in any meaningful way, and perturbative QCD is not useful. Lattice QCD aims to do low energy calculations on a discrete lattice, with grid points representing quarks and the lines connecting them representing gluons. The lattice method allows computational calculations to be done below an energy scale which is inversely proportional to the lattice spacing [45].

Lattice calculations are used to predict the transition temperature from hadronic matter to deconfined quark matter. Figure 1.3 shows the energy density over T^4 as a function of temperature in units of the phase transition temperature [34]. The steep rise at $T/T_C = 1$ indicates an activation of new degrees of freedom not available below the transition temperature. The various curves represent calculations done with 2 light quark flavors, 2 light quark flavors and 1 flavor with temperature dependent quark mass, and 3 light quark flavors, respectively.

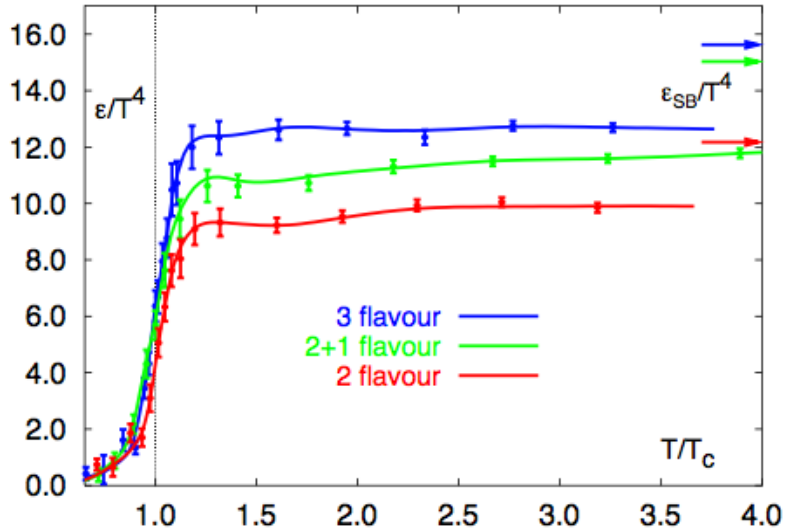


Figure 1.3: Energy density over T^4 as a function of T in units of the phase transition temperature, T_C . The steep increase represents an opening of degrees of freedom indicating a transition to a phase of deconfinement [34].

1.2.3 QCD phase diagram

At low temperature, such as those found on Earth, quarks and gluons are constituents of what is called *nuclear matter*. They make up the protons and neutrons that comprise atomic nuclei in the matter found around us. Figure 1.4 shows a phase diagram of QCD matter [18]. Cold nuclear matter can be found on the x-axis at zero temperature. As temperature is increased, nuclear matter becomes a hadron gas. Atomic nuclei are no longer bound together. When the temperature reaches the pion mass, around 135 MeV, pions are starting to be created and exchanged in the hadron gas. Eventually, the temperature is too high for even the hadrons to stay bound together. At this point, quarks and gluons form a different type of matter, the Quark-Gluon Plasma. This is analogous to an electromagnetic plasma, where electrons are no longer bound to nuclei. Instead, the mean free path of an electron in an electromagnetic plasma is larger than the typical size of an atom, and so it no longer makes sense to discuss the matter in terms of atoms. In a QGP, the mean free path of the quarks and gluons is larger than the typical size of a hadron, and it no longer makes sense to talk about the dynamics of this matter in terms of hadrons. This activation of new partonic degrees of freedom is due to the asymptotic freedom discussed previously.

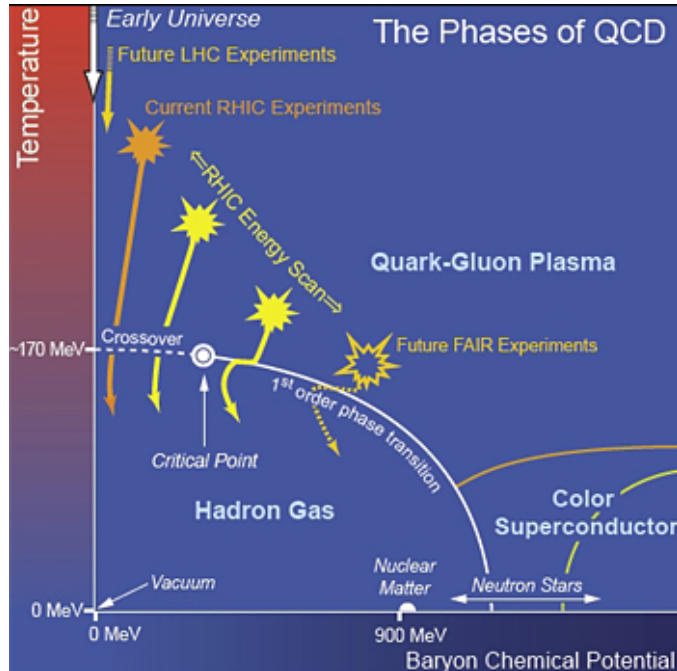


Figure 1.4: QCD phase diagram [18].

The deconfined QCD matter can be realized at high temperatures, such as in the early stages of the Universe, or at high baryon chemical potential, μ_B , which is hypothesized to be the case in the center of neutron stars. While we do not have direct access to neutron stars and current experiments in astrophysics are not sensitive to these early stages of the Universe, there is another way to reach the high temperatures necessary to transition to the QGP phase. This is through relativistic heavy ion collisions. These collisions deposit a large amount of energy into a very small volume, leading to previously unattainable temperatures. Lattice calculations predict a transition from hadron gas to QGP at approximately $T_c = 170\text{ MeV}$ for low quark baryon chemical potential. In this region, the transition is known as a crossover, indicating a rapid but continuous change in the equation of state. There is numerical evidence that a critical point exists at finite baryon chemical potential along the boundary between the hadron gas and the QGP [34]. The trajectory of the system starts on the x-axis of Figure 1.4, in the area labeled nuclear matter. Particles and anti-particles are produced in large quantities, with a one-to-one ratio. In this case, the trajectory follows an increase in temperature and a decrease in baryon chemical potential. The question of whether the transition from hadron gas to QGP is a first or second-order phase transition or a crossover is still an open problem within the field.

1.3 Relativistic Heavy-Ion Collisions

The initial state of the collision system (prior to the collision) consists of two nuclei approaching each other at relativistic energies. The nuclei are Lorentz contracted as a result of their velocities. Similarly, their time evolution relative to observers is affected by time dilation. In general, the collisions will not be direct head-on collisions. Instead, they will collide with some impact parameter, b . The colliding nucleons are referred to as participants, while the rest of the nucleons which do not collide are known as spectators. The collision system will then evolve through a series of stages before final state particles are detected in our detectors, as shown in Figure 1.5 [57].

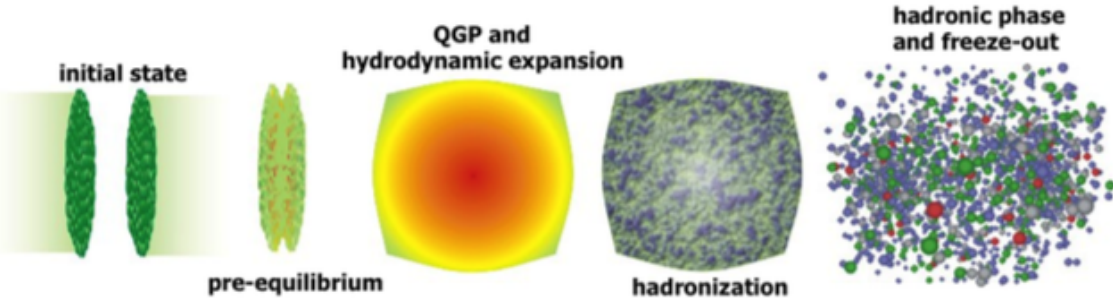


Figure 1.5: Stages of a heavy ion collisions [57].

The initial state geometry of the colliding nuclei is relevant to the subsequent evolution of the hot QCD matter. There are a number of ways to describe the intial state of the colliding nucleons within the nuclei. Currently, the most common description is via the Glauber model [40]. This model treats the nuclei as two colliding bags of hard spheres. Each sphere represents a nucleon. In any particular collision, the arrangement of nucleons will be different. The dynamics within the high energy nuclei are relevant to the subsequent collision system. Of particular interest is the so-called Color-Glass Condensate (CGC). In the center-of-mass frame, the gluons within the nucleons will be confined to the Lorentz contracted length scales of the nucleus, while the time evolution of the gluons is expanded relative to stationary observers due to the time dilation of the ultra-relativistic nuclei. The density of gluons increases with beam energy [39]. This leads to the concept of the CGC, a high density of colored gluons which evolve on long time scales. In this model, the colliding nuclei are treated as colored walls of gluons. The saturation of the gluons may be anisotropic. This anisotropy will have an effect on the initial geometry of the deposited energy and, subsequently, the evolution of the QGP.

1.3.1 Parton Distribution Functions

The dynamics of the colliding nuclei prior to the collision will influence the measured final state distributions. Effects due to the initial state of the nuclei are referred to as cold nuclear matter effects. In contrast, hot nuclear matter effects refer to phenomena attributed to the existence of a QGP. A complete understanding of the QGP and its properties requires separating the cold effects from the hot.

A necessary input for many theoretical calculations is the initial momentum distribution of partons within a given nucleon. This is given by the *parton distribution function (PDF)*. The parton distribution function, $f_i(x, Q^2)$, gives the probability to find a parton, i , with momentum fraction, x , within a proton. Q^2 denotes the momentum transfer of the interaction. Due to the low relative momenta between partons within a nucleon, the PDF's are not calculable within the pQCD framework. They must be determined experimentally in deep inelastic scattering experiments, or via phenomenological models. Figure 1.6 shows the parton distribution functions for partons in a proton-proton collision, as measured by HERA [47]. Note that the gluon curve (and the sea quark curve) has been scaled down by a factor of 20.

The PDF's for nucleons within a heavy nucleus are modified, and exhibit a number of features relevant to the QGP observables. Figure 1.7 shows the ratio of nuclear PDF's for lead nuclei to the PDF's for protons [35]. These functions are determined by parameterizing their shape and fitting to data. The suppression at low x is referred to as *shadowing*. Accordingly, the region of enhancement at intermediate x is due to *anti-shadowing*. Shadowing (and anti-shadowing) is an example of a cold nuclear matter effect. In the next section, a selection of observables used as QGP signatures will be discussed. The claim that a QGP has been created necessitates an understanding of how the initial state affects these observables. At RHIC, light nuclei are collided with heavy nuclei in an attempt to disentangle the cold nuclear matter effects from the hot.

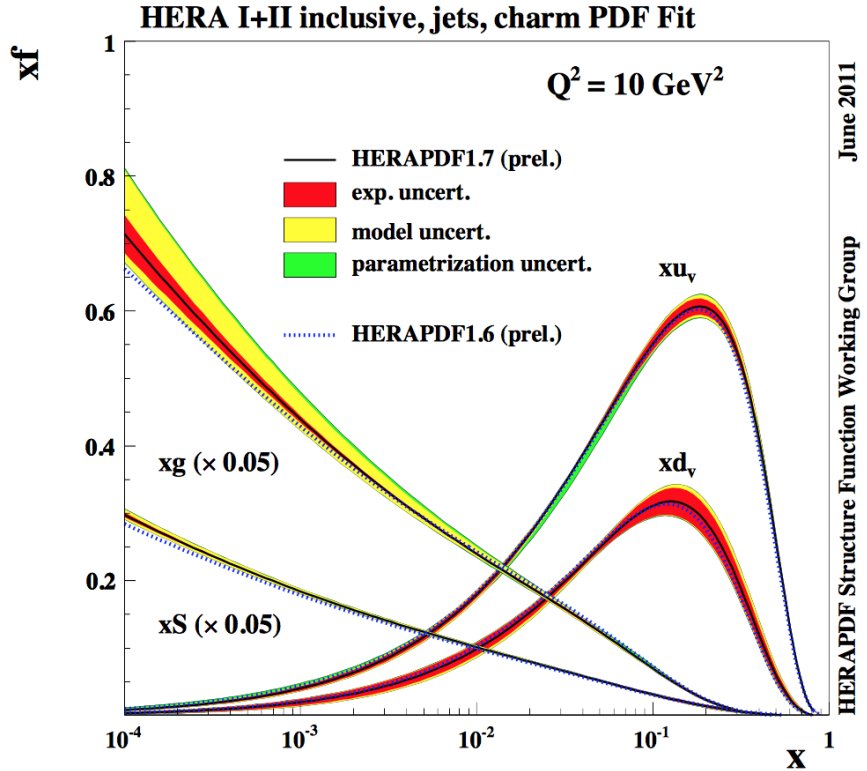


Figure 1.6: Parton distribution functions for up quarks, down quarks, sea quarks, and gluons. The x-axis, x , is the momentum fraction and the y-axis, xf , is the product of the momentum fraction and parton distribution function, f [47].

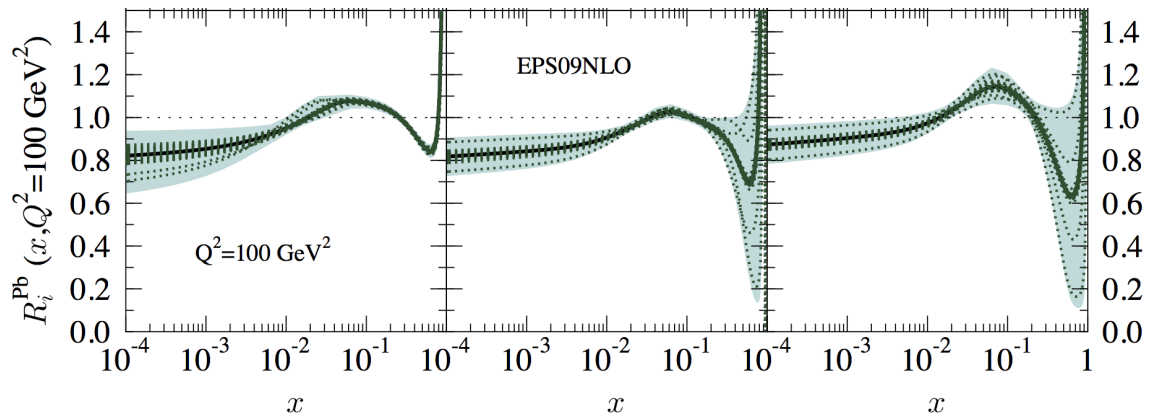


Figure 1.7: Nuclear parton distribution functions. The left panel shows the Nuclear PDF for valence quarks. The middle panel shows the Nuclear PDF for sea quarks. The right panel shows the Nuclear PDF for gluons [35].

1.3.2 Thermalization

The nuclei pass through each other on the time scale of about $0.1 \text{ fm}/c$ [38]. Inelastic scattering of the partons leads to particle production, producing a bulk medium. Quickly after the initial collision, the medium thermalizes. Hydrodynamic modeling of the data matches well when the thermalization time is about $0.6 \text{ fm}/c$, while some theoretical predictions place the time higher, at $2.5 \text{ fm}/c$ [41]. After the medium thermalizes, hard collisions within the medium happen much less often as the hard partons lose much of their energy within the bulk. The matter behaves as a strongly interacting fluid with a low ratio of viscosity to entropy, η/S . The data is well described as an ideal liquid with a viscosity to entropy ratio near the lower limit allowed by the uncertainty principle [29]. The medium expands and cools as the color charged partons interact, reducing the energy density of the system.

The partons interact with the medium through gluon brehmsstrahlung as well as collisions with other partons, which can be elastic or inelastic. Gluon brehmsstrahlung is analogous to electromagnetic brehmsstrahlung, where a charged particle emits photons as it accelerates in the presence of an electromagnetic field. Similarly, color charged particles emit gluons in the presence of the color field within the bulk of the QGP.

1.3.3 Hadronization

As the QGP expands, the relative distance between the quarks and gluons gets larger and the energy density decreases. When the temperature of the medium falls below the critical temperature, T_C , the conditions for deconfinement are no longer fulfilled and the quarks and gluons “dress themselves” as hadrons in a process known as hadronization.

There are various methods of hadronization. One such method is known as *fragmentation*. Fragmentation happens when partons are moving away from each other with large relative momentum. As relative distance increases, the color fields between the partons increase in strength. There comes a point where it is energetically favorable to pull a quark-antiquark pair out of the vacuum, rather than the color field energy increasing to infinity. The produced quarks combine with the initial partons to form color neutral hadrons. This is

an iterative process, and the energy of the initial color field between the partons is divided amongst the resultant hadrons. Fragmentation happens on a scale which is not suitable for pQCD calculations. In proton-proton collisions, this is the only method of hadronization and particle production.

Another method of hadronization is recombination. Recombination is a feature that is exclusive to the deconfined QCD matter. In this process, co-moving partons with low momentum relative to each other will form bound states. These bound states will not form until the average relative kinetic energy falls below the binding energy of the state. Hadrons and resonances with high binding energy may exist even before the system cools past T_C . Therefore, measurements of various bound states' production can provide an experimental thermometer for the medium. After the temperature drops below T_C the hadrons undergo inelastic collisions until chemical freeze-out, at which point the particle species are set. They continue to collide elastically until thermal freeze-out, where the momentum spectra of the particles are set.

1.4 QGP Signatures

1.4.1 Nuclear Modification Factor

Experimental measurements made at particle colliders are used to both confirm and reject various theories of QCD. There are a plethora of measurements used to describe the bulk medium produced in heavy ion collisions. The signatures which are relevant to this thesis will be mentioned here. One of most intuitive observables we can create is that of nuclear modification. In the early stages of the collision, some percentage of parton scattering will involve large momentum transfer, Q^2 . These interactions are known as “hard” collisions. The result of hard scatterings are back to back partons with high momentum. In proton-proton ($p+p$) collisions, these high momentum partons will fragment and produce a collimated group of hadrons known as a *jet*. In a heavy ion collision, the same hard scattering produces these high momentum partons. However, the partons then pass through the bulk, interacting with other partons along the way. These interactions reduce the total

momentum of the parton. A longer path length through the medium produces larger energy loss. If the parton has enough energy, it will exit the medium and fragment into a jet as in the p+p collision. If not, it is absorbed by the medium. This is the concept of nuclear modification. It is a proxy for the energy loss due to the medium. The magnitude of energy loss can be used to distinguish between a hadron gas and a QGP, since the expected energy loss in a QGP is much greater than that of a hadron gas. The measurement used to define the amount of modification is known as the nuclear modification factor, R_{AA} .

$$R_{AA} = \frac{dN_{AA}/dp_T}{N_{coll} * dN_{pp}/dp_T} \quad (1.4)$$

$$R_{CP} = \frac{N_{coll}^{60-100} * dN^{0-20}/dp_T}{N_{coll}^{0-20} * dN^{60-100}/dp_T} \quad (1.5)$$

If the number of hard collisions between partons scales with the number of binary collisions between nucleons, N_{coll} , then the initial hypothesis is that $R_{AA} = 1$. In this case, the heavy ion collision can be modeled as a superposition of p+p collisions, and the energy loss of hard partons within the medium is negligible. Suppression of the nuclear modification factor indicates that the medium is causing significant energy loss, or that binary collision scaling is insufficient. Enhancement of the nuclear modification factor, similarly, indicates a modification of the momentum dependence of produced particles and/or insufficiency of the binary collision scaling. Experimental results have shown that the soft, or low-momentum ($\approx 1\text{-}2$ GeV), spectra scale with the number of scattering nucleons, N_{part} , while the hard, or high-momentum (> 3 GeV), spectra scale with N_{coll} [50].

Figure 1.8 shows the R_{AA} as a function of N_{part} for neutral pions and direct photons [12]. Larger N_{part} indicates more participants and therefore a more head-on collision. For the neutral pions, the R_{AA} is modified by a factor of 5 in the most head-on collisions. The direct photons, however, show no suppression at all. The photons interact via the electroweak force only and their lack of suppression, along with the large neutral pion suppression, indicate that the medium is dominated by QCD interactions.

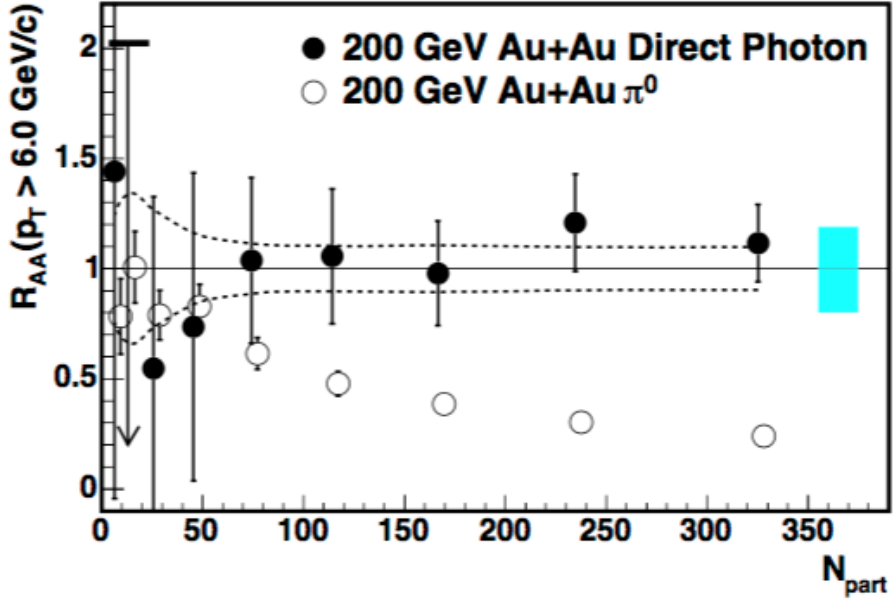


Figure 1.8: Nuclear modification factor R_{AA} for direct photons and π_0 as a function of N_{part} [12].

1.4.2 Azimuthal Anisotropy and Hydrodynamic Flow

Another important observable, which describes bulk collectivity of the medium, is the flow patterns of the produced particles [29]. In a typical heavy ion collision, the overlap region of the colliding nuclei is asymmetric in the x-y plane, where z defines the beam line (see Figure 1.9). The reaction plane is defined by beam axis and the impact parameter, b . The energy deposited will have some spatial anisotropy due to the particular geometry of the overlap region, as well as the initial conditions of the colliding nuclei.

The triple differential particle distribution can be expanded in a Fourier series in order to better characterize the azimuthal anisotropy.

$$\frac{d^3N}{dydp_Td\phi} \sim 1 + \sum_n 2v_n \cos[n(\phi - \psi_n)] \quad (1.6)$$

The coefficients, v_n , are used to characterize different types of collective flow. The first coefficient in the Fourier expansion, v_1 , is commonly called directed flow. It describes the preferred direction of expansion along the impact parameter. Using the coordinate system

from Figure 1.9, v_1 is proportional to the ratio of the number of particles traveling in the positive x direction to the number of particles traveling in the negative x direction. The second coefficient, v_2 , refers to the elliptic flow of the expansion. It is proportional to the ratio of the number of particles traveling out-of-plane to the number of particles traveling in-plane. The third coefficient, v_3 , describes the triangular flow. Figure 1.10 shows a visual representation of the Fourier coefficients in momentum space, with the x-axis being the reaction plane.

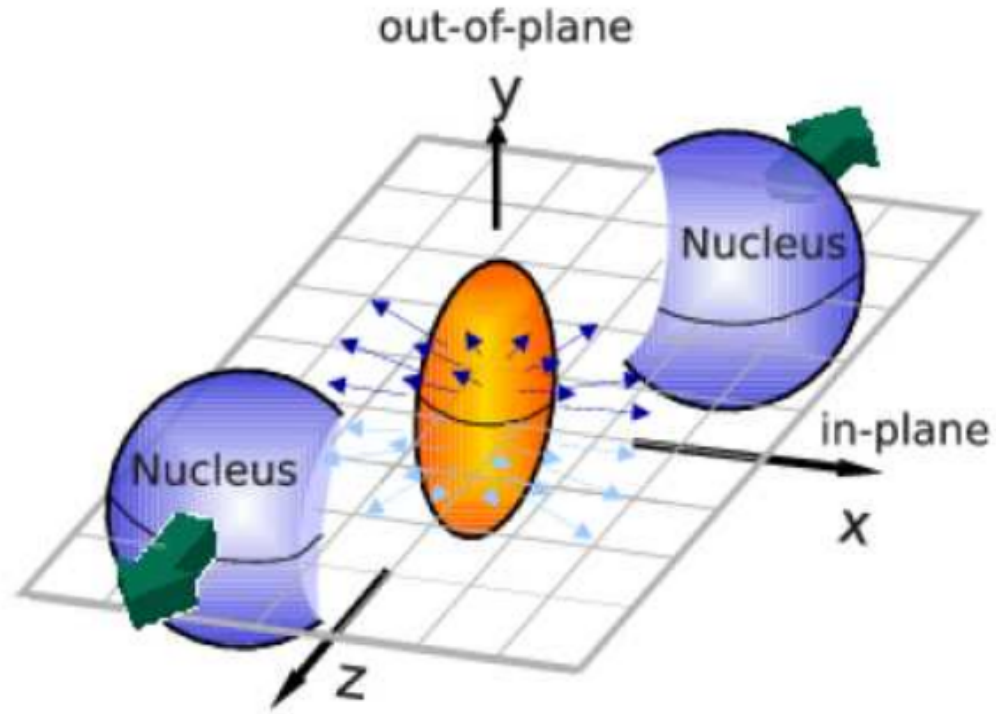


Figure 1.9: Collision geometry.

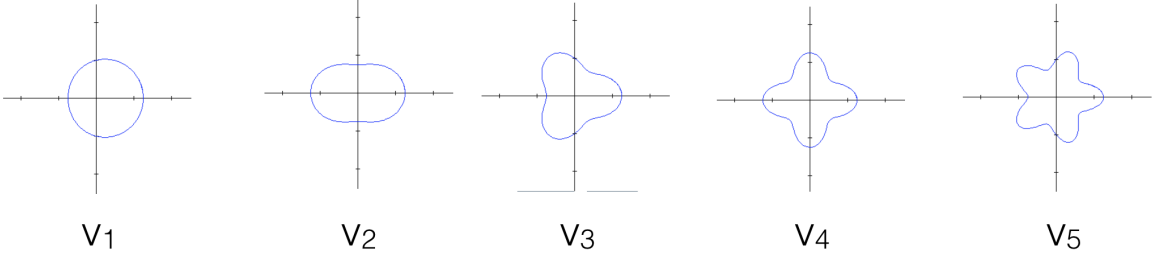


Figure 1.10: Fourier coefficients [3].

Thermalization of the bulk matter creates pressure gradients within the medium. These pressure gradients are larger in-plane relative to out-of-plane (see Figure 1.11). The transverse momentum, p_T , of low momentum particles in-plane is increased relative to those out-of-plane. This causes a momentum dependence of the elliptic flow parameter, v_2 , as there are more final state hadrons in-plane than out-of-plane. In this way, the initial spatial anisotropy of the medium is converted into a momentum space anisotropy in the final state. The mapping of spatial anisotropy to momentum space anisotropy is only possible if the viscosity to entropy ratio of the medium is low. For higher η/S , such as in a hadron gas, the medium would tend towards an isotropic distribution and the information would be lost. The increase in momentum due to elliptic flow takes place in the soft region, at low momentum. At higher momentum, second order azimuthal anisotropies are introduced due to energy loss and *jet quenching*, rather than collective flow. The path length out of the QGP is shorter in-plane relative to out-of-plane. Particles of a particular p_T have a better chance to escape the QGP in-plane, while they are likely to be completely thermalized if traveling out-of-plane. Fragmentation of these hard partons leads to an increase in final state hadrons in-plane relative to out-of-plane.

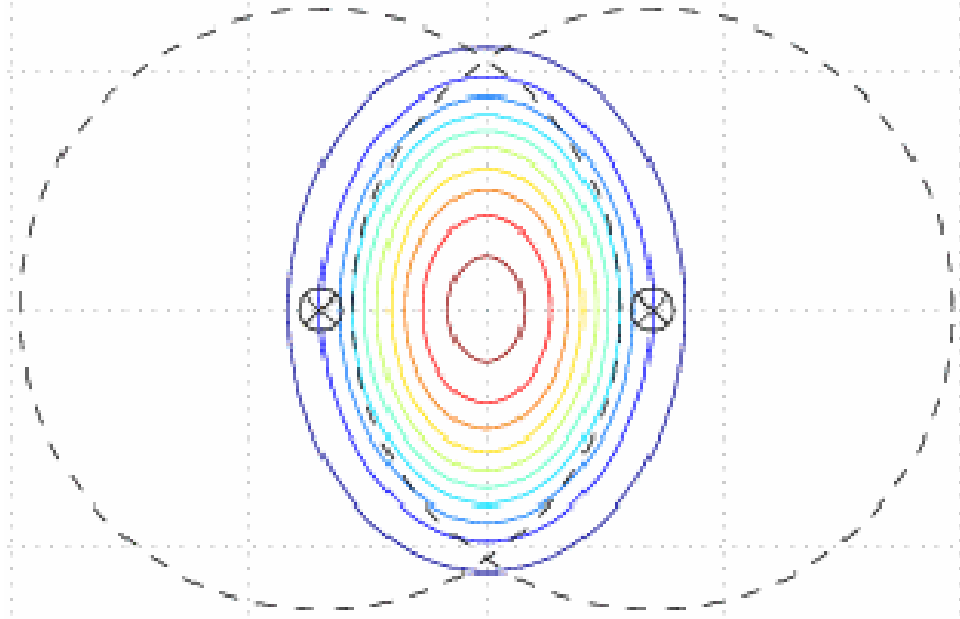


Figure 1.11: Diagram of pressure gradient equipotentials.

Figure 1.12 shows a measurement of v_2 for various hadrons, scaled by the number of constituent quarks [9]. Previous measurements of the mass dependence of elliptic flow implied that the partons themselves were flowing. The quark scaling, particularly in the right-hand panel of Figure 1.12, produces striking agreement between flow measurements of different hadrons. This is a strong indicator that the quarks and gluons are at least partially deconfined when the flow patterns are developing early in the collision.

There are a number of measurements indicating that a QGP has indeed been produced in relativistic heavy-ion collisions at the Relativistic Heavy Ion Collider (RHIC) and Large Hadron Collider (LHC). However, there are still many challenges ahead. Theoretical calculations in QCD fail to describe both of these observables at all momenta simultaneously. Figure 1.13 shows R_{AA} and v_2 for neutral pions as well as heavy flavor electrons (these will be discussed in the next section), with a number of theoretical calculations overlayed [10].

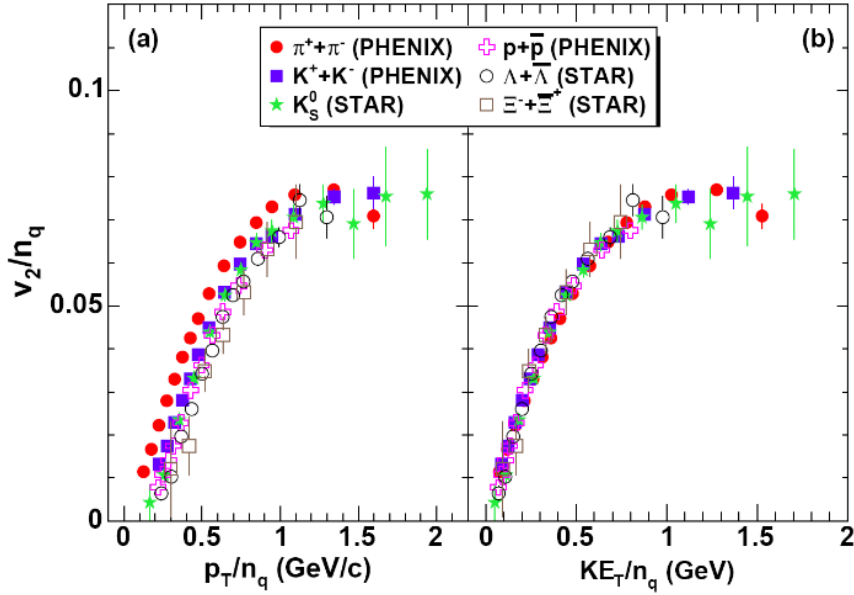


Figure 1.12: Quark scaling of azimuthal anisotropy [9].

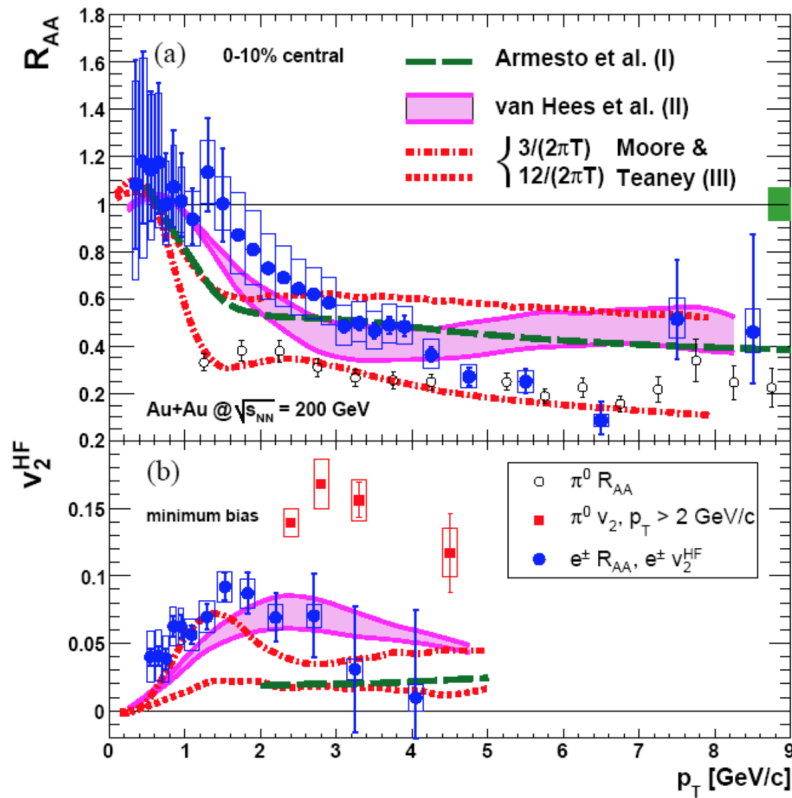


Figure 1.13: Nuclear modification factor and elliptic flow measurements for neutral pions and heavy flavor electrons [10].

1.5 Heavy Flavor and Hard Probes

The QGP phase is very short lived, on time scales of the order of $10 \text{ fm}/c$ or 10^{-23} sec . The short lifetime makes it impractical to use external probes in an experiment. Instead, internal probes which are produced in the collision are used to study the medium. Heavy quarks, charm and bottom, provide a unique tool with which to study the QGP. Their masses dictate that they can only be produced in very hard scattering processes which happens early in the collision, primarily by gluon-gluon fusion [26]. Conversely, light quarks are produced by soft and hard processes at various times during the systems evolution. The lifetimes of these heavy quarks are longer than the lifetime of the QGP. Together, this means that they are produced early in the QGP formation, and survive the full evolution of the QGP. The heavy masses of the charm and bottom signify that their creation necessitates high momentum transfer between the colliding partons. This means that they will be created in processes where pQCD can be a useful tool due to asymptotic freedom. In this way, the heavy quarks can serve as a calibrated probe of the QGP.

1.5.1 Factorization

In hard scattering processes, with high Q^2 , pQCD can be used to calculate the parton-parton cross section. However, these partons are confined within hadrons before the collision. Similarly, the partons will dress themselves into color neutral final state particles before we have a chance to detect them. A cross section of final state particles requires consideration of these effects. This can be done assuming the hard scale can be factorized from the soft scale physics [42]. This assumption is known as the factorization theorem. In this context, a cross section may look something like:

$$d\sigma = \int dx_1 dx_2 dz f_1(x_1) f_2(x_2) d\sigma_{pQCD} D_p^h(z). \quad (1.7)$$

$$d\sigma = \int \color{blue}{dx_1 dx_2} \color{red}{dz} f_1(x_1) f_2(x_2) d\sigma_{pQCD} \color{red}{D_p^h(z)}. \quad (1.8)$$

$$\begin{aligned}
& f_1(x_1), f_2(x_2) : DIS \\
& d\sigma_{pQCD} : pQCD \\
& D_p^h(z) : e^+e^-, DIS
\end{aligned} \tag{1.9}$$

The functions, $f_1(x_1)$ and $f_2(x_2)$, are the parton distribution functions (PDF) where x represents the momentum fraction of a parton within the nucleon. They describe the momentum distribution of partons within the colliding hadrons. These functions are assumed to be independent of the collision. The parton-parton cross section, $d\sigma_{pQCD}$, is the quantity that is calculable within the pQCD framework. In hard scattering processes such as those found at particle colliders, these cross sections are calculated with remarkable accuracy. The factor, $D_p^h(z)$, is a function which describes the final state momentum distribution that results from a fragmenting parton. This is a soft process and, like the PDFs, cannot be calculated within pQCD. Assuming that these functions are independent of the collision, they too can be measured in deep inelastic scattering experiments, as well as $e^- + e^+$ collision experiments. Figure 1.14 shows a fixed order plus next to leading log (FONLL) pQCD calculation of heavy flavor production compared with PHENIX data [8].

1.5.2 Energy Loss

A robust theory of the energy loss of strongly interacting particles within the medium is paramount for a complete description of the strong interaction. Previously, it had been thought that heavy quarks would not lose much energy to elastic collisions within the medium. The average momentum squared of heavy quarks in the medium is $\langle p^2 \rangle \sim 3MT$ where M is the heavy quark mass and T is the temperature of the medium [42]. It is assumed that the average momentum transfer within the medium is given by the temperature. Since $M \ll T$, this means many collisions are required to thermalize the heavy quarks.

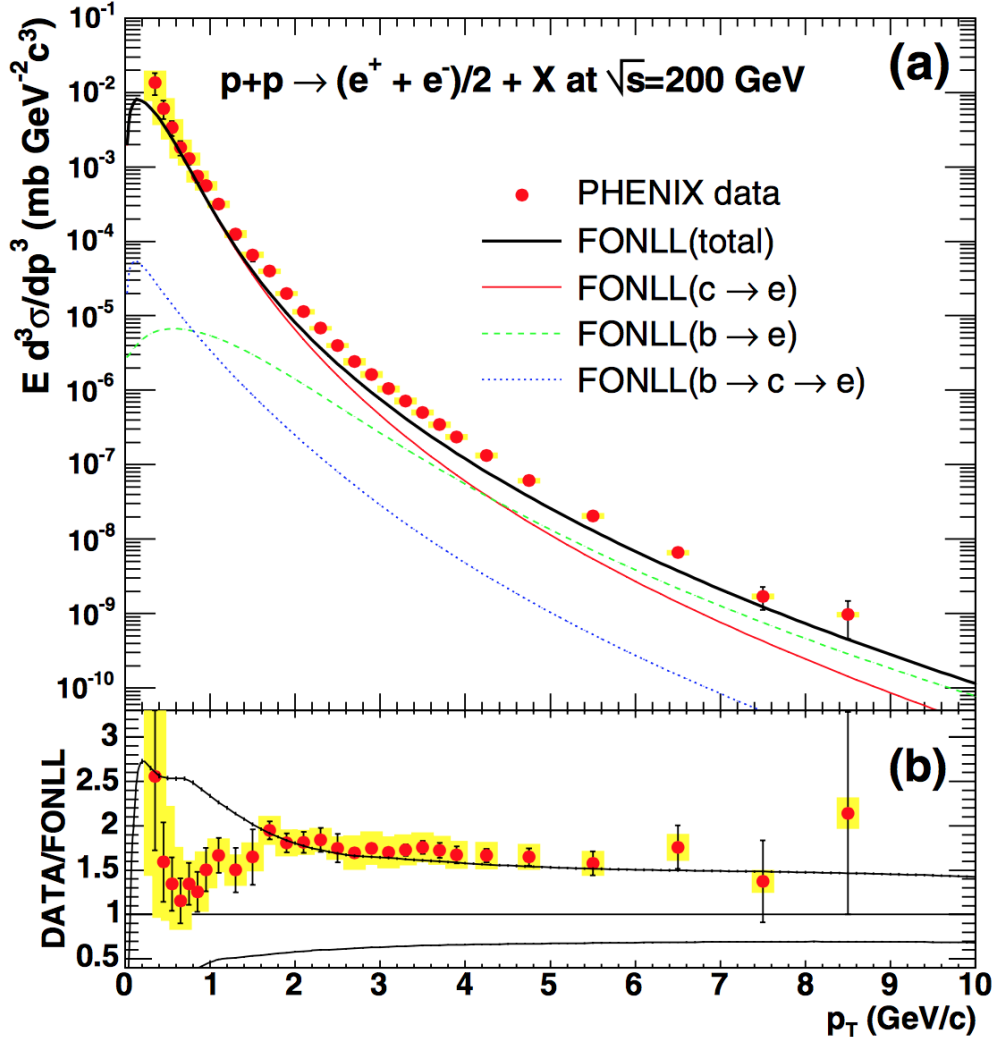


Figure 1.14: Upper plot: invariant differential cross sections of electrons from heavy-flavor decays [26]. The error bars (bands) represent the statistical (systematic) errors. The curves are FONLL calculations. Lower plot: ratio of the data to the FONLL calculation. The upper and lower curves represent the upper and lower limits of the FONLL uncertainty band. An overall normalization uncertainty of 10% is not shown [22].

Furthermore, heavy quarks are predicted to lose less energy due to gluon radiation because of the “dead cone effect”. The dead cone effect refers to the suppression of radiation at angles $\sin(\theta) \sim m/E$ [54]. For large mass, the angle of suppression becomes large and the gluon radiation is suppressed. Therefore, the heavy quarks serve as a unique measure of the strength of the coupling within the medium. However, the commonly held belief that these heavy quarks would plow right through the medium like a bowling ball, without thermalizing,

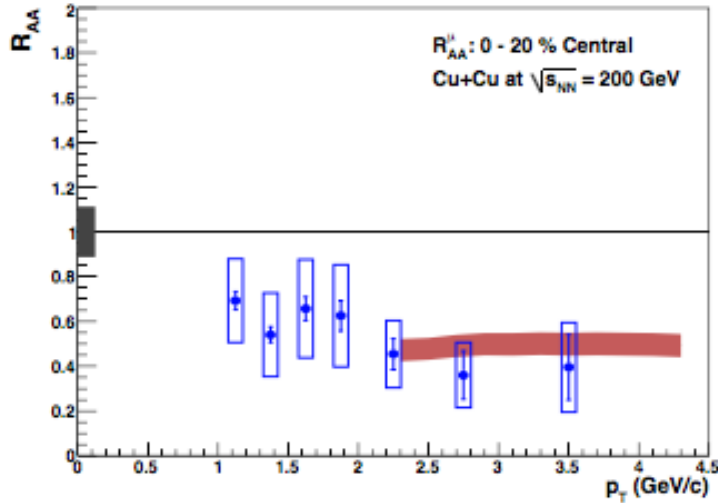
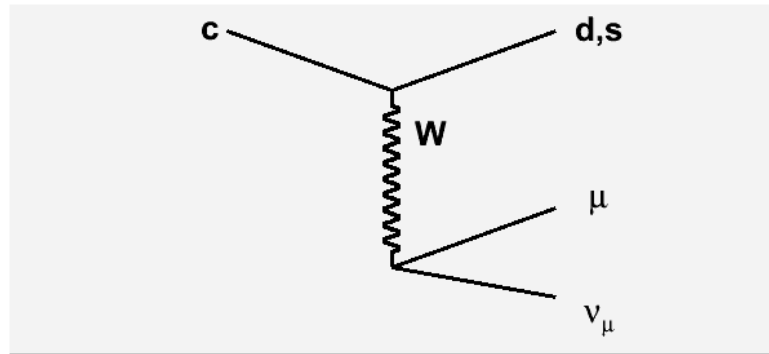


Figure 1.15: Nuclear modification factor R_{AA} for heavy flavor single muons in Cu+Cu collisions [11].

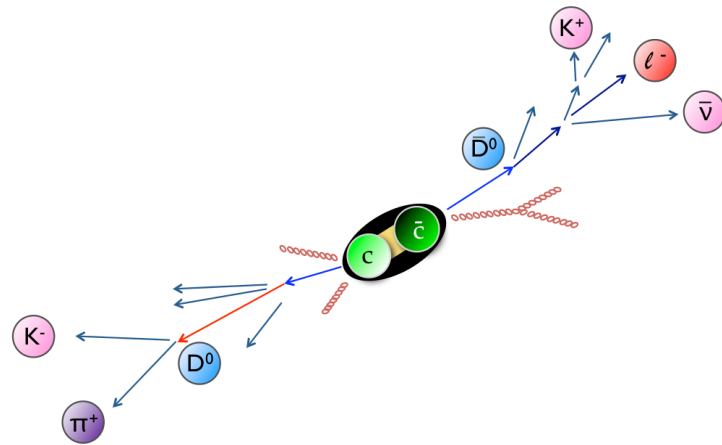
has been contradicted by empirical evidence. Recent experimental results (see Figure 1.15) suggest that thermalization of the heavy quarks may indeed happen [42], indicated by the large suppression seen in the heavy flavor single muon R_{AA} .

1.5.3 Semi-leptonic and Hadronic Decay

As has been mentioned above, quarks and gluons are not observables in and of themselves. It is only possible to detect the hadrons which contain these partons. While the heavy quarks (and their respective hadrons) live longer than the QGP, they do not survive long enough to make it to our detectors [Table 1.1]. However, we can detect the relatively long-lived decay products of these hadrons. The types of decay can be classified into two distinct groups, the hadronic decays and the semi-leptonic decays. A hadronic decay yields only hadrons. Semi-leptonic decay means there are hadrons and leptons in the final state. When only leptons are produced it is referred to as purely leptonic decay. Figure 1.16b shows an illustration depicting a hadronic decay and a semi-leptonic decay. In practice, detection means tracking and identifying electrons, muons, and the light hadrons as well as their corresponding anti-particles. The decay products of light hadrons are, by themselves, indistinguishable from the decay products of heavy flavor hadrons.



(a) Feynman diagram for charm decay



(b) charm meson decay

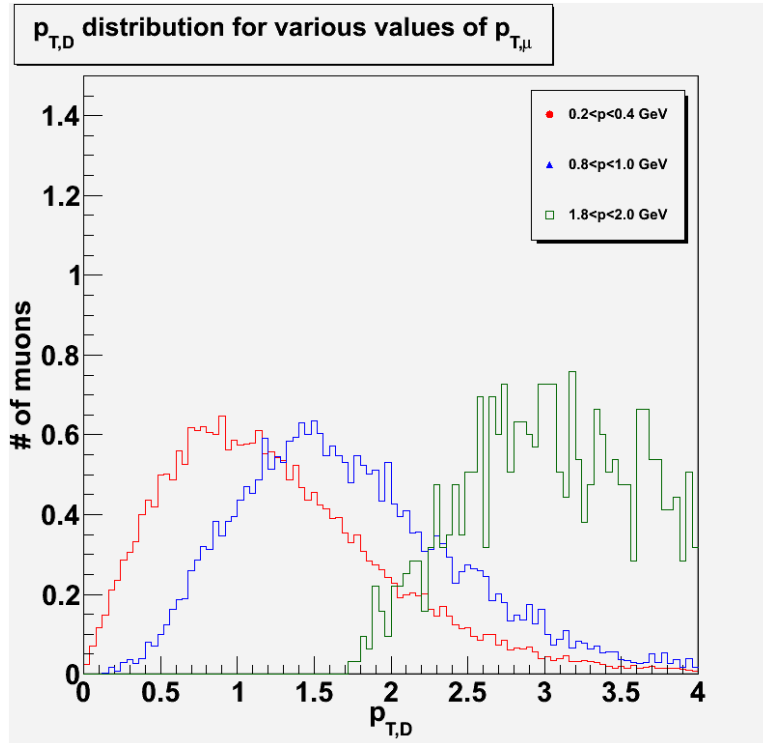
Figure 1.16: Heavy Flavor Decay [31].

Table 1.1: Table of Heavy Flavor Meson Decay Lengths.

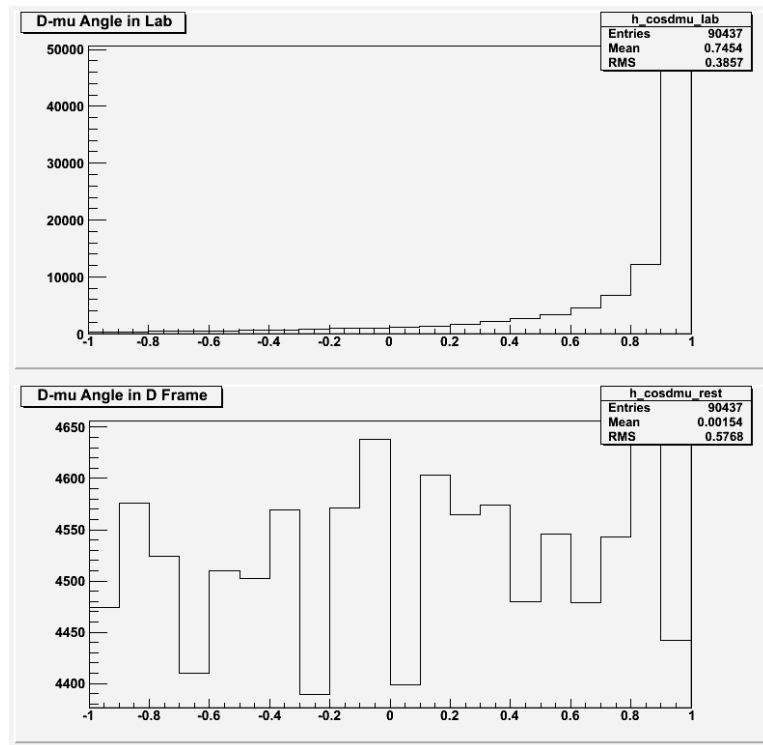
	Decay length, $c\tau$
D^\pm	$311.8 \mu\text{m}$
D^0	$122.9 \mu\text{m}$
B^\pm	$492.0 \mu\text{m}$
B^0	$455.4 \mu\text{m}$

Therefore, the dileptonic and semi-leptonic decays of pions and kaons are a large source of background in heavy flavor measurements. However, there are a variety of techniques which can be used to purify a sample of heavy flavor candidates. The measurements made are statistical measurements, and it is generally not an absolute certainty that a particular decay product came from a particular type of hadron.

Hadronic decays have the advantage of certain decay branches in which all the decay products can be detected and the parent meson can be reconstructed through an invariant mass technique. Charmonium has high branching ratios for dilepton decays so the J/ψ (and its excitations) are conveniently reconstructed in the same way. A disadvantage is that the detector does not have 4π coverage, so not all decay daughters are necessarily detected. In this case the parent cannot be reconstructed and the daughter tracks become background. Single leptons have the advantage that they can be triggered on with high efficiency. This allows us to acquire higher statistics for single leptons and make single lepton measurements out to higher p_T than, for example, reconstructed hadrons. Another advantage is that the azimuthal direction of the lepton is well correlated to the azimuthal direction of the parent meson. This is due to the heavy mass of the parents relative to the daughters. Even if, in the parent rest frame, the lepton is emitted perpendicular or even anti-parallel to the direction of propagation of the parent, after boosting to the lab frame we find that the lepton is still traveling along, or close to, the same trajectory as the parent. Figure 1.17a shows muon yields for different ranges of total muon momentum plotted against the parent D mesons



(a) Correlation in p_T



(b) Correlation in θ

Figure 1.17: Pythia study of correlations of decay muons to their parent mesons [52].

transverse momentum. Figure 1.17b shows the D- μ emmission angle in the lab and in the D rest frame.

1.6 Motivation

Cu+Au measurements at forward rapidity provide an opportunity to make new measurements which have not been made anywhere else in the world. The PHENIX detector is equipped to make such measurements with data taken during the Run-12 period in May and June of 2012.

1.6.1 Forward Rapidity Measurements

The PHENIX detector covers two physically disconnected regions. The central arm is located transverse to the beam line. It covers a pseudorapidity $-0.35 < \eta < 0.35$. The muon arms are located at forward and backward pseudorapidities $1.2 < |\eta| < 2.4$. The advantages of forward rapidity measurements will be discussed here, while the specifics of the PHENIX detector will be discussed in more detail in Chapter 3.

Nuclear PDF's

The creation of a QGP requires collisions between high momentum partons. Colliding partons with equal magnitude momenta in opposite directions will produce partons with most of their momentum directed in the plane transverse to the beam. The final state particles born from such partons will likely fall into the acceptance of the central arm. In the case that one parton has a higher magnitude momentum than the other, the produced partons will be created with a non-negligible longitudinal momentum component. In other words, final state particles that travel with significant longitudinal momentum originate from a collision of a *low-x* (momentum fraction) parton with a *high-x* parton. In this case, the final state particles may fall into the acceptance of the muon arms. Therefore, making measurements at forward (and backward) polar angles relative to the beam axis provides a way to probe different regions of the nuclear PDF's discussed previously. Figure 1.18 shows the range of x-values probed in the muon arms in proton-proton collisions [56].

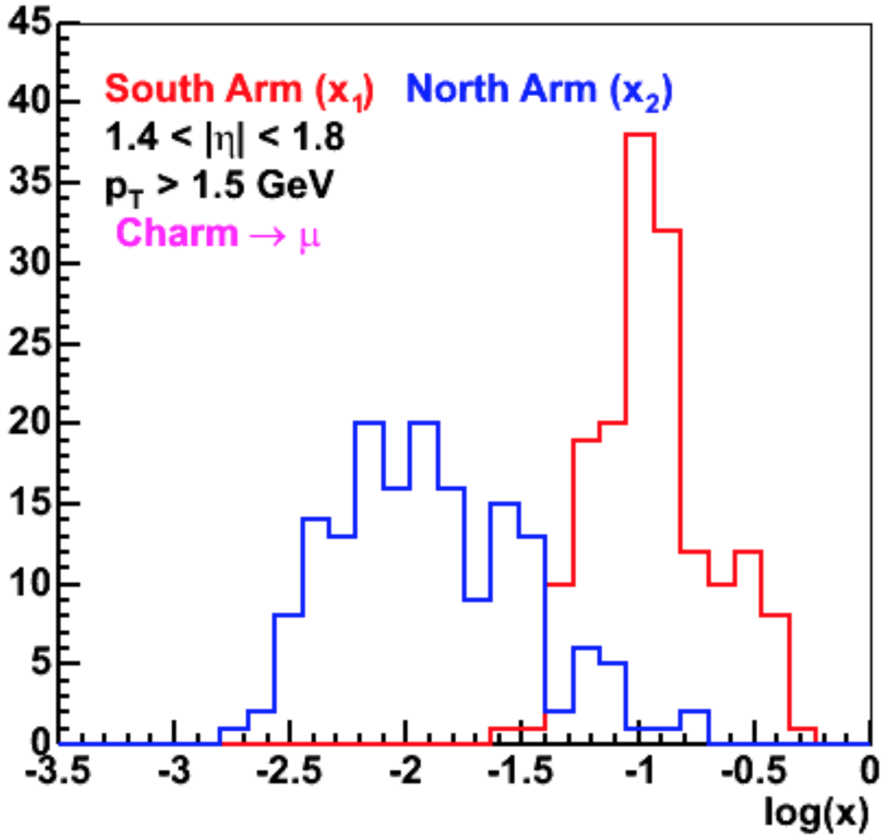


Figure 1.18: Distribution of logarithm of momentum fraction x values in the north and south arm [56].

Exploring the Phase Diagram

The hardest parton-parton collisions will consist of two *high- x* partons, which generally leads to final state particles that travel mostly in the transverse plane. These particles probe the hottest QCD matter with the highest energy densities created in a heavy ion collision. This matter, found at the center of the created medium, will have the highest temperature and the lowest baryonic chemical potential. Further from the center, the medium will deviate from the perfect liquid model which best describes measurements taken at mid-rapidity. The matter found further from the center may have lower energy density than is found at the center, corresponding to a lower temperature and higher baryon chemical potential. The outer regions of the medium will occupy a different part of the QCD phase diagram. Particles found at higher rapidities are able to probe these regions of the phase diagram.

The deviation from perfect fluidity may alter the energy loss within the medium as well as the flow coefficients, v_2 and v_3 .

1.6.2 Asymmetric Collisions

Asymmetric collisions, such as Cu+Au, provide additionally beneficial data relative to the symmetric collision data that is more common. In symmetric collisions the odd flow coefficients (v_3 , v_5 , etc...) are suppressed due to the symmetry of the colliding nuclei. Of particular interest to the Cu+Au system is the triangular flow coefficient, v_3 . While individual events in symmetric collisions may exhibit triangular flow due to the random fluctuations of the position of colliding nucleons, the event averaged v_3 is expected to be small. In contrast, peripheral Cu+Au collisions provide a particular geometry that may induce a large v_3 . This is due to the relative size of the Cu nucleus compared to the Au nucleus, as shown in figure 1.19 [1].

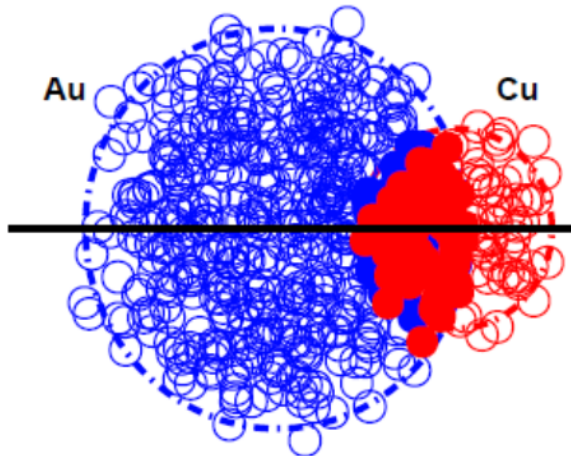


Figure 1.19: Illustration depicting a peripheral Cu+Au collision [1].

Chapter 2

Survey of Previous Experimental Results

The existence of a “soup of quarks and antiquarks” had been predicted as early as 1977[30], not long after the discovery of the J/ψ . The search for such a state of matter proceeded over the course of the next two decades, culminating in the initial operation of RHIC in 2000. In the spring of 2002, the first heavy flavor measurements from PHENIX were published in PRL [33]. In the years following these initial measurements, a rich body of work has developed characterizing the QGP and the interactions of its constituents.

2.1 Heavy Flavor Spectra

PHENIX published the first single muon measurement using the PHENIX muon arms in 2007 [53]. Figure 2.1 shows the heavy flavor (primarily charm in this momentum range) cross section measured in p+p collisions. A large discrepancy is seen between the perturbative calculations (FONLL) and the data. However, the systematic uncertainties associated with the calculation as well as the data preclude a definitive conclusion. Nevertheless, the charm cross section in p+p collisions serves as a baseline for heavy ion measurements of charm production.

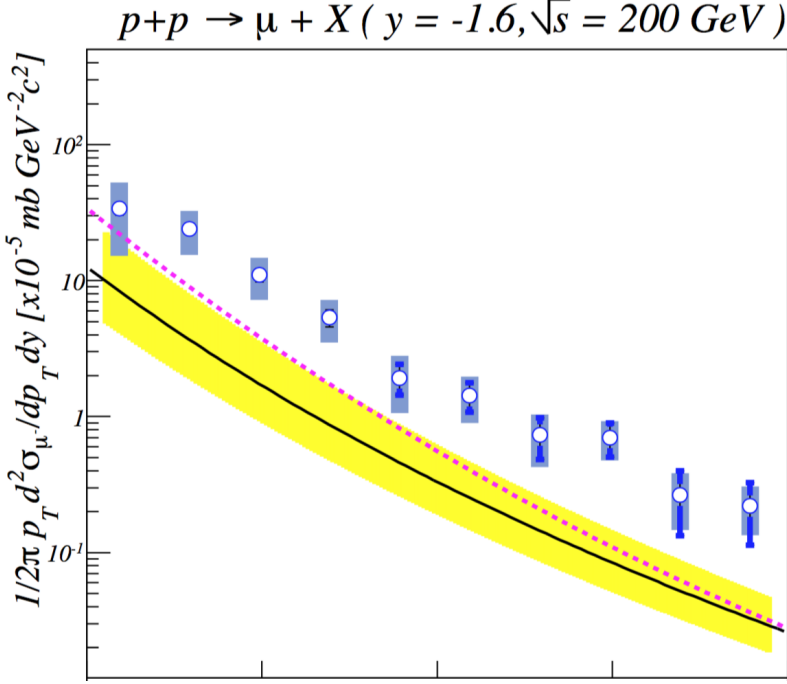


Figure 2.1: Charm cross section measured in p+p collisions at 200 GeV [53]. The PYTHIA prediction is represented by the dotted line. A FONLL calculation is also plotted, represented by the black line with the yellow band representing systematics. The x-axis starts at 1 GeV with 500 MeV intervals.

In 2005, RHIC produced large data sets of both p+p and Cu+Cu collisions. These data sets were analyzed by former UT graduate students in the RHIP group [31] [28], and culminated in a publication in Physical Review C in 2012 [11], referred to from here as PPG117. The 200 GeV p+p program from 2005 delivered a total integrated luminosity of 29.5 nb^{-1} , more than twice the delivered luminosity of all previous p+p runs (14 nb^{-1}). Meanwhile, the 200 GeV Cu+Cu program delivered a total luminosity of 42.1 nb^{-1} . A more statistically meaningful measurement of the charm cross section was produced, as well as the first single muon R_{AA} measurement.

Figure 2.2 shows the charm cross section measured in p+p collisions as a function of p_T . Particularly notable is the extension of the measurement from 3 GeV out to 7 GeV while reducing the error bars significantly. Coupled with the Cu+Cu single muon measurement, PPG117 was able to deliver the first single muon R_{AA} measurement with remarkable accuracy. However, due to the large systematic error, the measurement was only extended to 4 GeV. Figure 2.3 shows the single muon R_{AA} for single muons with a transverse

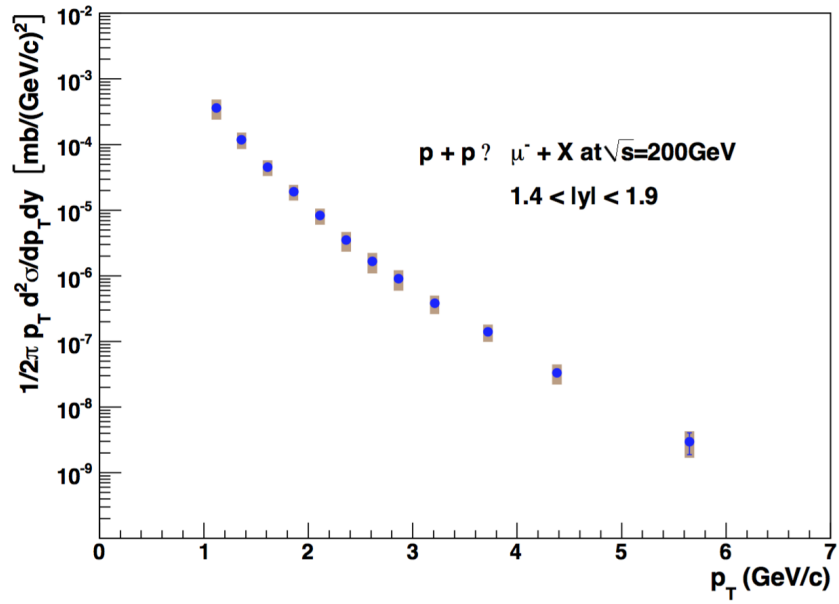


Figure 2.2: Charm cross section measured in $p+p$ collisions at 200 GeV [11].

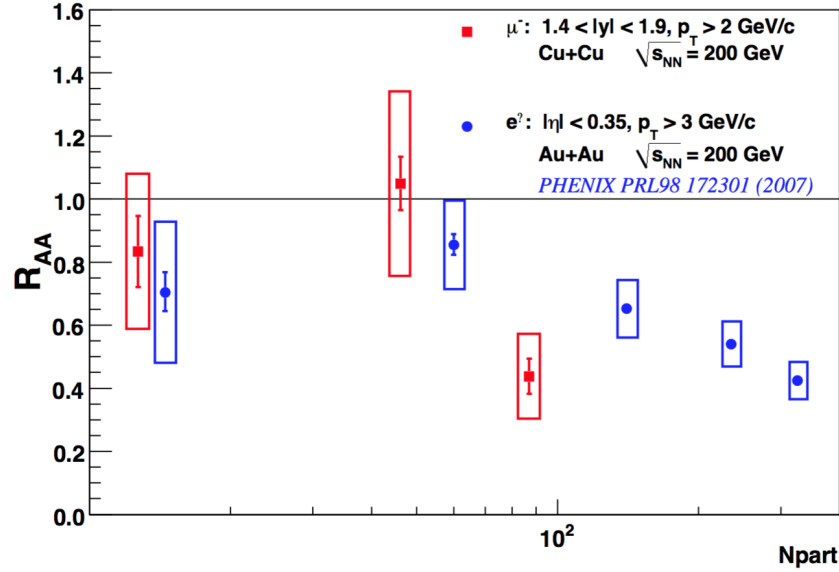


Figure 2.3: Nuclear modification factor as a function of N_{part} . The red points are the measurement published in PPG117, while the blue points are the nuclear modification factor for single electrons in $Au+Au$ collisions [11].

momentum above 2 GeV as function of N_{part} compared with the single electron R_{AA} measured in the larger Au+Au system, at mid-rapidity, and with a transverse momentum larger than 3 GeV. The reduction in R_{AA} in more central collisions is generally viewed as a signature for the existence of a strongly interacting medium with which the constituents lose energy (read: a QGP). However, in more peripheral collisions, the nuclear modification factor is consistent with one. This suggests that a QGP may not be formed at high rapidity in the peripheral collisions. The authors of PPG117 address this possibility, stating “One expects the Bjorken energy density of the matter produced in the mid-rapidity region in the most central Au+Au collisions to be at least twice as large as that of the matter produced in the forward rapidity region in most central Cu+Cu collisions”[11]. This suggestion leads to the conclusion that so-called “cold nuclear matter effects” lead to some modification of the final state spectra. Cold nuclear matter (CNM) effects refer to modification seen in systems where a QGP is not expected to be produced.

PPG117 represented a substantial step forward in the understanding of single muons, and served as a jumping off point for future single muon analyses, including this one. Following on the heels of PPG117 sprung another single muon analysis from the deuteron-gold (d+Au) collision system [6]. This publication, referred to from here as PPG153, followed the analysis procedure laid out in PPG117 with some slight modifications in the background subtraction.

The d+Au system offers a chance to study collisions which do not produce a QGP. The data show an enhancement for negative muons in the Au-going direction and suppression in the d-going direction in the most central collisions, while the data from peripheral collisions is consistent with one for both the Au-going and d-going directions. The measurement (shown in Figure 2.4) is particularly interesting in that it “suggests that various CNM effects combine to produce the observed modifications” [6].

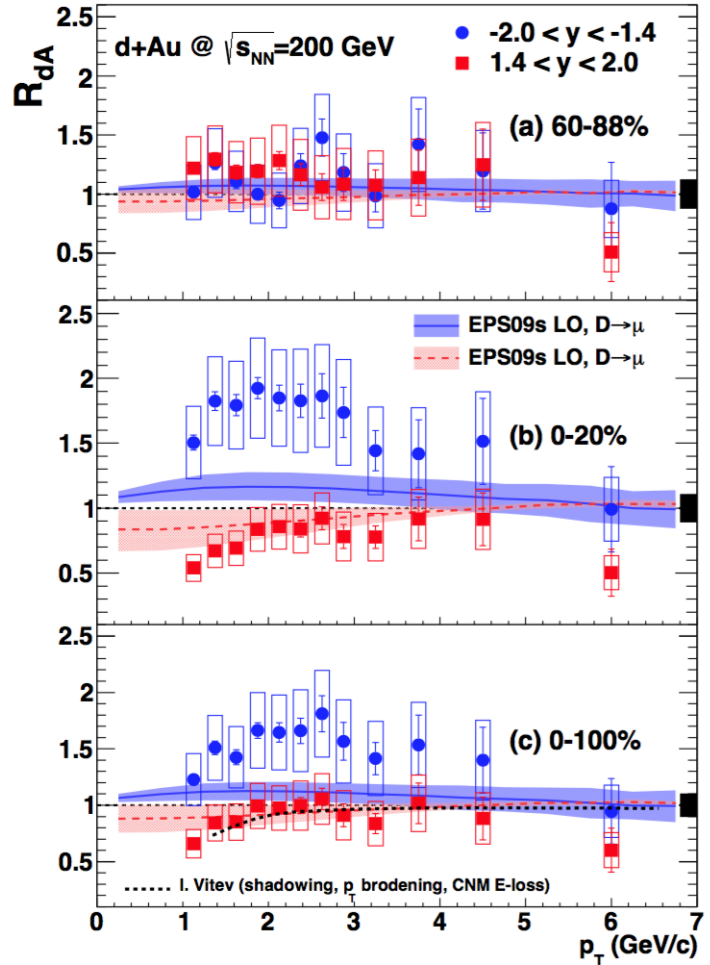


Figure 2.4: The nuclear modification factor R_{dA} , for negatively charged heavy-flavor muons in d+Au collisions for the (a) 60%–88%, (b) 0%–20%, and (c) 0%–100% most central collisions. The black boxes on the right side indicate the global scaling uncertainty. The red dashed (blue solid) lines in each panel are calculations at forward (backward) rapidity based on the EPS09s nPDF set [6].

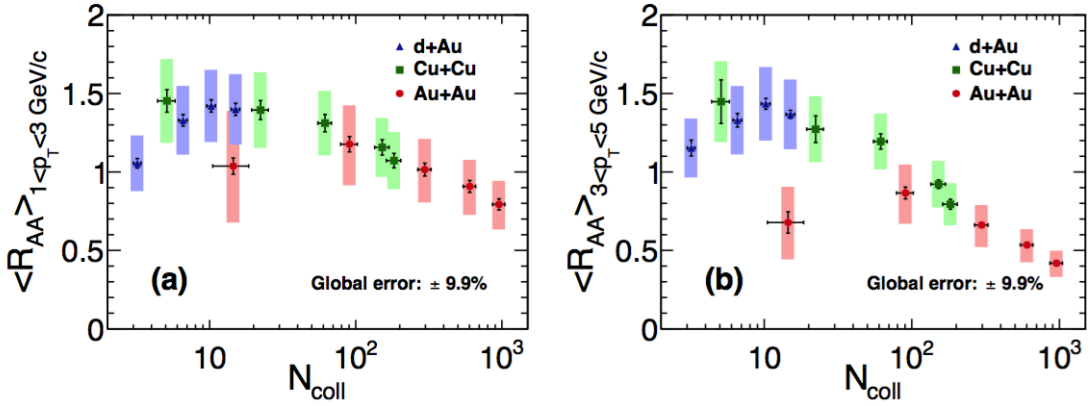


Figure 2.5: R_{AA} of heavy-flavor electrons as a function of N_{coll} in various collision systems [5].

At mid-rapidity, heavy flavor single electrons have been measured in the same collision systems. Figure 2.5 shows the nuclear modification factor for d+Au, Cu+Cu, and Au+Au collisions as a function of N_{coll} . The data show enhancement in d+Au collisions and suppression in central Au+Au collisions, with Cu+Cu providing a smooth transition between cold and hot nuclear matter effects [5].

A discrepancy arises between the two rapidity regions, where at mid-rapidity the Cu+Cu data follows a smooth transition from cold to hot as centrality increases, such that the most central Au+Au collisions are more suppressed than the most central Cu+Cu collisions, whereas at forward rapidity the suppression in the most central Au+Au collisions is comparable to that of the most central Cu+Cu collisions. It seems the conclusion that CNM effects (such as shadowing, Cronin effect, and initial state parton energy loss) at forward rapidity may play a larger role in the modification of the spectra is well founded.

The puzzle is further complicated when considering closed charm measurements in these collision systems. The charm quarks within a J/ψ are sensitive to the same effects as the charm quarks which go on to produce open charm. However, the closed charm are additionally affected by breakup within the nuclear matter [6], as well as recombination effects in the hadronization phase of the system evolution. Figure 2.6 shows the J/ψ suppression in central Cu+Cu collisions as a function of p_T on the left and rapidity on the right [23]. The results

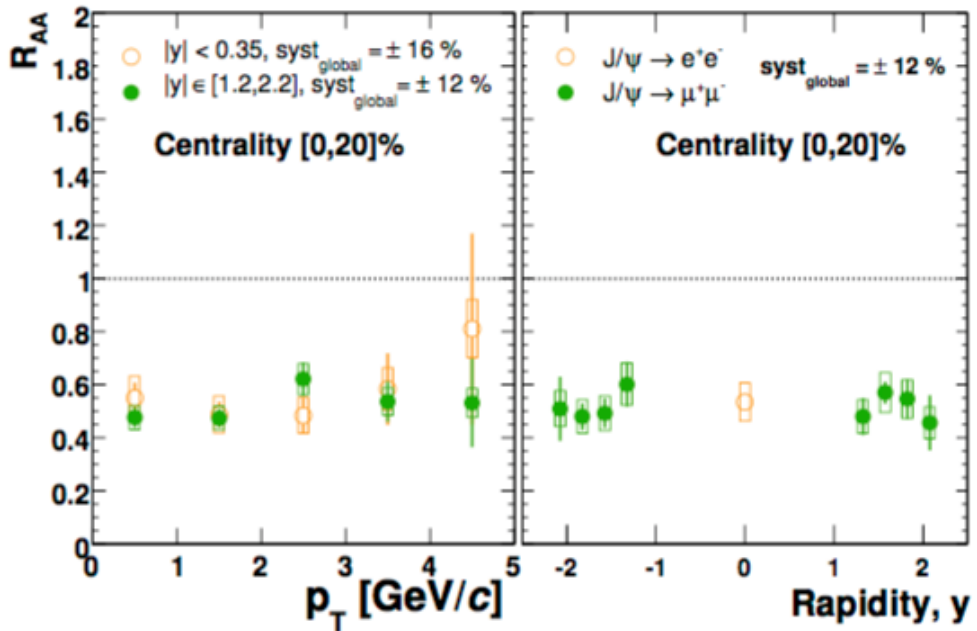


Figure 2.6: R_{AA} versus p_T (left) and y (right) for J/ψ production in the most central Cu+Cu collisions [23].

are consistent with each other. This is consistent with the single lepton measurements, which showed similar suppression in central collisions.

Meanwhile, a comparison of the forward J/ψ suppression in Cu+Cu and Au+Au collisions shows a smooth transition between the two systems, shown in the middle panel of Figure 2.7 [23]. This is similar to what was seen with single electrons at mid-rapidity. To summarize, we see a clear transition in single electron suppression as a function of number of colliding partons between the Cu+Cu and Au+Au systems at mid-rapidity, as well as a clear transition in J/ψ suppression between the two systems at mid- and forward rapidity. However, with single muons measured at forward rapidity, the suppression as a function of N_{part} does not transition smoothly between Cu+Cu and Au+Au, as shown in Figure 2.3. Instead, the central collisions show a similar suppression even though the central Au+Au collisions have a larger N_{part} .

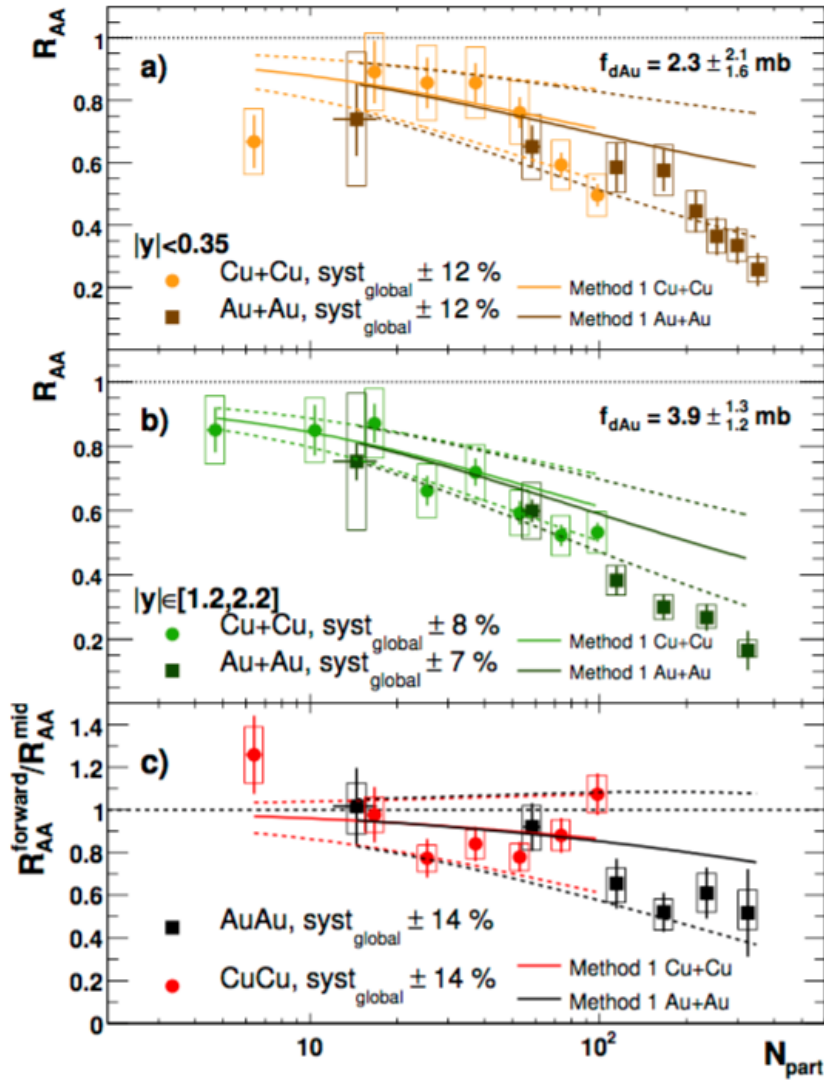


Figure 2.7: R_{AA} versus N_{part} for J/ψ production in Cu+Cu and Au+Au collisions. (c) Forward/mid-rapidity R_{AA} ratio. The curves are predictions from ad-hoc fits to d+Au data [23].

A comparison of the J/ψ suppression in $d+Au$ collisions may help illuminate the discrepancy. Figure 2.8 shows a comparison between the J/ψ and single muon R_{dA} measurements at forward rapidity. The data show agreement in the forward (d -going) direction but show significant disagreement in the backward (Au -going) direction. As stated in PPG153, “The larger difference of the R_{dA} between J/ψ and open charm at backward rapidity compared to forward rapidity could be related to the longer time this $c\bar{c}$ state requires to traverse the nuclear matter or the larger density of comoving particles after the initial collision at backward rapidity” [6]. This is yet more evidence that CNM effects play a significant role in heavy flavor suppression at high rapidity.

Recently, PHENIX has reported the nuclear modification factor for J/ψ in $Cu+Au$ collisions, shown in Figure 2.9 [24]. The results show a similar trend as seen in the $d+Au$ data, in that the forward (Cu -going) direction is more suppressed than the backward (Au -going) direction. However, the $d+Au$ data showed enhancement in the backward direction while the $Cu+Au$ data show suppression albeit to a smaller extent than the forward

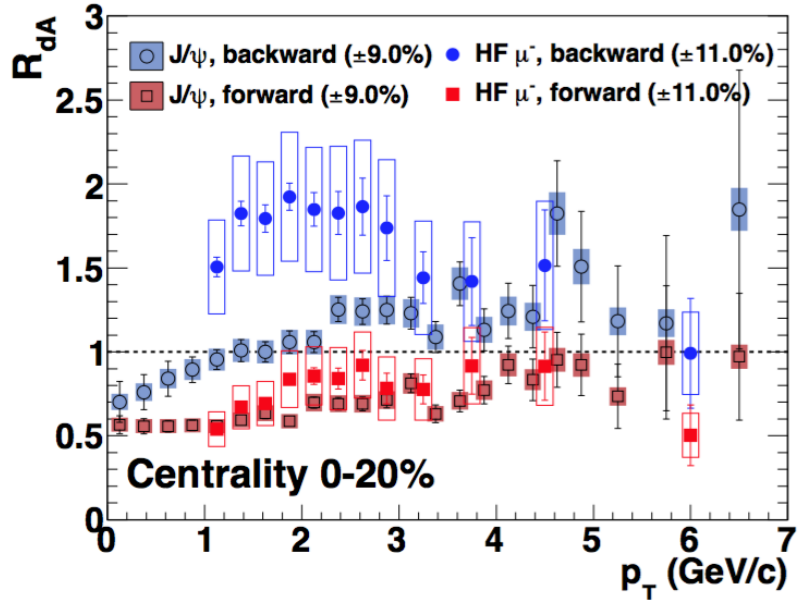


Figure 2.8: The nuclear modification factor R_{dA} for J/ψ and heavy-flavor muons for the 0%-20% centrality class. The global systematic uncertainty on each distribution is shown as a percentage in the legend [6].

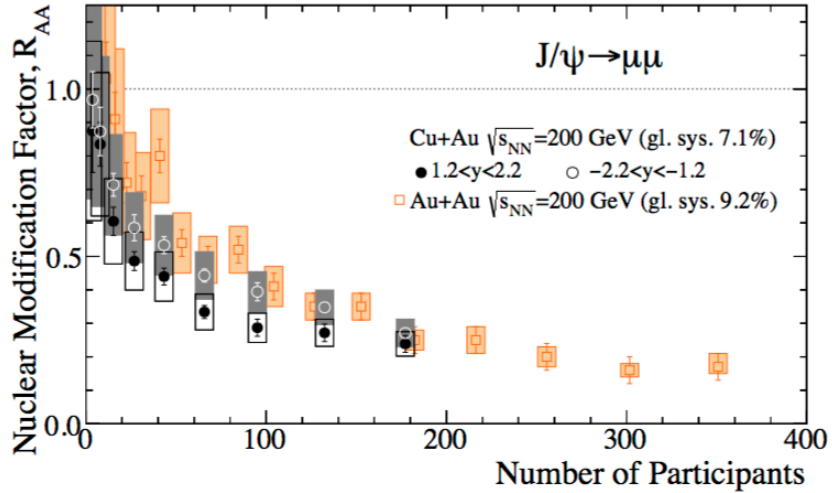


Figure 2.9: Nuclear modification factor, R_{AA} , measured as a function of collision centrality (N_{part}). Values for J/ψ at forward (Cu-going) rapidity are shown as open circles and at backward (Au-going) rapidity as closed circles. For reference, Au+Au data are also shown, averaged over forward and backward rapidities, as red squares [24].

direction. A measurement of the single muon R_{AA} in Cu+Au collisions will complement these measurements and will be an important constraint on theoretical work to come.

2.2 Heavy Flavor Flow

The nuclear modification factor serves as a tool to study energy loss within the produced medium. Azimuthal anisotropy of the final state spectra serves as another tool with which to study the medium, in particular, the viscosity of the flowing liquid produced in these collisions. Azimuthal anisotropy of heavy flavor single electrons has been measured at mid-rapidity in Au+Au collisions at PHENIX. Figure 2.10 shows the heavy flavor single electron v_2 reported in 2005 with theoretical models with and without charm flow[21]. While the error bars are large, the data are consistent with a scenario in which charm quarks are flowing within the medium.

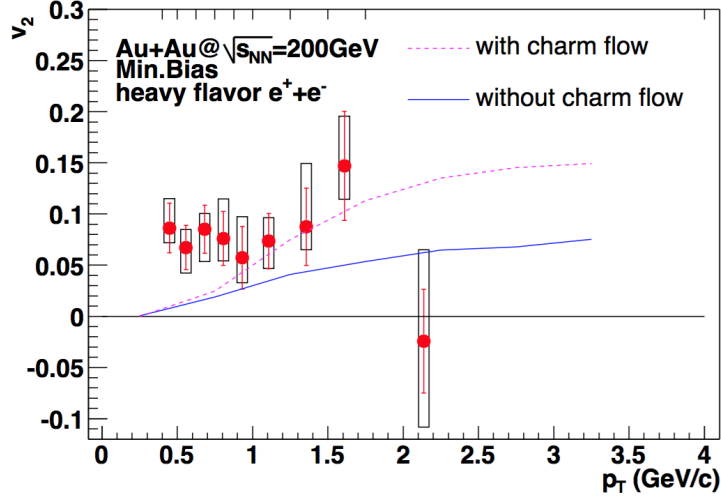


Figure 2.10: Comparison of heavy flavor single electron v_2 with various theoretical models [21].

The heavy flavor single electron v_2 was again measured by PHENIX in 2011 [10] in a comprehensive paper (PPG077) on azimuthal anisotropy and energy loss in Au+Au collisions. The reported heavy flavor single electron v_2 agrees with the above measurement within the statistical and systematic uncertainty. Figure 2.11 shows the result reported in 2011.

The single lepton anisotropy is an indirect measure of the charm quark flow, since the lepton carries only a fraction of the momentum of the parent hadron. The azimuthal anisotropy of reconstructed D-mesons in Au+Au collisions was reported by the STAR collaboration in early 2016. Figure 2.12 shows the measurement compared to the v_2 for light hadrons, also measured by STAR [37]. However, the accuracy of the measurement is not sufficient to deduce the level to which the single lepton v_2 is shifted in momentum. Nevertheless, it is clear that the heavy flavor quarks inherit some of the azimuthal anisotropy and that it is preserved to some extent in the azimuthal distributions of their single lepton daughters.

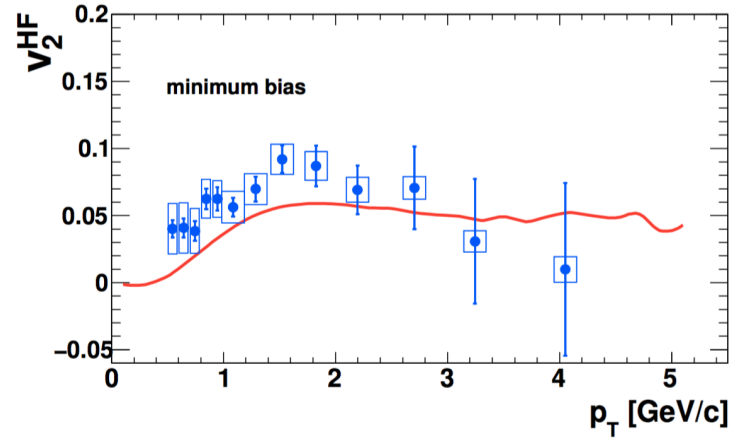


Figure 2.11: Comparison of heavy flavor single electron v_2 with a model calculation from Gossiaux and Aichelin [21].

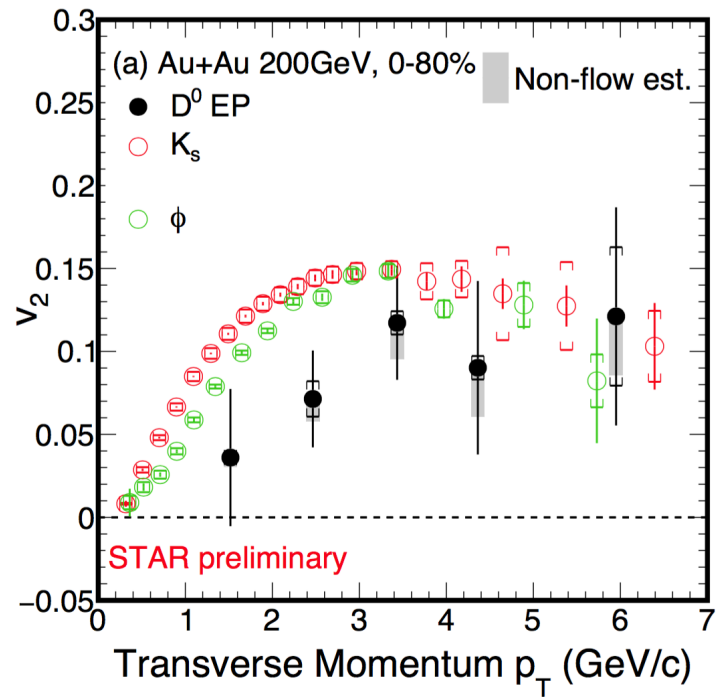


Figure 2.12: Measured v_2 for D^0 compared to that of light hadrons [37].

This is not necessarily unexpected, as the Au+Au system is generally thought to produce a QGP. However, as was discussed previously, the smaller Cu+Au system may include significant contributions from CNM effects. PHENIX has published results for identified pion, kaon, and proton v_1 , v_2 , and v_3 at mid-rapidity in Cu+Au collisions. Figure 2.13 shows the system size dependence of v_2 as a function of p_T for various centralities in Cu+Cu, Au+Au, and Cu+Au collisions [51]. The Cu+Au data fall in between the Cu+Cu and the Au+Au data, although it is interesting to note that the ordering appears to have switched in the most central bin. In the previous section, we saw that heavy flavor single electron R_{AA} as a function of N_{coll} showed a clear transition from the enhancement in the d+Au and peripheral Cu+Cu systems to the suppression and onset of hot nuclear matter effects in central Cu+Cu and Au+Au systems. Correspondingly, we see a clear dependence on system size here.

The Cu+Au collision system is unique in that it features heavy ions that are different sizes. In peripheral collisions, this leads to an inherent triangularity of the overlap region which is not present in the symmetric collisions. PHENIX has also measured v_3 in Cu+Au and Au+Au collisions, shown in Figure 2.14.

Recently, LHC has published a measurement of v_2 for single muons at forward rapidity in 2.76 TeV Pb+Pb collisions [19]. While the energy density is much higher in these collisions, and the p_T range is larger, the results inform this analysis as a first glimpse of the forward single muon v_2 in heavy ion collisions.

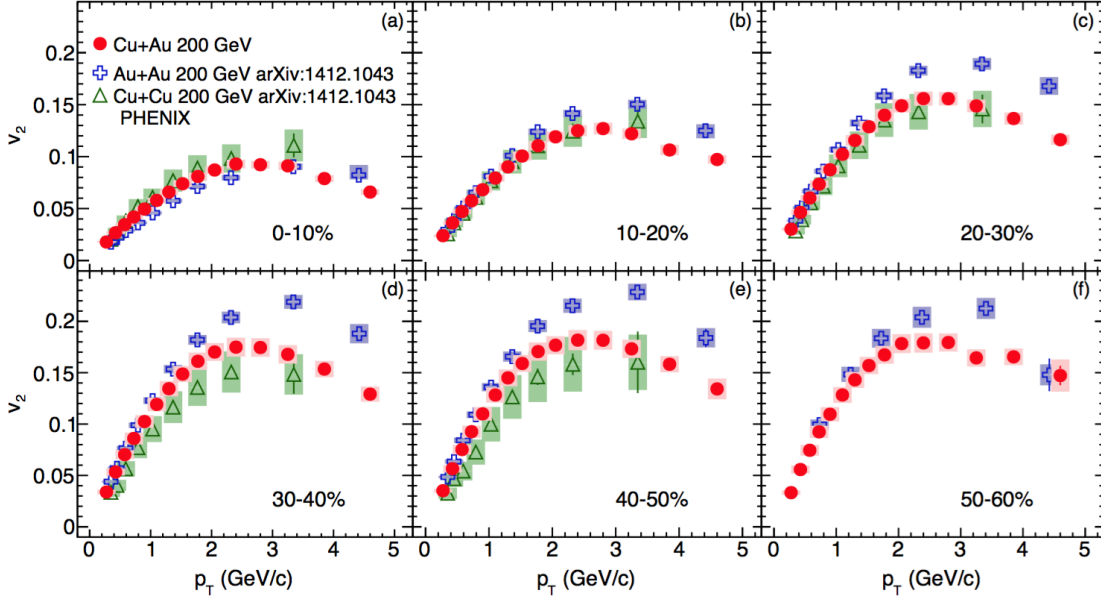


Figure 2.13: The second-order Fourier coefficients v_2 for charged hadrons is shown as a function of p_T . Cu+Cu data points plotted in green, Cu+Au is in red, and Au+Au is blue. Statistical uncertainty is plotted with bars and systematic uncertainty with shaded boxes. The top left panel shows the 0-10% centrality interval and subsequent panels show increasingly peripheral collisions in 10% intervals [51].

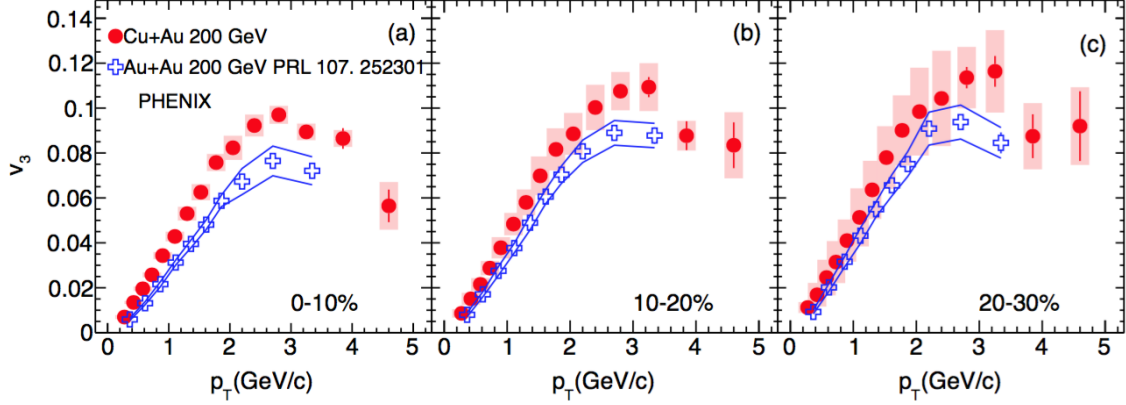


Figure 2.14: In each panel, the $v_3(p_T)$ coefficients are compared for the same centrality class, as marked in the figure. The symbols represent the measured $v_3(p_T)$ values, the uncertainty bars show the statistical uncertainties, and the shaded boxes indicate the systematic uncertainties for Cu+Au. The blue bounding lines show the systematic uncertainties for the Au+Au measurement. Cu+Au is represented with red data points and Au+Au with blue [51].

Figure 2.15 shows the measurement for various methods and in various centrality bins[19]. The first two p_T bins of these results are the relevant p_T range in relation to this measurement, and these results suggest a small but non-zero v_2 in the central 0%–20% and 20%–40% centrality bins. There is some discrepancy between the methods used, particularly in the 20%–40% centrality bin. The so-called *Scalar Product* method leads to a significantly lower v_2 in this bin.

The plethora of data taken and measurements made in the past 16 years have painted a general picture of the medium produced in these collisions in broad strokes, while generating much theoretical work. Suppression and flow in the forward Cu+Au system is a unique tool with which to study the physics of the QGP, and further distinguish between competing theories.

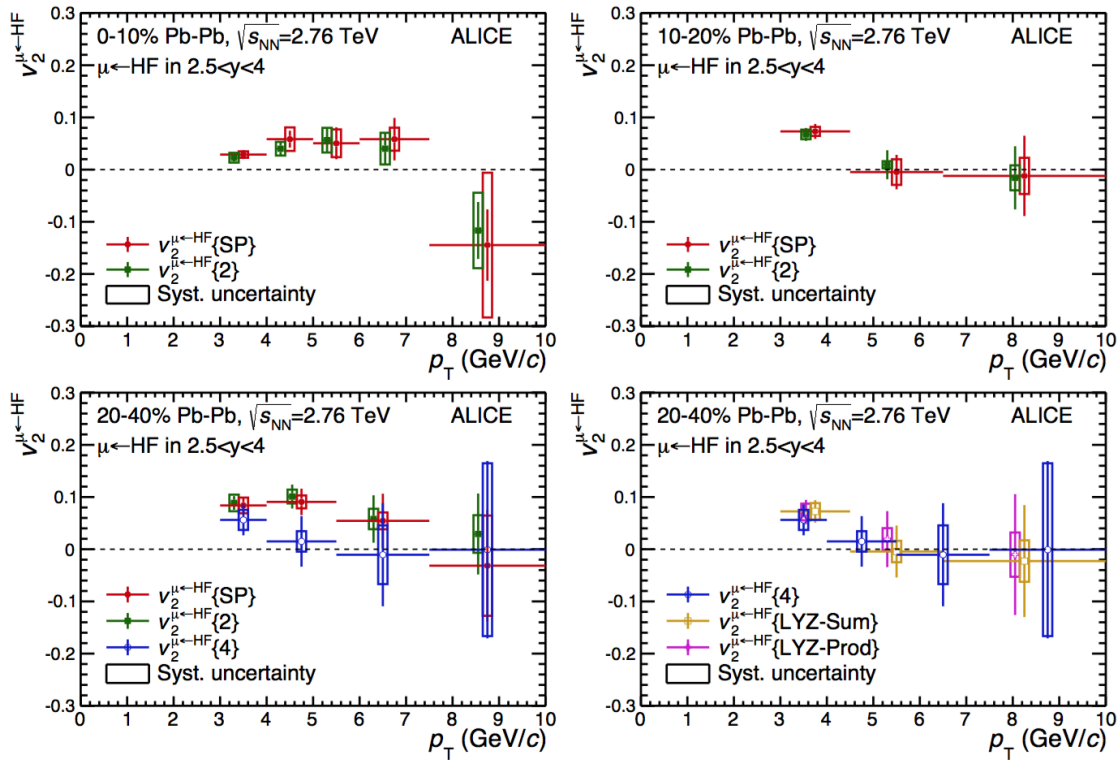


Figure 2.15: p_T -differential elliptic flow of muons from heavy-flavour decays, v_{HF} , in $2.5 < y < 4$ and various centrality intervals, in Pb+Pb collisions at $s_{NN} = 2.76$ TeV. The symbols are placed at the centre of the p_T interval and, for visibility, the points from two-particle Q cumulants and Lee-Yang zeros with product generating function are shifted horizontally [19].

Chapter 3

The PHENIX Experiment

3.1 The Relativistic Heavy Ion Collider

The Relativistic Heavy Ion Collider (RHIC) is located at Brookhaven National Laboratory (BNL) on Long Island, in New York. The purpose of the physics program at RHIC is twofold. One goal is the production of the predicted QGP and mapping of the QCD phase diagram by colliding heavy ions together over a range of collision energies. To this end, the facility has the ability to produce a variety of symmetric ($p+p$, $Cu+Cu$, $Au+Au$, and $U+U$) and asymmetric collisions ($d+Au$, $Cu+Au$), as well as proton-proton collisions which serve as a baseline for the heavy ion measurements. Another goal is addressed by the spin program which aims to solve the proton spin puzzle. The facility is equipped to collide polarized protons together for this purpose.

The acceleration of the heavy ions is a multi-step process involving a few different accelerators. The beams are created in two Van de Graaff generators and are accelerated by the Booster Synchrotron and then the Alternating Gradient Synchrotron (AGS). The heavy ions in these beams are stripped of electrons at various points of the accelerating process, until they become fully stripped and are injected into the RHIC rings at an energy of 10.8 GeV per nucleon [31]. The beams are then accelerated to the desired energy. The center of mass energy in heavy ion collisions ranges from 7.7 GeV per nucleon up to 200 GeV per nucleon. Proton-proton beams have been collided at a center of mass energy of 62.4 GeV,

200 GeV, and 500 GeV. Figure 3.1 Shows an aerial view of RHIC, with the various boosters used in the acceleration process labeled.

The two heavy ion beams are guided by large superconducting magnets through the beam tunnel in opposite directions, with crossing points at various locations along the 3.8 km circumference. The collisions take place at the crossing points. These crossing points are the sites for the various experiments at RHIC. Currently, there are only two running experiments, STAR and PHENIX. This analysis was done using the PHENIX detector.

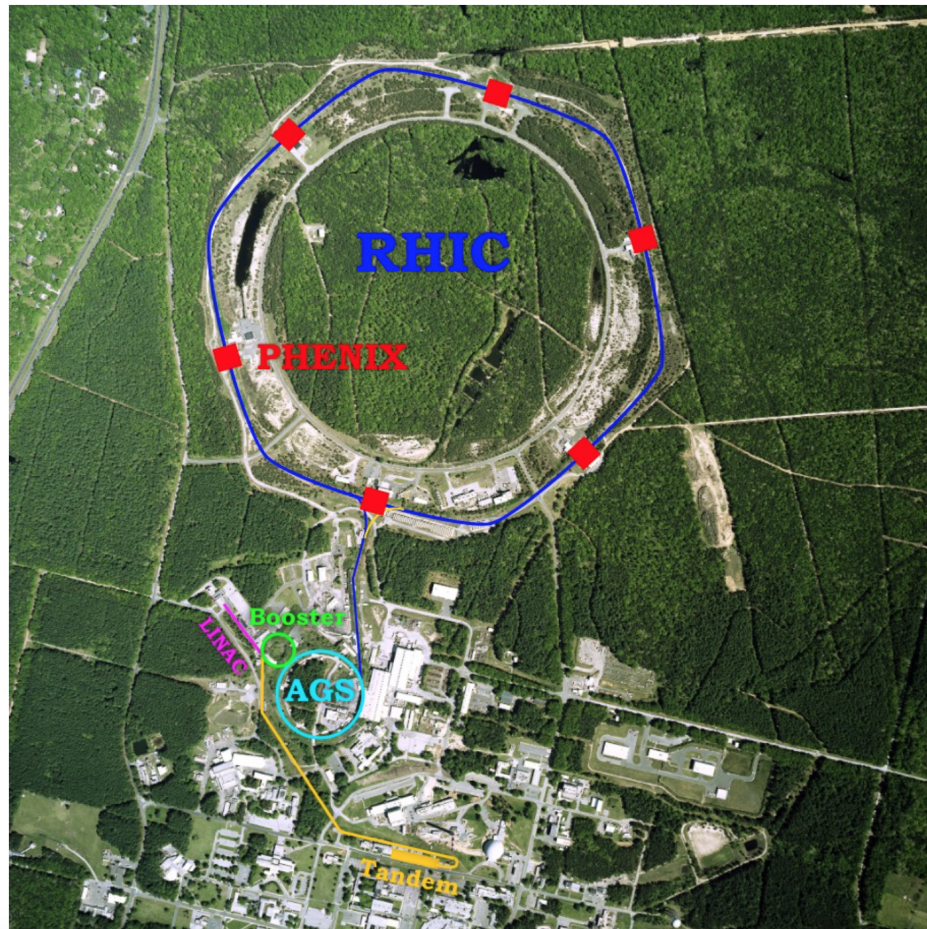


Figure 3.1: Aerial view of RHIC.

3.2 PHENIX

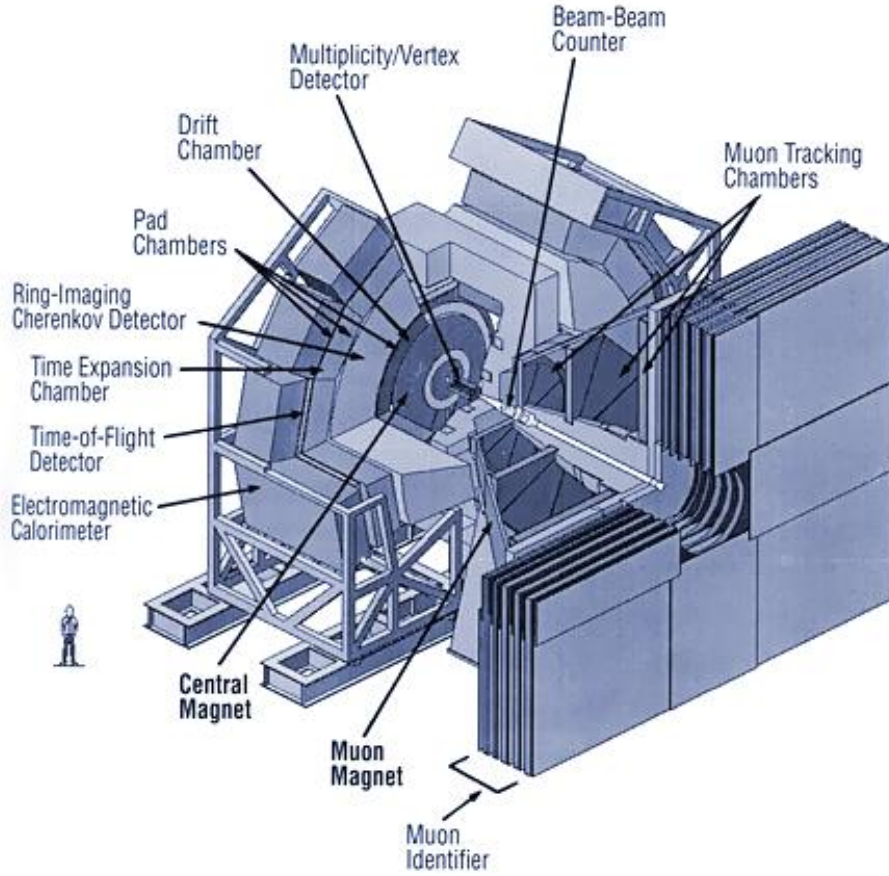


Figure 3.2: A cut-away view of the PHENIX detector [25].

The PHENIX detector is composed of many sub-detectors at varying locations with respect to the interaction region. The z -axis is defined as running along the beamline with the positive direction pointing north. The azimuthal angle, ϕ , and the pseudorapidity, η , are used to define the laboratory frame of reference. Using these coordinates, we can define four different regions of the detector, corresponding to the directions north, south, east, and west. The central arms refer to the east and west detectors, while the muon arms refer to the north and south detectors. Figure 3.2 shows a cut-away view of the PHENIX central arms and one of the muon arms. Figure 3.3 shows the PHENIX coordinate system. The x -axis is perpendicular to the RHIC ring with the positive direction pointing outward (away from

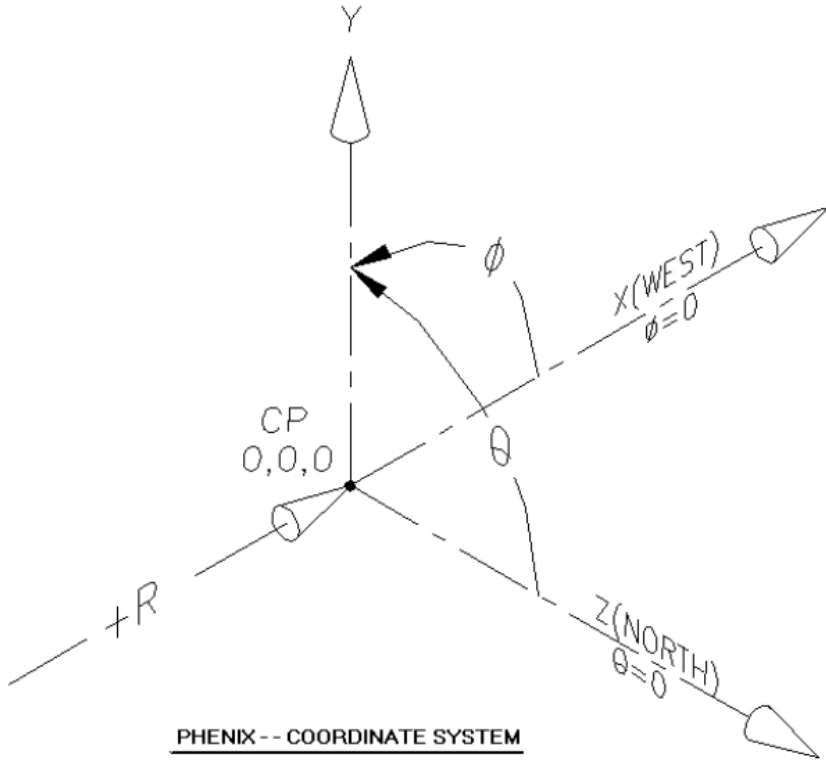


Figure 3.3: Phenix coordinate system.

the center of the ring). The y-axis is the vertical axis, with the positive direction pointing up. The z-axis runs along the beamline.

There are two global detectors to be used in most, if not all, analyses. These are the Beam-Beam Counter (BBC) and the Zero-Degree Calorimeter (ZDC). These detectors are used to measure global properties about each collision, giving information about impact parameter, collision vertex position, and reaction plane, as well as being the minimum bias trigger used to store data. Other, more sophisticated, triggers are used in conjunction with the minimum bias trigger to trigger on specific physics processes.

The central arms are positioned at mid-rapidity, or pseudorapidity near zero. The central arms include various tracking and particle identification detectors, as well as electromagnetic calorimeters used to measure energy deposition within materials with known energy loss properties.

At forward rapidities sit the muon arms, the main detectors used in this analysis. The muon arms are comprised of a muon tracker, used for momentum measurements, and a muon identifier.

3.2.1 Central Arms

The PHENIX central arms (shown in Figure 3.4) cover a pseudorapidity, $|\eta| < 0.35$, which corresponds to a polar angle $70^\circ < \theta < 110^\circ$. Each arm covers 90° in azimuth. The Drift Chambers (DC), Ring Imaging Cherenkov Detectors (RICH), Pad Chambers (PC), Aerogel Cherenkov Counter (Aerogel), Time-Of-Flight East and West (TOF-E and TOF-W), and Electromagnetic Calorimeters (PbSc and PbGl) comprise the central arms. These detectors are used for momentum tracking (DC and PC) and particle identification (Aerogel, TOF-E and TOF-W, RICH, PbSc and PbGl).

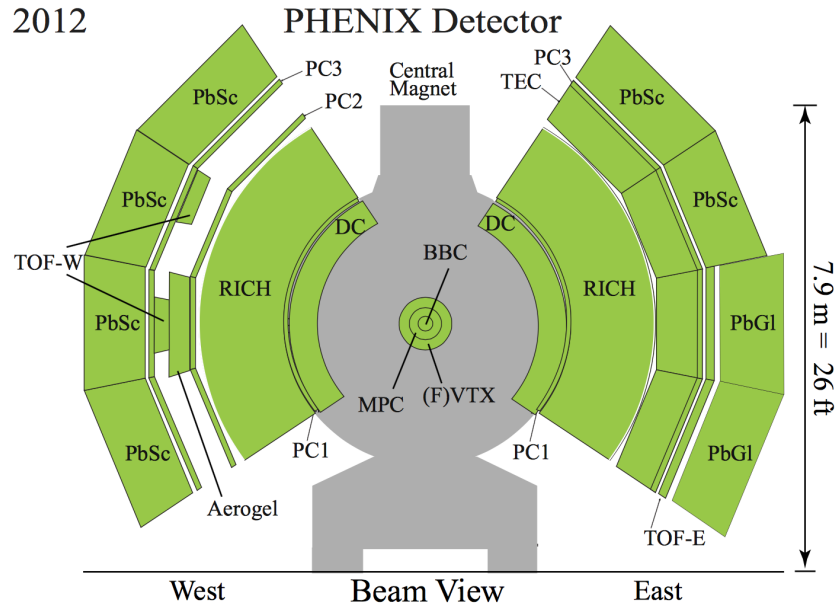


Figure 3.4: Beam line view illustration of the PHENIX central arms circa 2012.

3.2.2 Muon Arms

The PHENIX muon arms (shown in Figure 3.5) are located at forward rapidities. They cover a pseudorapidity, $1.2 < |\eta| < 2.4$. This corresponds to a polar angle of $146^\circ < \theta < 170^\circ$ for the south arm and $10^\circ < \theta < 34^\circ$ for the north arm. They cover a full 2π of azimuth, which makes them particularly suited for azimuthal anisotropy measurements. The muon arms were designed for the purpose of studying vector mesons which decay via the dimuon channel, heavy flavor mesons which decay muonically, as well as Drell-Yan processes. Muon identification is achieved by taking advantage of the relatively small cross section of muons traveling within absorber material as compared to the background hadrons. All candidates pass through more than a meter of steel before reaching the back of the Muon Identifier (MuID). This large amount of steel filters a high number of hadrons while most muons pass through, leaving behind a highly purified sample of muon tracks.

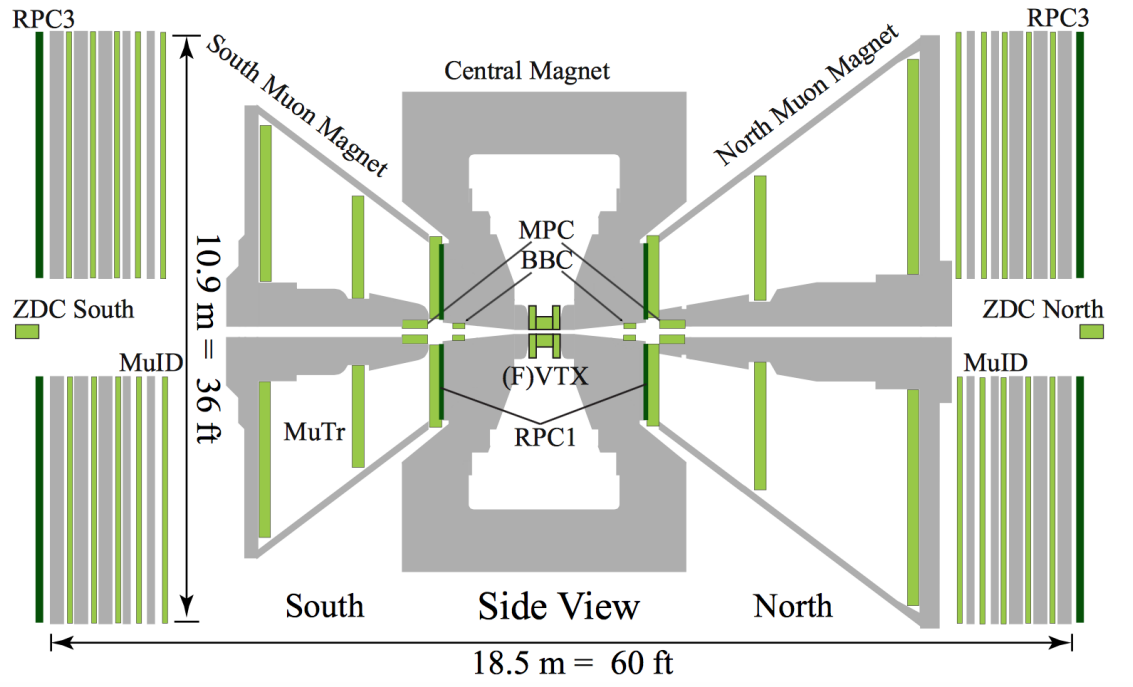


Figure 3.5: Elevation view illustration of the PHENIX muon arms circa 2012.

Muon Tracker

The muon tracker (MuTr) refers to the tracking detectors that sit on the north and south sides of the interaction point. Each detector consists of three “stations”, where the first two stations have three “gaps” and the third station has two gaps. A gap consists of an anode layer sandwiched between two layers of cathode strips. The volume between the two cathodes is filled with a mixture of argon, carbon dioxide, and tetrafluoromethane (CF_4) with a ratio of 5:3:2. Each station is then split into “octants” for the purpose of signal readout.

Anode wires are aligned perpendicular to the radial vector. One plane of cathode strips is aligned perpendicular to the anode wires, or parallel to the radial vector. The second plane of cathode strips is aligned at a small angle with respect to the first cathode plane. This provides improved azimuthal resolution [57] while rejecting ghost cathode hits [20]. The charged particles which pass through the tracker ionize this gas mixture, depositing charge onto the cathodes. The charge distribution across the cathodes are fit to create a “hit” with a particular position. Figure 3.6 shows a picture of two octants of cathode strips.

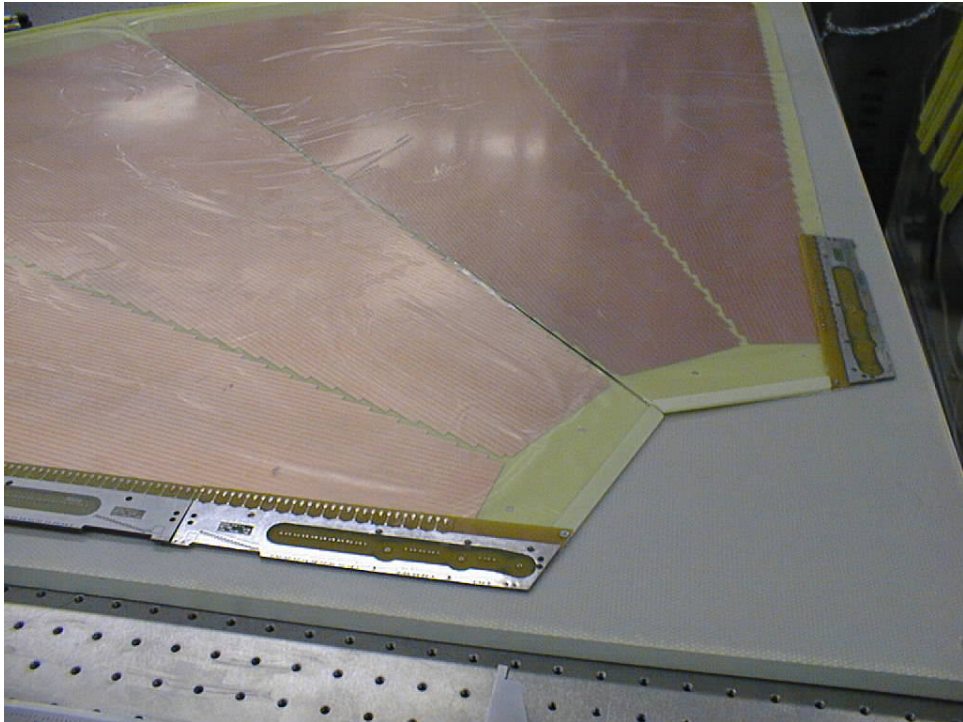


Figure 3.6: Close-up view of two octants of cathode strips before installation.

Each of the muon tracker detectors (north and south) are placed inside a large magnet, dubbed the “muon magnets”. The magnet creates a radial magnetic field in order to bend the trajectory of the charged particles which pass through the detector. The radial magnetic field causes the particles to bend in the phi direction, creating a spiral trajectory within the detector. The magnitude of the momentum of the particle is determined from the simple equation

$$|\vec{p}| = q\vec{B} \cdot \vec{r}. \quad (3.1)$$

Figure 3.7 shows a schematic diagram of the south arm muon magnet with the stations positioned inside.

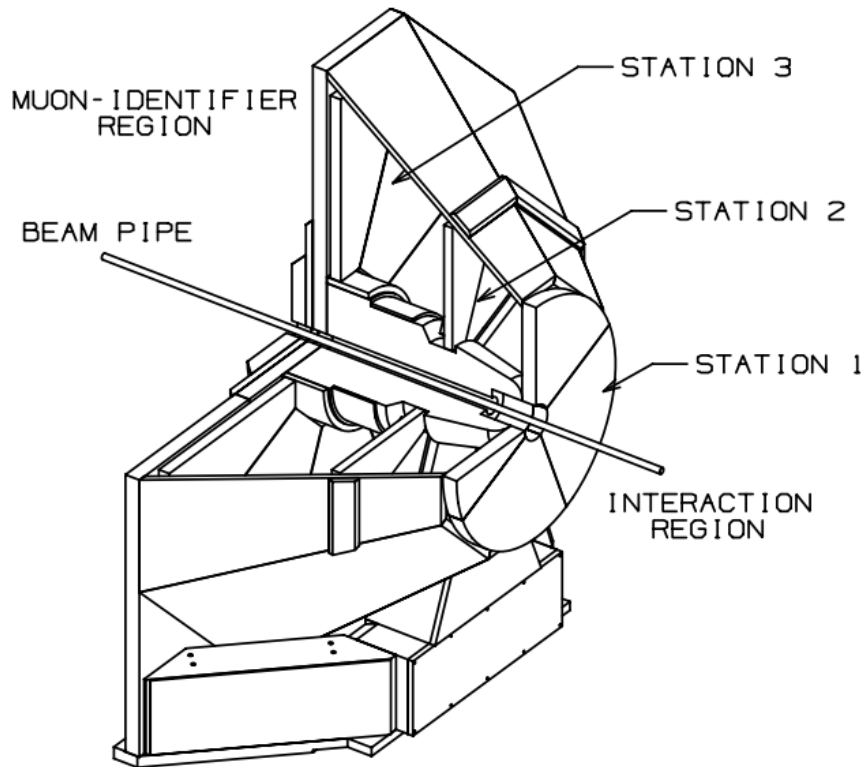


Figure 3.7: MuTr schematic diagram showing the position of the stations with respect to the interaction point and the beam line.

Muon Identifier

The muon identifier (MuID) uses a design similar to that of the MuTr. That is, ionization of gas is used to create hits in the detector. However, the position resolution of the MuID is not as precise as the MuTr. This is because momentum measurements are not made in the MuID. Rather, the MuID is used for rejecting hadron tracks which have passed through the MuTr, while allowing muons to pass through.

The MuID consists of five planes, or “gaps”, of Iarocci tubes with planes of absorber material (steel) in between. The Iarocci tubes are made of PVC channels with a square cross-section, lined with a graphite coat which forms the cathode, while a $100 \mu\text{m}$ Cu-Be anode wire runs down the center. The tubes are arranged into “two-packs” (as seen in Figure 3.8). The staggered design of the two-packs improves the efficiency of the detector. The two-packs are then arranged into panels (as seen in Figure 3.9). Each panel consists of a number of vertical and horizontal two-packs. Therefore, a particle passing through the detector can leave, at most, two hits in any particular gap.

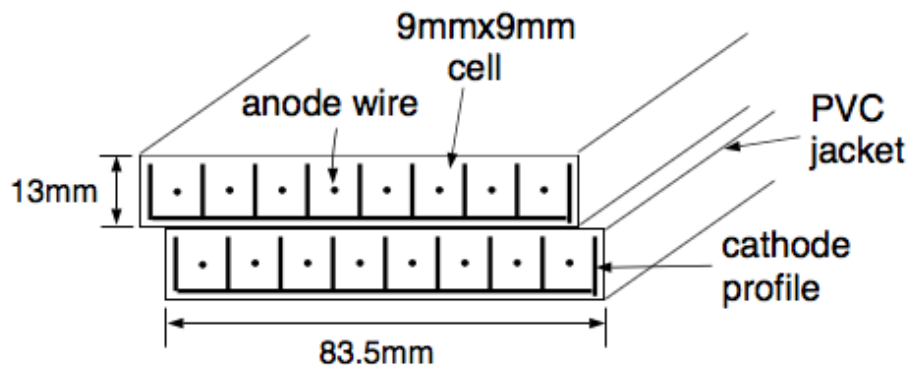


Figure 3.8: A MuID two-pack.

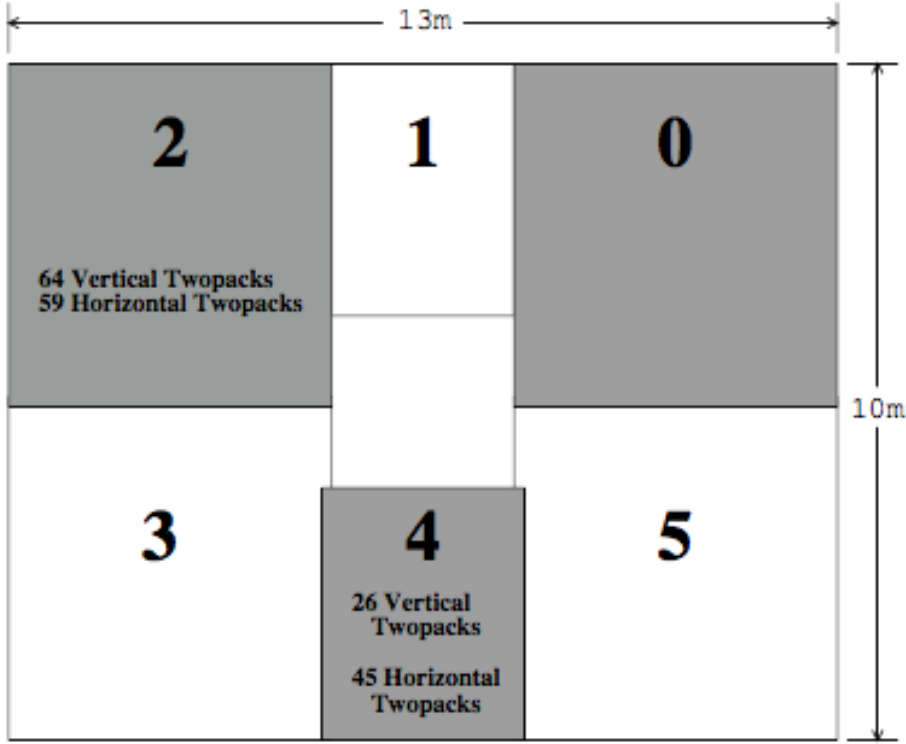


Figure 3.9: MuID panels.

The five gaps of the MuID are labelled from 0 to 4, such that Gap 4 refers to the last possible gap. The full pion rejection of the absorber material before Gap 4 of the MuID was about 2.5×10^{-4} [11], prior to the installation of additional nose cone absorber material at the beginning of Run-12. Figure 3.10 shows the integrated interaction length (prior to the installation of the new absorber material) plotted as a function of distance from interaction point. With the installation of the new absorber material, the pion rejection is now roughly 3.5×10^{-5} .

Using hits in the planes of the MuID, “roads” are reconstructed and matched to the tracks of the MuTr. In this way we create a pool of muon candidates which must pass a number of track quality cuts before we can include them in the muon analysis. Tracks that reach Gap 4 are considered highly likely to be muon tracks.

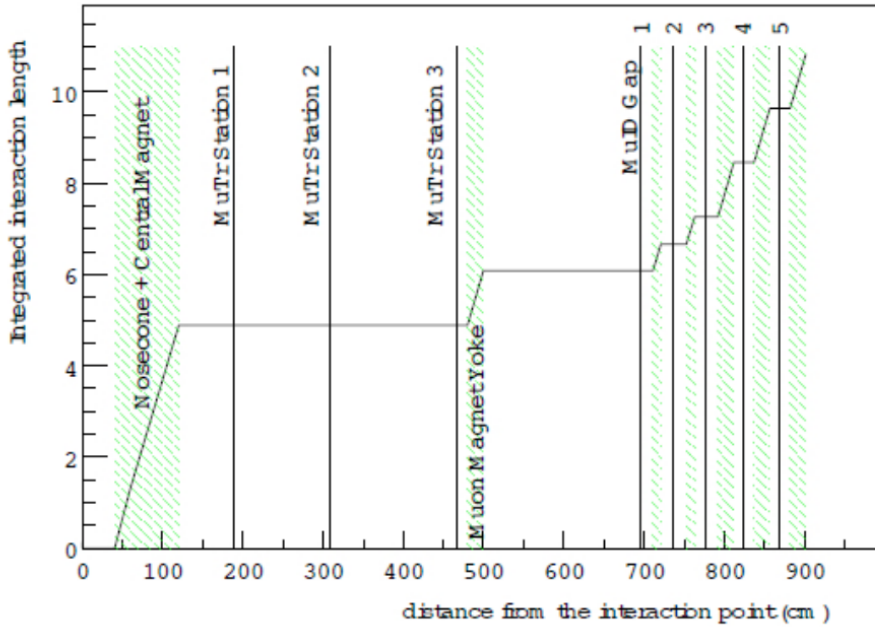


Figure 3.10: Integrated interaction length as a function of distance from interaction point [28].

3.2.3 FVTX

The Forward VerTeX detector (FVTX) was commissioned for Run-12. There is a detector located in front of the muon magnets on both the north and south side. These detectors are designed to improve the resolution of event vertex measurements, as well as secondary decay vertex measurements. They also aim to improve on the tracking done in the muon arms by providing hit points closer to the interaction point [46]. The addition of more absorber material in front of the MuTr leads to a reduced resolution by increasing the multiple scattering of particles in the absorber. The improvement on tracking provided by the FVTX is significant, and may account for the loss in resolution due to the additional absorber.

The separation of charm and beauty contributions to heavy quark measurements is an important step in the characterization of heavy quark production and interactions. This separation can be achieved via improved secondary vertex measurements. The contributions are separated by taking advantage of the different lifetimes of heavy flavor mesons (see Table

1.1). With a resolution of approximately $100\ \mu\text{m}$ in the r-z plane [46], the separation of heavy flavor into charm and beauty may be possible.

Another application, particularly useful in this analysis, is in measurements of the reaction plane. Previously, reaction plane measurements were made using the Reaction Plane Detector (RXP). However, the RXP was removed to make room for the VTX/FVTX detector. The FVTX can make improved reaction plane measurements by increasing azimuthal resolution on tracks originating from the event vertex [46].

3.2.4 Global Detectors

Complementary detectors exist in addition to the detectors that make up the central and muon arms. These detectors are used to measure global observables of a given nucleus-nucleus collision. The Beam-Beam Counter (BBC) and Zero-Degree Calorimeter (ZDC) serve this purpose.

The BBC (North and South) detectors are positioned at higher rapidity (closer to the beam line) than the muon arms, with an acceptance of roughly $3.0 < |\eta| < 3.9$. They are circular arrays of quartz crystals followed by photomultiplier tubes which collect the Cherenkov radiation produced by charged particles within the quartz. The BBC detectors are positioned coaxial with the beamline. The photomultiplier tubes are detect charged particles at very forward angles. The charge deposited in the BBC (and the timing thereof) is used to calculate the collision vertex (along with the FVTX and VTX detectors as of 2012) as well as providing information used for the *minimum bias* trigger.

The ZDC is a hadron calorimeter positioned 18 meters away from the interaction point. Charged particles, as well as the beam, are directed away from this region by the magnets which direct the beam. Neutral particles which are liberated from the spectator portion of the colliding nuclei in, continuing in a straight line towards the ZDC. The ZDC serves to measure the number of neutral spectators emerging from the interaction region after a collision. Figure 3.11 illustrates the difference between participants and spectators.

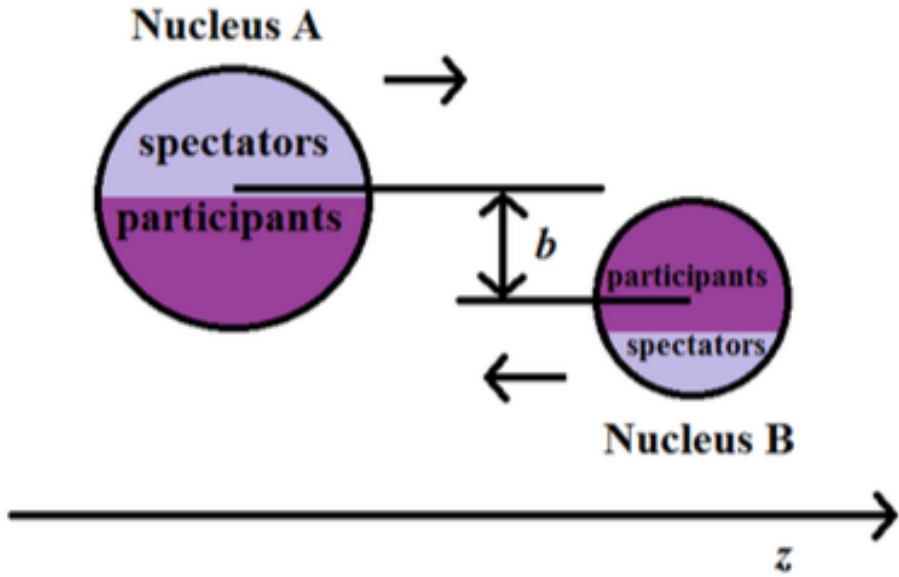


Figure 3.11: An illustration depicting the participants and spectators of a heavy ion collision. The participants remain mostly in the interaction region as they interact, while the spectators continue along the z -axis [32].

3.3 Event Classification

A collision, or “event”, which takes place within the Interaction Region (IR) of PHENIX will create a number of outgoing final state particles. These particles are detected by the various PHENIX subsystems that make up the PHENIX detector. The global detectors are used in conjunction with the various tracking detectors to reconstruct and classify these events in order to provide high quality data for analysis. Events are primarily classified by the position of the colliding nuclei relative to each other (centrality), the location of the collision along the beam access (vertex), and also by the likeliness of the existence of rare processes within the event (trigger).

3.3.1 Centrality

There are many quantities of interest which describe a heavy-ion collision. The impact parameter, number of participant nucleons, and number of nucleon-nucleon collisions are

all particularly useful in the classification of a given event. However, these quantities are not directly observable. Instead, events are classified by their “centrality” which allows one to estimate these quantities using various models. The separation of events into centrality classes assumes that the centrality of a collision is related to the charged particle multiplicity measured within said event [40]. Referring to Figure 3.11, one can see that the number spectators should increase monotonically with the impact parameter. In order to measure the centrality in PHENIX, charged particle multiplicity in the BBC is used to measure the centrality of collisions. Figure 3.13 illustrates the concept. [40]

A Glauber model simulation is commonly used to extrapolate centrality, number of participants (N_{part}), and number of nucleon-nucleon collision (N_{coll}) values [40]. Inputs to the Glauber simulation include the nuclear charge densities of the colliding nuclei as well as the inelastic nucleon-nucleon cross sections. Figure 3.12 shows the measured charge density distributions for Cu and Au, as measured in low energy electron scattering experiments [40]. With these inputs, a simulation is run in which the nuclei consist of uncorrelated nucleons projected into a plane transverse to the beam. The nuclei are then collided given some impact parameter, b .

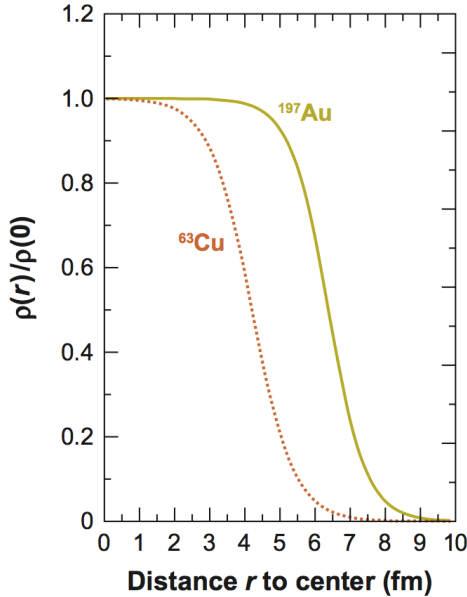


Figure 3.12: Charge density distributions for nuclei used at RHIC [40].

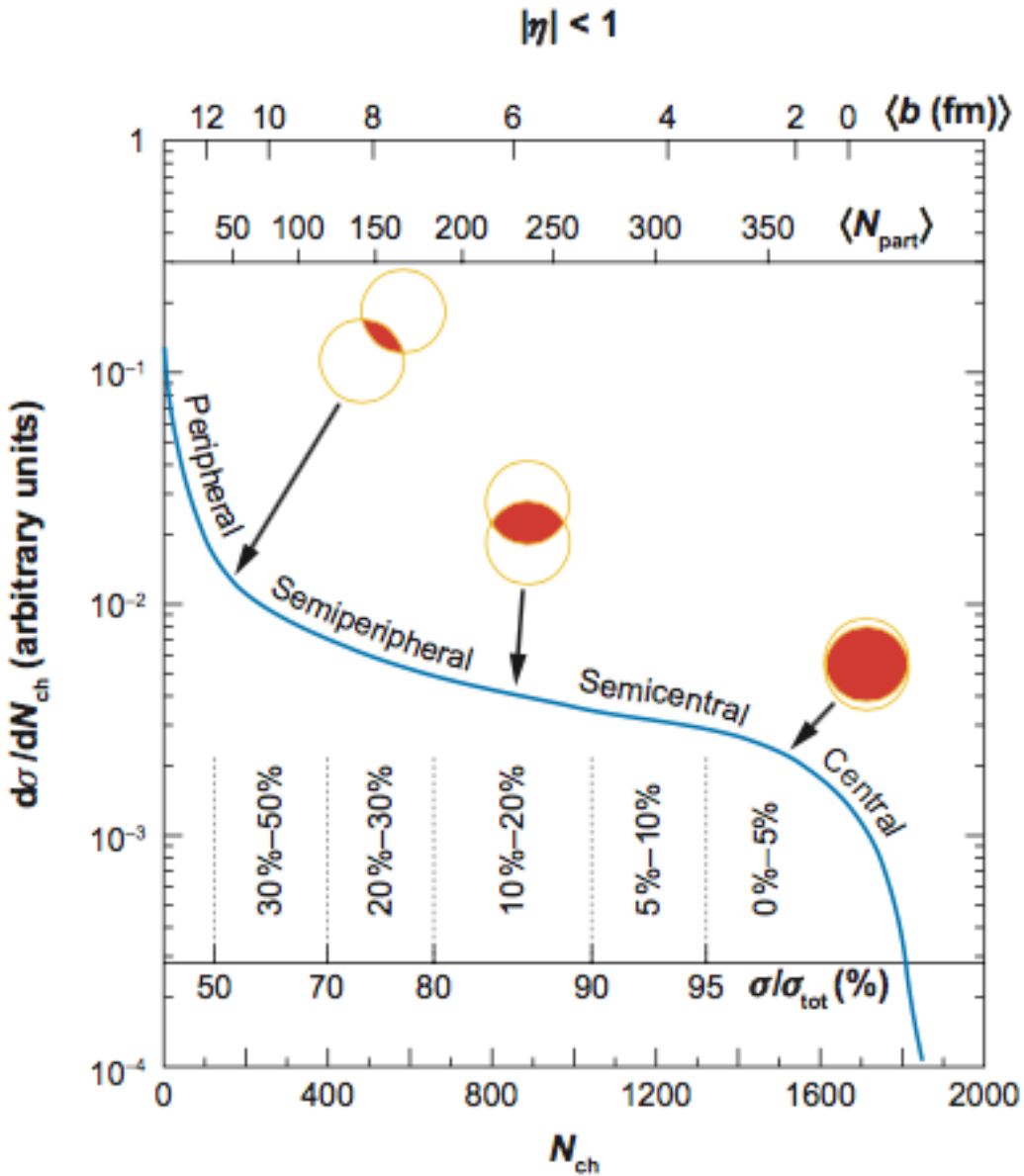


Figure 3.13: A plot showing a charged particle multiplicity distribution with various illustrations depicting the centrality of collisions. Peripheral collisions are more common, hence the rise in final-state yield for decreasing centrality [40].

3.3.2 Collision Vertex

The z -coordinate of the collision vertex (z -vertex) is another important observable in characterizing events in PHENIX. Events which occur far from the center of the detector are less reliable in the sense that detector response will be asymmetric. For this reason, most analyses make a minimum cut at ± 25 cm (or smaller) from 0 on the z -axis (defined as the center of the PHENIX detector). Furthermore, the particular rapidity interval of a detector changes slightly as a function of the z -vertex. Figure 3.14 shows the z -vertex event distribution in the run 12 Cu+Au data set.

In the context of the single muon analysis, the z -vertex is inherently tied to the background subtraction of muons which decay from light hadron sources. For a given z -vertex, the farther away a particular detector is from said vertex, the more likely a light hadron is to decay. Therefore, the distribution of light decay muons increases as a function of distance between the detector and the vertex. This will be discussed in detail in Chapter 4.

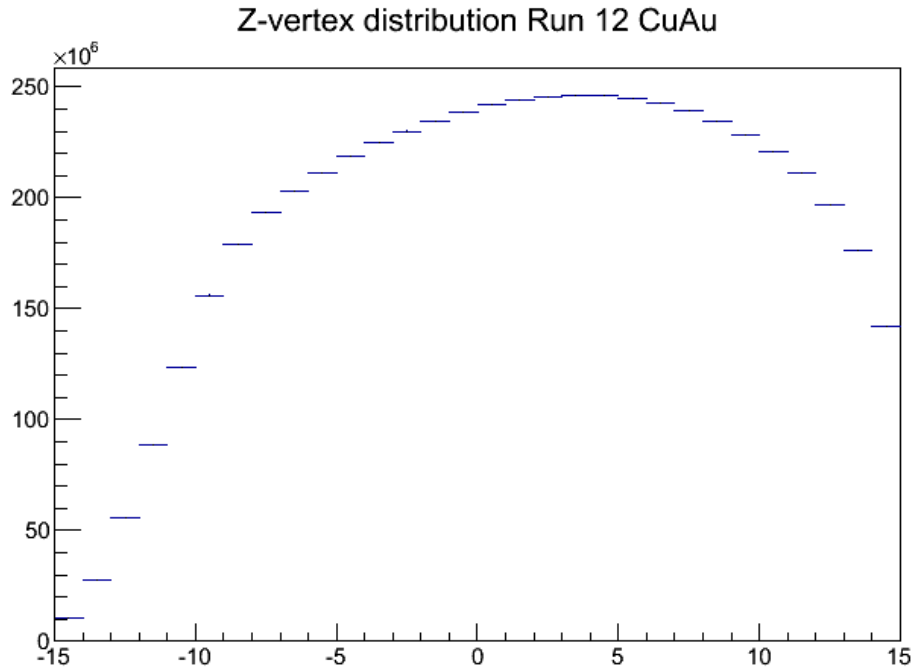


Figure 3.14: Z-vertex distribution in the run 12 Cu+Au data set.

3.3.3 Triggers

In order to provide more useful data for the Central Arm, PHENIX implemented a narrow vertex trigger for the Run 12 Cu+Au data-taking period. The trigger is based on real-time measurements of the event vertex using the BBC. Events which fall outside of ± 10 cm of the origin of the PHENIX coordinate system are scaled down in order to capture the most narrow vertex events possible. This trigger has a large impact on this analysis. The extent to which the analysis is impacted and the steps taken to correct for any trigger inefficiency will be covered in Chapter 4.

3.4 Track Reconstruction

Track reconstruction in the muon arms is achieved with the MUTOO reconstruction package. MUTOO is an object oriented code framework, written in C++, which runs within the PHENIX Fun4All framework. The MUTOO tracking framework is designed to handle the large hit multiplicities typical of a heavy ion collision, while remaining efficient with regards to computing and time requirements.

3.4.1 Tracking in the MuID

Tracking in the muon arms begins in the MuID. The tracking starts with “hits” in the MuID, defined by a signal from a given two-pack. Adjacent hits are grouped into “clusters”. As was discussed previously, the two-packs are aligned in both horizontal and vertical configurations. The clusters are then grouped into ”roads” in the 2D x-z and y-z planes, using the vertical and horizontal two-pack configurations, respectively. The tracks originating from the interaction point are nearly perpendicular to the MuID planes, and do not bend as in the MuTr since there is no magnetic field applied in the MuID. For this reason, the roads in the x-z and y-z planes are fit to a straight line. The roads within the 2D planes are then paired with each other to form 3D roads within the MuID. The pairing of roads depends on a number of different criteria to ensure the validity of each pairing. For a given pair to be accepted:

- The last gap of the roads within the pair must not differ by more than one.

- Each of the roads must have hits recorded in at least two gaps.
- The number of hits of each road within a pair cannot differ by more than two.
- Each road cannot have gaps prior to the last gap that did not record a hit.

3.4.2 Tracking in the MuTr

Tracking in the MuTr starts with the cathode strips. Ionization charge is collected by the cathode strips causing them to produce a hit signal. Adjacent cathode strips are then grouped into “clusters” (not to be confused with the clusters found in the MuID). The stereo angling of the adjacent cathode planes allows for the determination of 2D “hit” location within a particular gap (see Figure 3.15). The hits in each station are then fit with a straight line, creating track “stubs”. The straight line fit is justified within a given station because of the small amount of bending that occurs within each station. In the next step, stubs from Station 3 are matched to the roads found in the MuID. The track seeds formed by this matching are then extrapolated to Station 2 of the MuTR using a straight line. While the bending of tracks is significant over this range, there is, as of yet, no momentum information with which to estimate the amount of bending. The seeds are then matched to track stubs within Station 2. With the matched found in Station 2, a crude momentum estimate can be made. This estimate is used to approximate the amount of bending of the track in order to more accurately match to track stubs in Station 1. After the tracks have been fully extrapolated to Station 1, another crude momentum estimate is applied in order to correct for the approximations made earlier in the tracking algorithm.

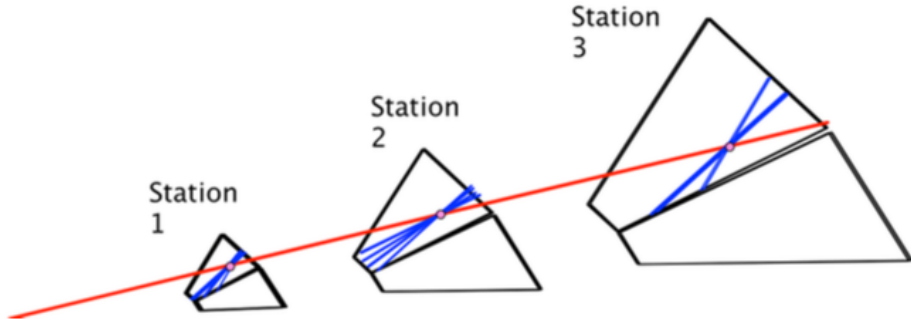


Figure 3.15: Illustrated depiction of a track within the MuTr. The blue lines represent cathode strips within an octant of each station [31].

At this point, many tracks will have some hits in common. These tracks are then fit with a smooth curve, each having a χ^2/NDF value. For a shared hit, the tracks with larger χ^2 or lower number of hits elsewhere will be rejected. The last step is to apply a Kalman fit [57] to the remaining tracks. The Kalman fit is used to extrapolate the tracks to the event vertex. The track objects contain the measured momentum and position information at each station in the MuID, as well as projected momentum and position information at the event vertex as well as the first gap of the MuID.

3.5 Data Aquisition

The PHENIX data aquisition system (DAQ) consists of a number of different components which are listed here:

- Front-End Modules (FEM) collect and digitize the analog signal from a given detector.
- Data Collection Modules (DCM) collect the the data sent by the FEMs and repackage the data into more efficient formats.
- Sub-Event Builders (SEB) collect the repackaged data from the DCMS.
- Assembly and Trigger Processors (ATP) assign an event number for each event, then collect the event data from the SEBs holding the data.
- Buffer Boxes hold the event data sent by the ATPs.

- High Performance Storage System (HPSS) collects the event data from the buffer boxes where it is stored on tape.

Figure 3.16 shows an illustrated schematic of the data flow from collisions in the interaction region to data that is stored on tape.

The DAQ is optimized for the high collision rates and high multiplicity events characteristic of heavy ion collisions at RHIC. The heavy ions within each beam are grouped together in “bunches”. The beams cross each other at the interaction regions described previously. A “beam crossing” refers to the time when a bunch from each beam is passing through the interaction region and has a chance to produce a collision. A beam crossing occurs every 106 nanoseconds, although not every beam crossing produces a collision and not all collisions produce interesting physics. In addition, the DAQ can only operate with a finite bandwidth. For these reasons, triggers are used to maximize the fraction of the total cross section that is recorded, while optimizing the amount of interesting physics data that is taken. The process begins with Local Level-1 (LL1) triggers. LL1 triggers are used to create an *accept* or *reject* flag for a given beam crossing. Some examples of LL1 triggers are the minbias trigger provided by the BBC, or the muon trigger provided by the MuID. The LL1 triggers are collected by the global level-1 (GL1) trigger which ultimately decides whether or not the event is recorded. The GL1 trigger sends a global accept or reject flag

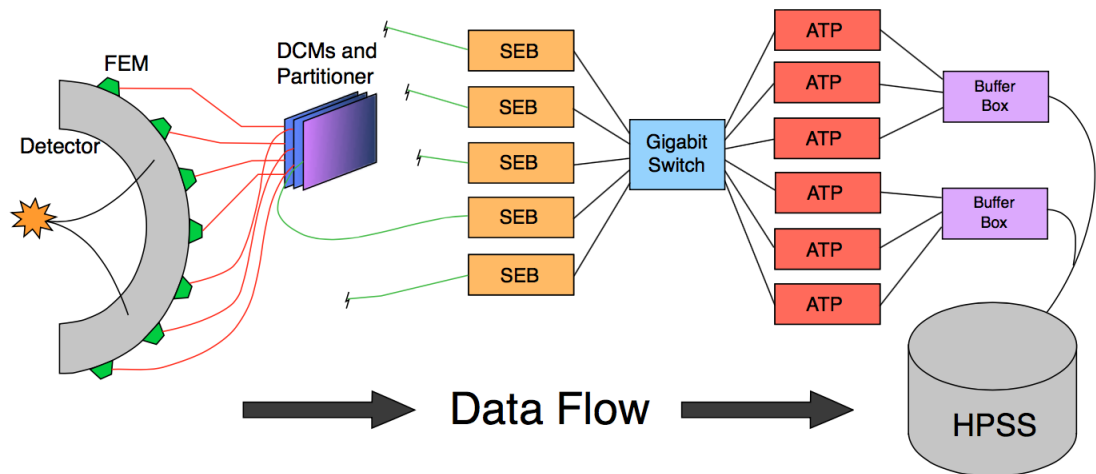


Figure 3.16: An illustration depicting the flow of data from the detectors to permanent storage on tape [57].

to the FEMs which, given an accept flag, will send their data to the DCMs. The accept flag from the GL1 initiates the data flow described above. Data stored in HPSS is then used for analyses such as this one.

Chapter 4

The Single Muon Analysis

4.1 Overview

The heavy flavor single muon yield measurement described in this chapter is based on a similar analysis done by the RHIP group here at the University of Tennessee [11]. The analysis begins with the inclusive muon candidates, as identified by the MuID. The sample is a combination of the heavy flavor single muon signal as well as a few different sources of background.

The sample of candidates contains both muon tracks as well as hadron tracks, with the muon tracks originating from heavy flavor hadrons and from light hadrons. Light hadrons, which decay in flight between the collision vertex and the front of the muon arm or which decay within the detector or steel absorber, can produce muons, referred to as “decay muons”, which are then correctly identified by the MuID as muon candidates. However, these decay muons are of no interest and must be subtracted in the final heavy flavor measurement. The decay muons form the largest source of background for this measurement. Since there is no sure way to distinguish a decay muon from a heavy flavor muon on a track by track basis, their contribution must be subtracted statistically. The decay muon contribution is estimated using Monte Carlo simulations.

The decay lengths of the various light hadrons (on the order of meters) are much longer than the distance from the collision vertex to the front absorber of the muon arms. The heavy flavor hadrons, on the other hand, have much shorter decay lengths (on the order of

hundreds of microns). Due to the wide z-vertex distribution accepted by the muon arms, the inclusive muon yield will exhibit a linear z-vertex dependance. Light hadrons which originate further from a given muon arm have more time to decay before reaching the front of said muon arm. Therefore, there are more decay muons coming from collisions which happen further from the detector. For example, the south arm, which lies along the negative z-axis, will find more muon candidates in collisions with a postive z-vertex ($z_{vtx} > 0$) than collisions with a negative z-vertex ($z_{vtx} < 0$). The north arm, conversely, will find more muon candidates in collisions with a negative z-vertex. The z dependance of the decay muon yield is used to constrain the decay muon contributon.

Many of the light hadrons produced in the collision will not decay. While the steel absorber within the muon arm rejects a large fraction of these hadrons, the large number of hadrons ensures that a non-negligible number of hadron tracks will penetrate to Gap 4 of the MuID and be incorrectly tagged as muon candidates. These hadron tracks are referred to as "punch-through hadrons". As with the decay muon tracks, it is not possible to distinguish the hadron tracks which penetrate to Gap 4 from the muon tracks. This contribution is also subtracted statistically, with a Monte Carlo simulation being used to estimate the contribution.

The hadron tracks come with an additional complication relative to the decay muon tracks. The punchthrough hadron tracks originate from the collision vertex. Therefore, they do not exhibit the linear z-vertex dependence that the decay muons do. However, there is another way to constrain the punchthrough contribution. Tracks which penetrate to Gap 4 of the MuID are considered muon candidates. However, many tracks in the muon arms are stopped in shallower gaps. These tracks mostly consist of punchthrough hadrons. In order to correctly estimate the punchthrough tracks in Gap 4, a Monte Carlo simulation is performed which is "tuned" to the measured yield in Gap 3. The simulated yield in Gap 3 is first normalized to the yield measured in the data by requiring that the tracks per event in each is equal. The normalization factor is the tracks per event in data divided by the tracks per event in simulation. A further fine-tuning is achieved with a p_T -reweighting method. The input spectra for the simulation is reweighted to better match the data. The initial normalization in Gap 3 is simply used to center the p_T dependent weights around 1. The

reweighting is done iteratively. Once the relative weights between consecutive iterations are consistant with unity, the reweighting has converged. The weights are determined by the data to simulation yield ratios in Gaps 2 and 3, and by the z-vtx dependent slope ratios in Gap 4. This method allows a statistically accurate prediction of the punchthrough contribution to the final measurement.

In summary, the final heavy flavor measurement consists of the inclusive muon spectra with the background components subtracted. Figure 4.1 shows an illustrated schematic depicting the inclusive muon yield and its components. The background components are estimated with a Monte Carlo "cocktail" of pions and kaons. These simulated hadrons are thrown based on a model which uses measured spectra at mid-rapidity, and extrapolates them to the higher rapidities of the muon arms. The simulated yields in Gap 3 are normalized to the yields found in the data, and then reweighted to better match the transverse momentum distributions in Gaps 2 and 3, and z-vtx distributions in Gap 4. The Gap 2 and 3 yields are used to make sure the estimate of the punchthroughs is reasonable, while the z-vertex slopes in Gap 4 are used to make sure the decay muon estimate is reasonable. This method of extracting the heavy flavor yield is discussed in further detail in the following sections.

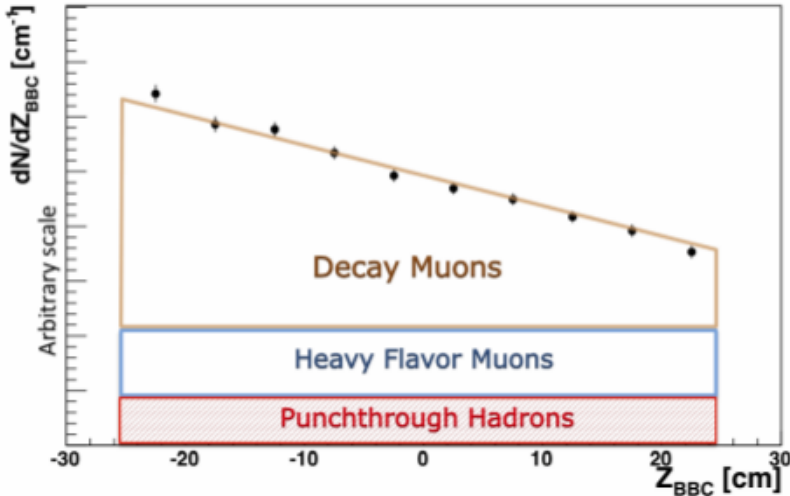


Figure 4.1: Illustrated schematic depicting the different components of the inclusive yield [57].

4.2 Data Quality Assurance

It is important to verify that the data being analyzed is of high quality to ensure a meaningful measurement. Various quality assurance checks are performed in order to determine whether or not data is suitable for analysis. This begins during the data taking process while a run is on-going. Live checks are performed by the data taking team, in particular the data monitor, DAQ operator, and voltage controller. This includes monitoring various detector hit rates, DAQ performance, and voltage levels. However, further QA is performed offline by the analyzers to ensure consistency between the data taken over the course of weeks to months.

In the heavy flavor yield analysis, one of the first things to examine to determine data quality is the number of tracks per event. The initial expectation is that the average number of tracks per event should be constant throughout an entire run (this refers to the entire Run-12). However, this may not always be the case. For the case that the number of tracks per event changes over time, it is necessary to determine the cause of the change and whether or not the quality of the data is compromised. This is the case for this analysis.

Figure 4.2 shows the number of tracks per event versus run number for the entire Run-12 dataset. Of particular interest is the rapid drop around run 375400. The data are fit to a horizontal line before and after run 375400. The fits show that the drop is between 8 and 10

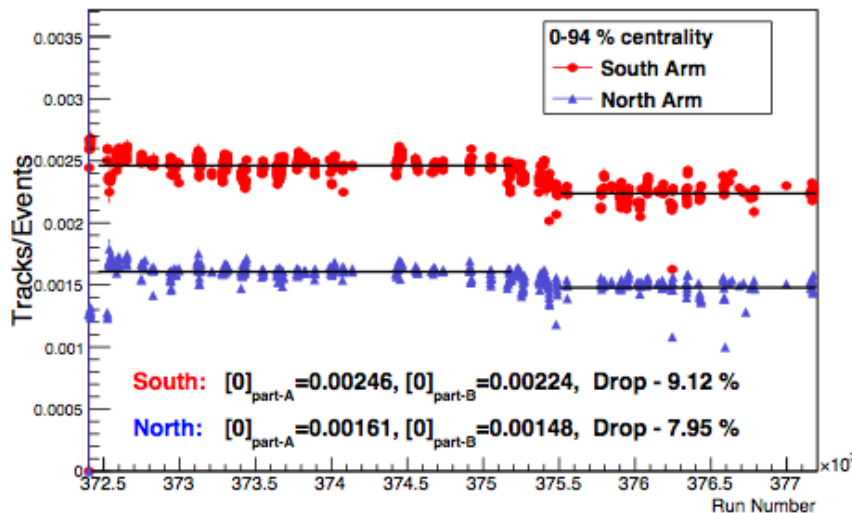


Figure 4.2: Tracks per event versus run number for Run-12.

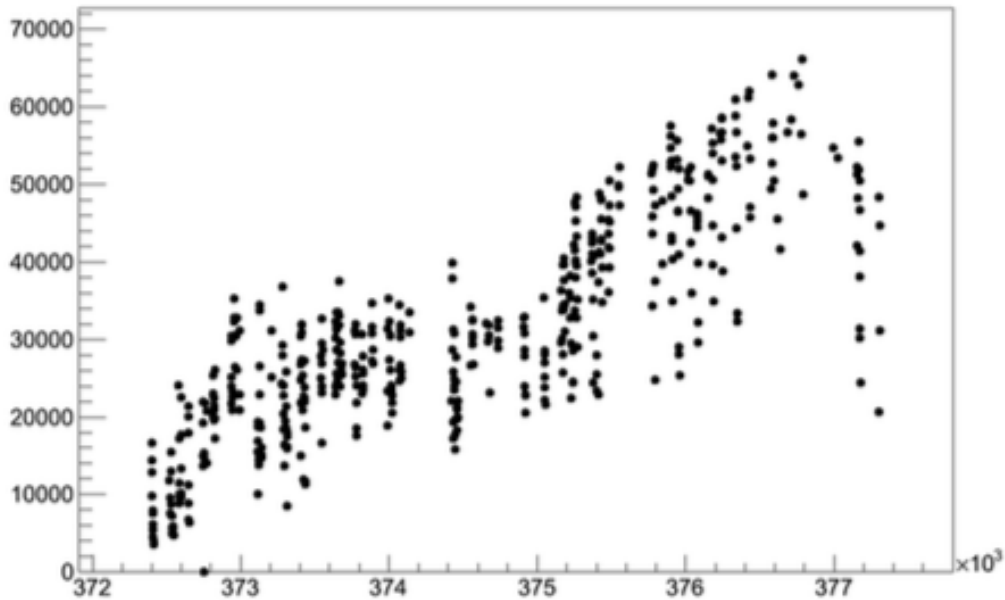


Figure 4.3: Collision rate versus run number for Run-12.

percent. Internal discussions lead to a number of different avenues to explore to diagnose the problem. Ultimately, it was found that the drop in tracks per event was coincident with an increase in beam luminosity and a corresponding drop in MuID efficiency. Figure 4.3 shows the collision rate versus run number for Run-12. One can clearly see a stepped increase in roughly the same place as the tracks per event drop. This will be discussed further in Section 4.6.

Further analysis has shown that the MuID efficiencies have a linear dependence on the collision rate. This will be discussed further in Section 4.5.

4.3 Narrow Vertex Trigger Efficiency Correction

PHENIX implemented a narrow vertex trigger in the Run 12 Cu+Au data-taking period in order to better accomodate the central arm, where events outside of the narrow vertex are more difficult to analyze. The triggered event distribution suffered from a trigger inefficiency which led to centrality dependent z_{vtx} distributions (see Figure 4.4). In order to correct the shifted distributions, the event and track distributions are normalized to the minimum bias

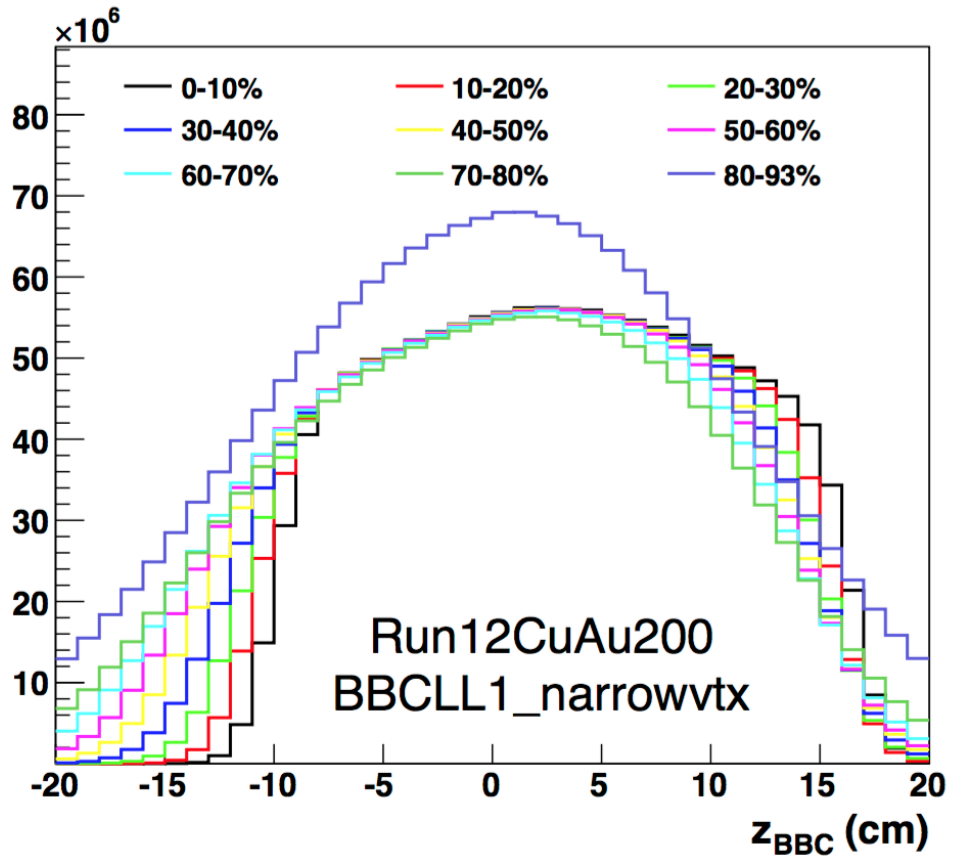


Figure 4.4: Event z_{vtx} distributions for various centralities. The distributions show an increasing shift away from zero for increasingly central collisions [4].

z_{vtx} distributions which do not suffer from the same trigger inefficiency. Figures 4.5 and 4.6 show the corrected (blue) and uncorrected (red) event distributions for the 0-20% and 20-40% centrality bins. The correction has removed the centrality dependence of the z_{vtx} distributions.

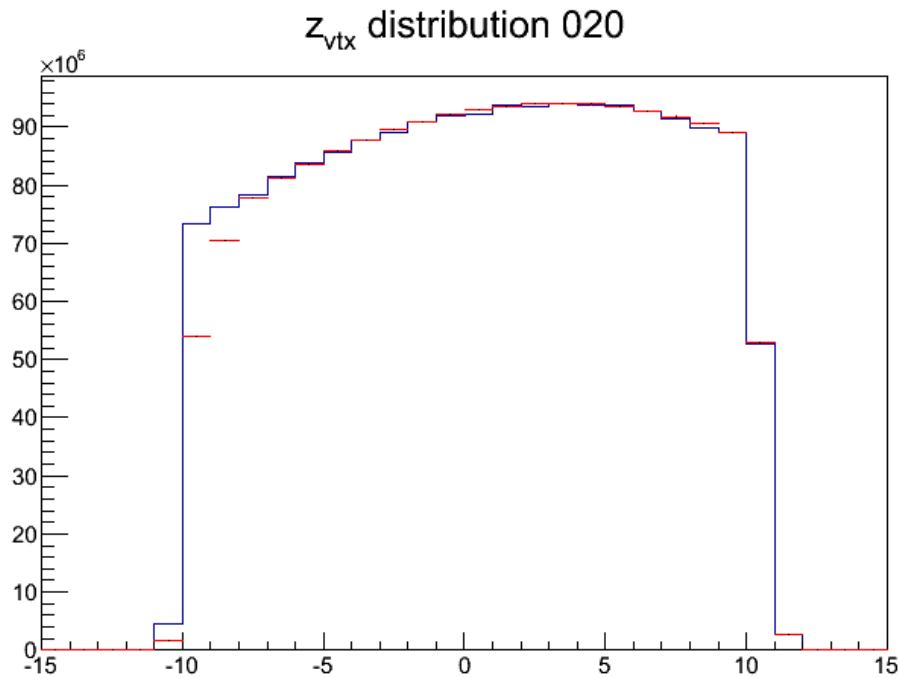


Figure 4.5: Corrected (blue) and uncorrected (red) event z_{vtx} distributions for centrality 0-20%.

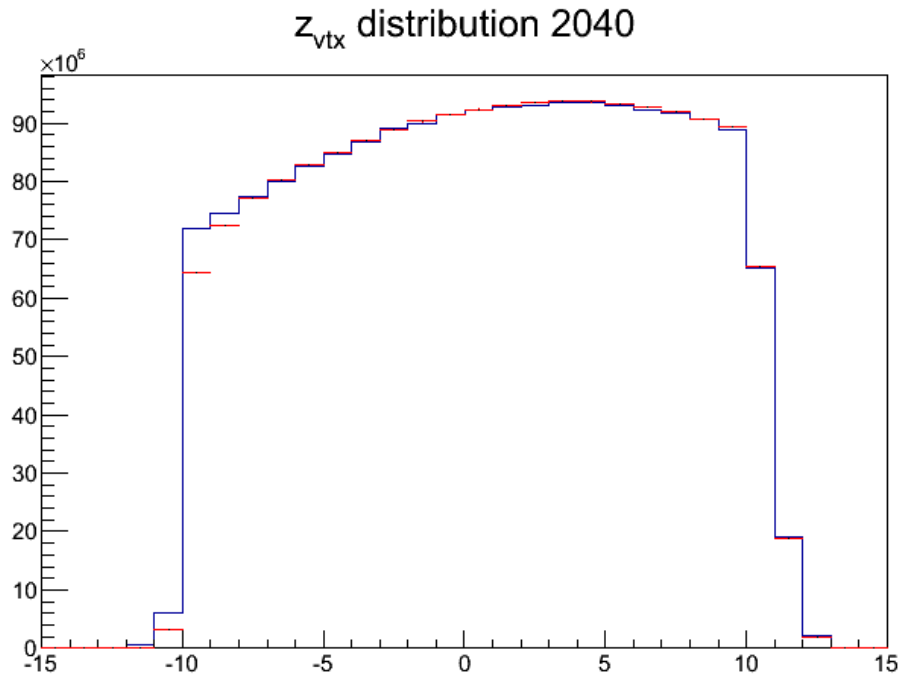


Figure 4.6: Corrected (blue) and uncorrected (red) event z_{vtx} distributions for centrality 20-40%.

4.4 Matching Data and Monte Carlo

Once the data is determined to be of high quality, the next step is to be sure that one understands and interprets the data correctly. In order to make this determination, the detector response is simulated using a Monte Carlo simulation. In fact, the simulation will be used in the background estimate, meaning the level at which the simulation matches the data will become a source of systematic uncertainty in the measurement. The distributions for rapidity, longitudinal momentum, and azimuthal angle are plotted in Figures 4.7, 4.8, and 4.9.

4.5 Track Cuts

While the Muon Arms are designed to identify and track muons that originate from the heavy-ion collision, a number of track cuts are applied offline to ensure the purity of the muon sample while keeping the efficiency high. The analysis presented in this thesis uses the track cuts from PPG 117 [11] as a starting point. The specific values that are required have been changed in some cases, mostly due to the additional absorber material placed in front of the Muon Arms.

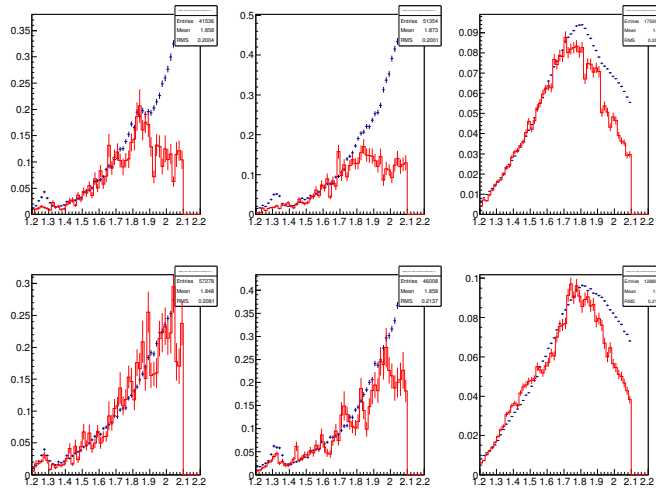


Figure 4.7: Rapidity distributions for Monte Carlo (red) and data (blue). The plots are ordered from left to right by the tracks last gap (2,3,4). The top panels show the south arm and the bottom panels show the north arm.

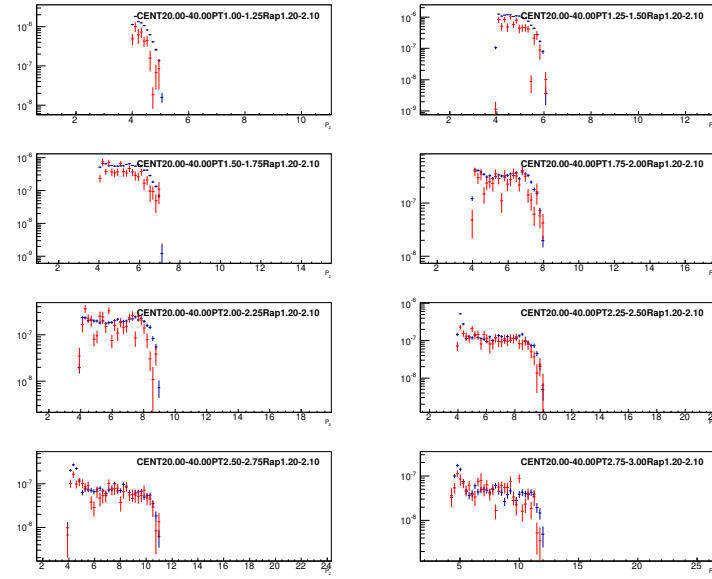


Figure 4.8: p_z distributions for Monte Carlo (red) and data (blue) in ascending ordered p_T bins.

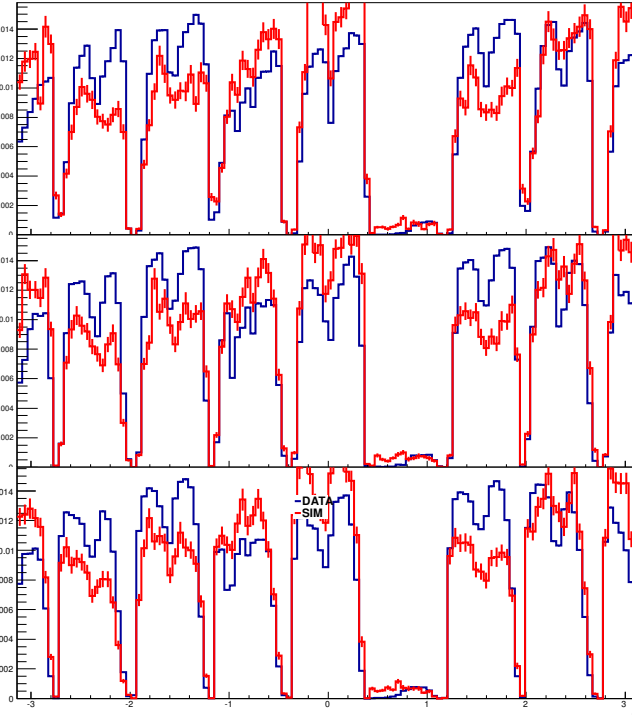


Figure 4.9: Phi distributions for Monte Carlo (red) and data (blue) in the north arm. Note the missing octant. The Monte Carlo shown here was injected with a non-zero v_2 . The red points over estimate the data at $\phi = 0, \pi$ and under estimate the data at $\phi = \pi/2, 3\pi/2$ due to the injected v_2 .

4.5.1 Analysis Variables

- z_{vtx} - The position, along the z-axis, of the event collision. This is measured by the BBC and the FVTX.
- $p\delta\theta$ - $\delta\theta$ refers to the angle of deflection due to the multiple scattering and radiative energy loss within the absorber material, as well as the magnetic field applied [11]. The scattering angle is proportional to $1/p$, therefore $p\delta\theta$ is approximately constant and the $p\delta\theta$ distribution is expected to be Gaussian. The momentum, p , is calculated as: $p = (p_{vtx} + p_{sta1})/2$. $\delta\theta$ is given by:

$$\delta\theta = \cos^{-1}\left(\frac{\vec{p}_{vtx} \cdot \vec{p}_{sta1}}{p_{vtx} \cdot p_{sta1}}\right) \quad (4.1)$$

where \vec{p}_{vtx} is the momentum vector at the collision vertex and \vec{p}_{sta1} is the momentum vector at Station 1 of the MuTr. Figure 4.10 shows an illustration of the $p\delta\theta$ components.

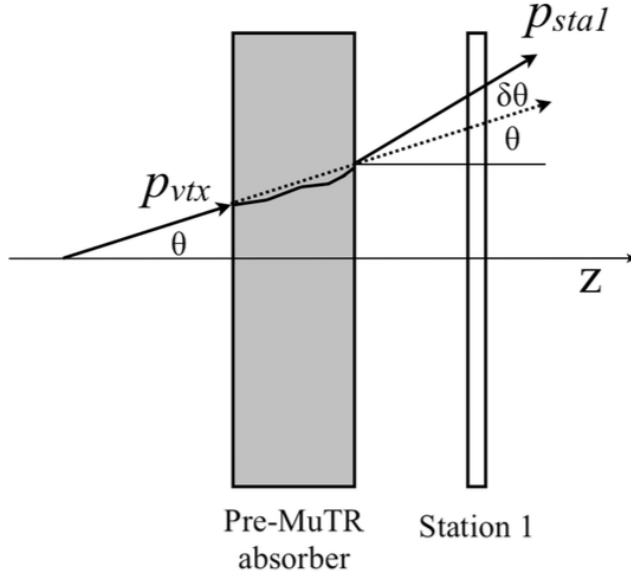


Figure 4.10: Illustration of the $p\delta\theta$ variable [31].

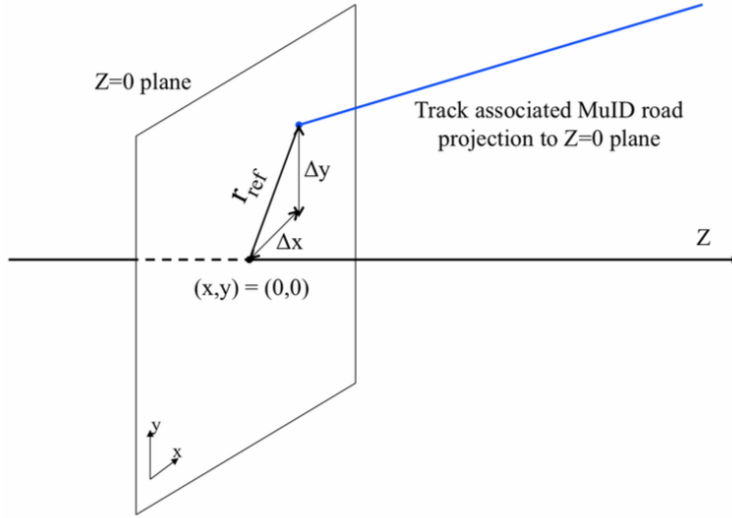


Figure 4.11: Illustration of the r_{ref} variable [11].

- N_{hits}^{MuTr} - The total number of track hits in the MuTr for a given track. There are 3 stations. Stations 1 and 2 have 3 planes each, while Station 3 has 2 planes. Therefore, the total number of possible hits is 16.
- N_{hits}^{MuID} - The total number of track hits in the MuID for a given road. There are 5 gaps, with 2 planes each. Therefore, the total number of possible hits is 10.
- r_{ref} - The radial distance, from the track to the beam axis, of a MuID road at $z = 0$. The road is extrapolated back to $z = 0$ without the use of the MuTr. Figure 4.11 shows an illustration of the r_{ref} variable.
- $DG0$ - “Distance at Gap 0” is the distance, in centimeters, between the MuID road and its associated MuTr track projection at Gap 0. Figure 4.12 shows an illustration of the $DG0$ variable.
- $DDG0$ - The angular difference, in degrees, of the MuID road and its associated MuTr track projection at Gap 0. Figure 4.12 shows an illustration of the $DDG0$ variable.

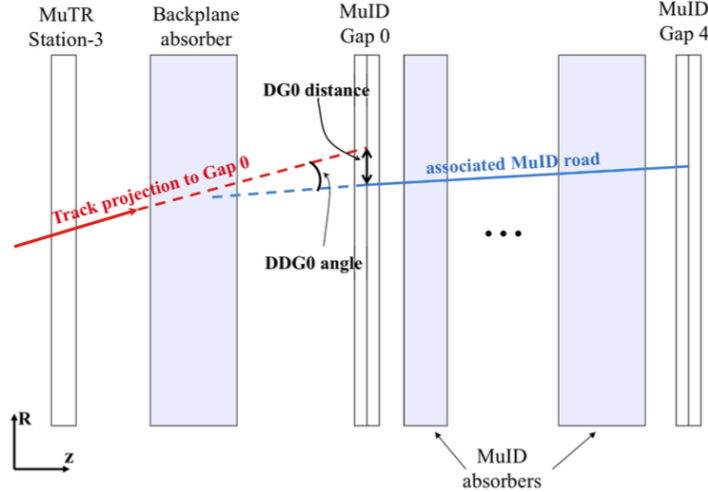


Figure 4.12: Illustration of the $DG0$ and $DDG0$ variables [11].

4.5.2 Analysis Cuts

Cuts are applied to the variables discussed in the previous section on a track by track basis. The values of the cuts are determined via Monte Carlo simulation.

- $|z_{vtx}| < 15$ cm
- $p\delta\theta < 0.35$
- $N_{hits}^{MuTr} > 11$
- $N_{hits}^{MuID}(\text{Gap 2 or Gap 3}) > 5$
- $N_{hits}^{MuID}(\text{Gap 4}) > 6$
- $r_{ref}(\text{South}) < 120$
- $r_{ref}(\text{North}) < 100$
- $DG0(\text{South}) < 20$
- $DG0(\text{North}) < 15$
- $DDG0(\text{South}) < 10$
- $DDG0(\text{North}) < 10$

4.6 Background Subtraction

The background to the heavy flavor single muon measurement consists primarily of light hadrons (mostly pions and kaons) or their decay muons. In some cases, hadrons will decay within the muon tracker, producing a muon with a large fraction of the parent momentum. The decay may create a kink in the track (depending on the decay angle with respect to the direction of the parent particle), leading to an incorrect momentum measurement. In order to estimate and subtract the background, two methods have been developed.

The first method is the use of a so-called “hadron cocktail”. The hadron cocktail refers to a full Monte Carlo simulation using GEANT4. The cocktail consists of simulated pions and kaons (some of which will decay), which are propagated through the PHENIX detector and reconstructed by the PHENIX muon arm tracking algorithm. The detector response is used to estimate the number of stopped hadrons in Gap 4 as well as the number of muons which originate from light hadrons.

The second method, referred to as the “ $p\delta\theta$ ” method, is used to estimate the smaller background contribution of tracks which are misreconstructed at the wrong momentum due to hadron decay within the muon arm. The method takes advantage of the fact that the tracks $p\delta\theta$ distribution is expected to be Gaussian. This analysis uses a hadron cocktail, and addresses the non-Gaussian tail in the $p\delta\theta$ distribution.

4.6.1 Hadron Cocktail

Hadron Cocktail Input

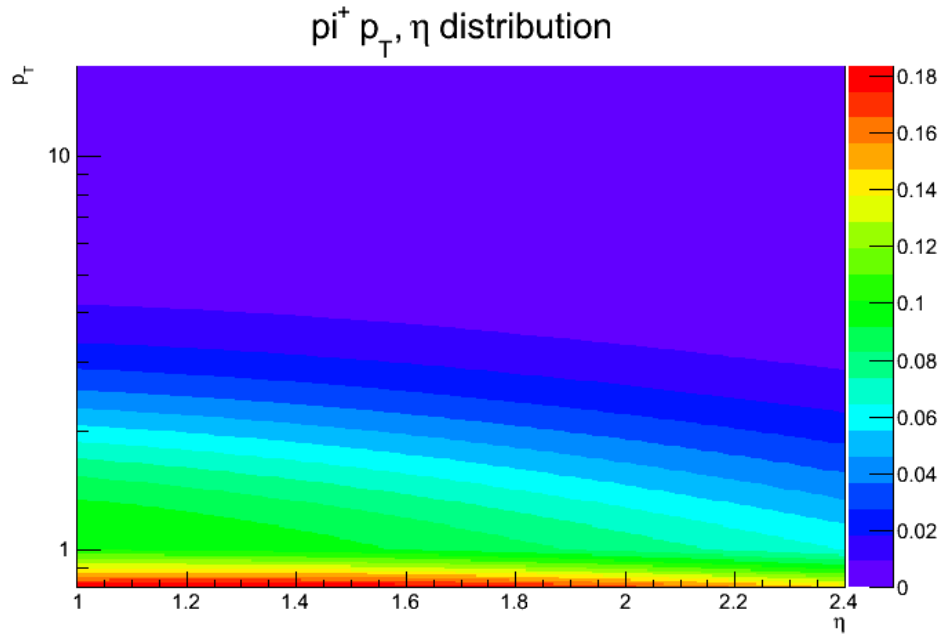


Figure 4.13: Distribution of transverse momentum versus pseudorapidity for π^+ in cocktail input.

Figure 4.13 shows an example of an input distribution for positively charged pions. Simulated positive and negative pions, kaons, and protons are collectively known as the hadron cocktail.

Longitudinal Momentum Cut

In order to purify the sample of hadrons found in the shallow gaps (Gaps 2 and 3), a longitudinal momentum cut is applied. Figure 4.14 shows the longitudinal momentum distribution after a cut at 4 GeV is applied, with the decay muon component plotted in red and the hadron component plotted in blue. Above the cut, the hadron contribution dominates over the decay muon contribution. This is due to the fact that muons have a small interaction cross section relative to the hadrons, and therefore, only low momentum muons are stopped in the shallow gaps.

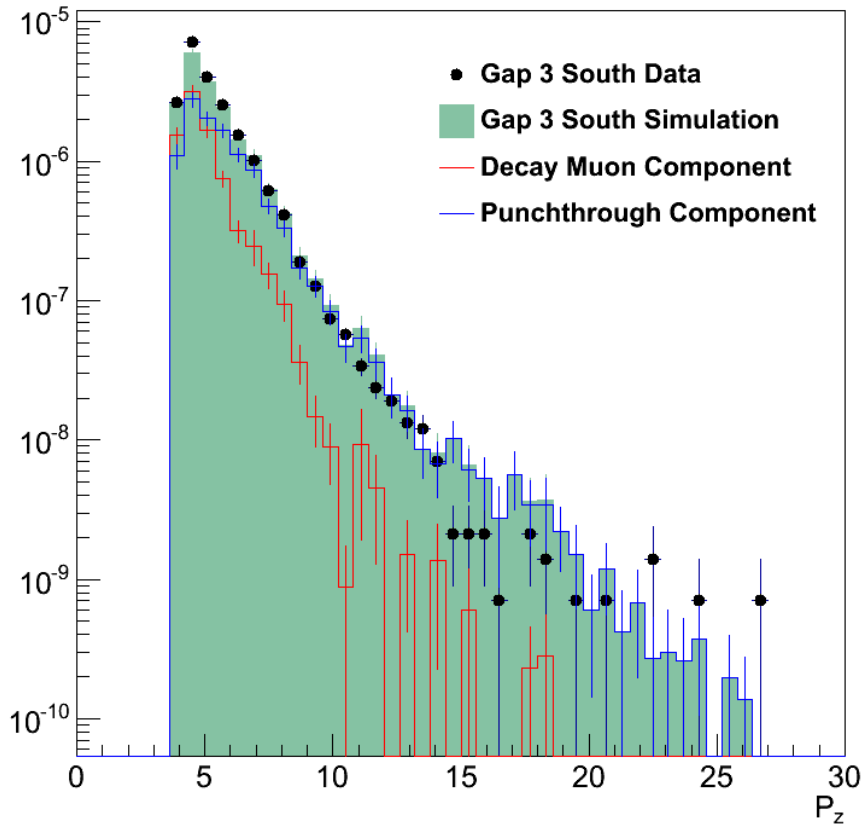


Figure 4.14: Longitudinal momentum distribution, p_Z , for data and simulation in MuID Gap 3 of the south arm.

Embedding

The simulations are performed using GEANT4 [13] to model the PHENIX detector. Single particles are “thrown” at the detector with known momenta and are reconstructed using the muon arm tracking software. In order to properly emulate the effects due to the high occupancy of tracks within the detector, these single particles are “embedded” into real data events at the hit level. The events used for embedding are chosen in a process similar to the QA process described previously. In particular, runs which have a tracks per event near the mean number of tracks per event for the entire data set are chosen.

Tuning the Hadron Cocktail

The first step in the tuning procedure is to normalize the simulated Gap 3 yield to the measured Gap 3 yield in data. This is necessary since the embedding procedure requires that only one simulated track is embedded per event. In real data, however, there may be more than one track per event. Therefore, the simulated yield per event is scaled to match the data. Though it is true that the p_T reweighting procedure would encompass this normalization if it weren't done explicitly, it is still instructive to do the normalization separately in order to better understand the spectra before the reweighting is applied. In this case, the normalization matches the tracks per event while the p_T reweighting corresponds to a reshaping of the spectra. The scale factor is determined as the tracks per event in data divided by the same quantity in simulation:

$$ScaleFactor = \frac{N_{SimEvents}}{N_{DataEvents}} \cdot \frac{\int_{p_T} Yield_{Data}^{Gap3} dp_T}{\int_{p_T} Yield_{Sim}^{Gap3} dp_T}. \quad (4.2)$$

The simulated Gap 3 yield is scaled by this factor. This normalization of the simulated yield does not alter the ratio of punchthrough hadrons to decay muons and does not affect the underlying physics. The upper panel of Figure 4.15 shows the measured Gap 3 yield in solid points as well as the simulated Gap 3 yield (after scaling) in open points. The lower panel shows the data over simulation fraction. Ideally, this fraction should be one. The values of this fraction are used in the calculation of the p_T dependent weights described later.

In order to determine whether the scaled simulation correctly estimates the punchthrough hadron contribution, the scale factor determined in Gap 3 is used to scale the simulated Gap 2 yield. Figure 4.16 is analogous to Figure 4.15. The upper panel shows the measured Gap 2 yield in solid points and the simulated Gap 2 yield (after scaling) in open points. The lower panel shows the data over simulation fraction. As with Gap 3, the fraction should ideally be equal to one and is used in the calculation of the p_T dependent weights.

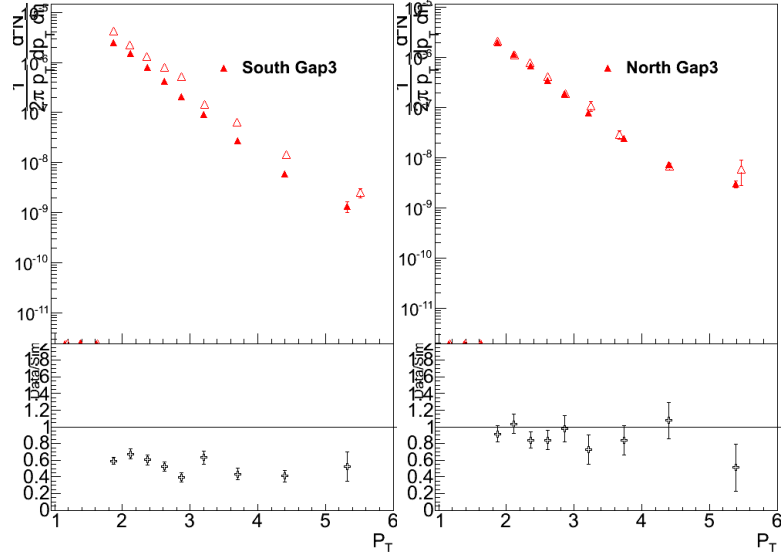


Figure 4.15: Gap 3 yields for Monte Carlo (open) and data (closed) (centrality 20-40 %). The bottom panel shows the data over simulation fraction.

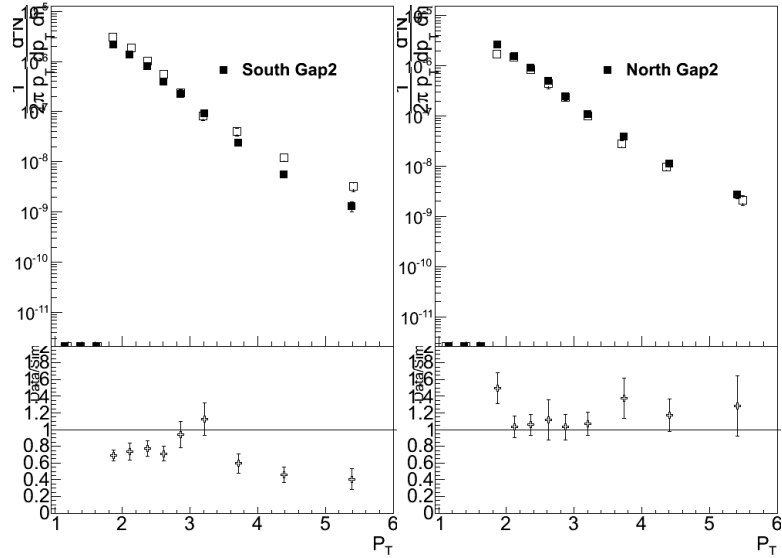


Figure 4.16: Gap 2 yields for Monte Carlo (open) and data (closed) (centrality 20-40 %). The bottom panel shows the data over simulation fraction.

The Gap 4 tracks per event distribution as a function of z-vertex is used to determine whether the cocktail has correctly estimated the decay muon component. The Gap 4 z-vertex distributions are normalized by the scale factor determined in Gap 3. Unlike the Gap 2 and Gap 3 yields, it is not expected that the data and scaled simulation will overlap. The simulation is used to predict the background component while the data includes background as well as the heavy flavor signal. Therefore, after scaling the simulation, it is expected that the Gap 4 z-vertex distribution in data will be larger than in simulation. While the data should exceed the simulation, the slopes of the linear distributions should match since both sets of points have the same dependence on decay muons:

$$\frac{dN_{Data}^{Gap4}/dz}{dN_{Sim}^{Gap4}/dz} \simeq 1. \quad (4.3)$$

Figures 4.17 and 4.18 show the Gap 4 z-vertex distributions for the south and north arms, respectively. Unfortunately, our simulation is not ideal and fractions of data over simulation in Gaps 2 and 3 are not equal to 1, nor are the slopes in Gap 4 exactly equal. This can be attributed to both the uncertainty in the input p_T spectra as well as the uncertainty in the GEANT4 hadron interaction simulation. For this reason, a further tuning of the input p_T spectra is applied. This tuning is effected by using the data over simulation fractions from Gaps 2 and 3, and the slope fraction from Gap 4, $(dN_{Data}^{Gap4}/dz)/(dN_{Sim}^{Gap4}/dz)$, as initial weights for the input p_T spectra.

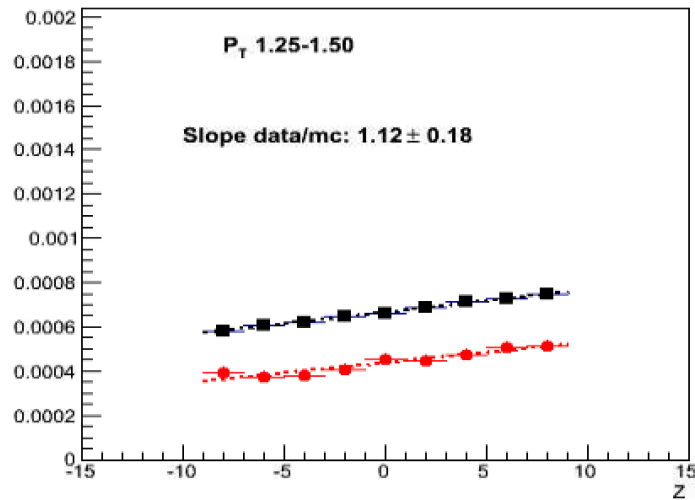


Figure 4.17: Gap 4 south slopes for Monte Carlo (red) and data (black) (centrality 20-40 %).

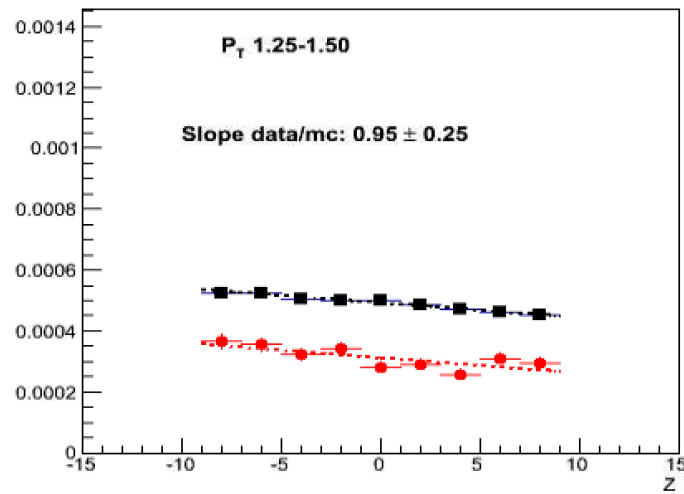


Figure 4.18: Gap 4 north slopes for Monte Carlo (red) and data (black) (centrality 20-40 %).

$$\begin{aligned}
\omega_0^{Gap2}(p_T) &= \frac{N_{Data}^{Gap2}(p_T)}{N_{Sim}^{Gap2}(p_T)} \\
\omega_0^{Gap3}(p_T) &= \frac{N_{Data}^{Gap3}(p_T)}{N_{Sim}^{Gap3}(p_T)} \\
\omega_0^{Gap4}(p_T) &= \frac{dN_{Data}^{Gap4}/dz}{dN_{Sim}^{Gap4}/dz}
\end{aligned} \tag{4.4}$$

An issue that arises from this reweighting scheme is that the input p_T spectra may become discontinuous and, therefore, unphysical. In order to address this the initial weights are convoluted with the p_T -response matrix. The response matrix converts the weights derived from reconstructed tracks into weights for input tracks.

$$\omega(p_T^{Thrown\ i}) = \sum_j^{Reco\ p_T\ bins} \frac{N_{Thrown\ i}^{Reco\ j}(p_T)}{N_{Thrown\ i}(p_T)} \omega_0(p_T) \tag{4.5}$$

The final applied weight is a combination of all the gaps' weights.

$$\omega(p_T) = a\omega^{Gap2}(p_T) + b\omega^{Gap3}(p_T) + c\omega^{Gap4}(p_T) \tag{4.6}$$

The determination of the parameters a , b , and c for the Gap 2, 3, and 4 weights is ambiguous. In the most recent implementation of this method [36], the values 0.25, 0.25, and 0.5, respectively, were chosen. The argument for this choice is that Gaps 2 and 3 are used to match the punchthroughs, while Gap 4 is used to match the decay muons. Therefore, these values correspond to considering decay muons and punchthrough hadrons as equals in the subtraction. However, it is unclear that this is the correct choice for this analysis. In particular, the additional absorber material relative to the previous analysis raises the decay muon to punchthrough ratio. Matters are further complicated by the asymmetric z-vtx distributions, which tend to increase the decay to punchthrough ratio in the south arm relative to the north. In order to address this lack of knowledge, we consider a few different combinations, e.g. 0.25:0.25:0.5, 0.33:0.33:0.33, and 0:0.5:0.5, in order to determine a systematic uncertainty associated with these parameters.

In previous analyses, such as PPG117, a similar scheme was used. However, an important distinction should be made here. PPG117 used an older hadron interaction package,

Table 4.1: Simulation matching criteria.

Gap 4	Gap 3	Gap 2
$\chi^2(p_T)/\text{NDF} < 2$	$\left \frac{N_{Sim}^{Gap3} - N_{Data}^{Gap3}}{N_{Data}^{Gap3}} \right < 0.25$	$\left \frac{N_{Sim}^{Gap2} - N_{Data}^{Gap2}}{N_{Data}^{Gap2}} \right < 0.25$

GEANT3 [13], to propagate the simulated tracks through the detector. Due to the poor matching between simulation and data, the cocktail was tuned yet again. In this additional step, the hadron cross section of GEANT3 was modified such that the cross section used in the simulation ranged from 90% to 110% of the original stated cross section used in either FLUKA or GHEISHA (hadron interaction packages). The simulation was run many times, all with different modified cross sections, and then the different simulations (referred to as packages) were averaged together in order to create a final simulated output that matched the data. The different packages were evaluated using a specific criteria to determine whether a package would be used or thrown out.

The matching criteria addresses the matching of yields in Gaps 2 and 3 as well as the matching of slopes in Gap 4. In order to quantify the matching of slopes in Gap 4, a specialized χ^2/NDF was formulated as such:

$$\chi^2(p_T) = \sum_{i=1}^{z\text{bins}} \frac{(\delta N_i - \delta \bar{N})^2}{\sigma_i^2 + \sigma_{\delta \bar{N}}^2}. \quad (4.7)$$

Here, the sum is over the number of bins in each z-vtx histogram, with each histogram corresponding to a p_T bin. The value δN_i is the difference between data and simulation in the i th bin and $\delta \bar{N}$ is the mean difference between data and simulation for that particular histogram. The value σ_i represents the uncertainty of the difference between data and simulation (δN_i), while $\sigma_{\delta \bar{N}}$ refers to the uncertainty on the mean of the difference ($\delta \bar{N}$). The criteria for a “good” matching is listed in Table 4.1.

4.6.2 Analysis Improvements

One of the most significant differences between this analysis and previous analyses is the addition of the VTX and FVTX detectors as well as the additional absorber material placed between these detectors and the muon arm. The new vertex detectors improve vertex resolution and provide tracking closer to the vertex than ever before. These may be used to improve the tracking in the muon arm. Furthermore, the additional absorber material in front of the muon arms increases the hadron rejection relative to previous analyses.

Increased resolution in measurements of the collision vertex can lead to better tracking in the muon arm. All runs prior to Run-12 primarily used the BBC detector for z-vertex measurements. The BBC is unable to measure the x and y positions of the primary vertex. With the new VTX and FVTX detectors, the collision vertex is measured in 3 dimensions. As discussed in the previous chapter, tracks are projected from the front of the MuTr towards the collision vertex. With the new vertex information, these tracks can be refit while including the vertex in the fitting process. This refitting process gives a better momentum measurement. The refitting also helps with rejecting the combinatorial background of ghost tracks (tracks comprised of uncorrelated hits), which will be discussed in the next subsection.

The increased hadron rejection lowers the background due to punchthrough hadrons, indicated by lower yields in Gap 2 and 3 relative to previous analyses. In previous single muon analyses, only negatively charged muons were considered. This is due to the decreased signal-to-background for positive tracks. There is an abundance of protons relative to anti-protons from the collision which increases the background for positive tracks. Furthermore, positive kaons also increase the background for positive tracks, due to the difference in cross section of K^- and K^+ with the absorber material. This leads to a larger fraction of K^+ reaching the deeper gaps of the MuID [31]. The additional absorber material and the use of GEANT4 allows an accurate prediction of the hadron flux for both positive and negative tracks.

However, there is a larger muon contribution to these yields, particularly in Gap 3. In this case, the heavy flavor contribution to the Gap 3 yields may no longer be negligible. Examining the heavy flavor component in Gap 4 indicates that the heavy flavor to decay

muon ratio is close to 1:5 at $p_T < 3$. This means that scaling the simulation of pions and kaons to the Gap 3 yields in data is not necessarily correct. We do not simulate the heavy flavor hadrons and therefore should expect the simulation to underpredict the data. Furthermore, we expect that the muons that do range out and become Gap 3 tracks will more often have low p_T since it is low total momentum muons that range out. Due to imperfect efficiency in Gap 4, some high momentum muons may end up as Gap 3 tracks if they do not leave a hit in Gap 4. However, efficiency increases with momentum so these are a negligible contribution.

The decay muons constitute $\approx 30\%$ of total simulation at low p_T . Assuming a heavy flavor to decay muon ratio of 1:5, a $\approx 6\%$ increase in tracks is expected at low p_T . This contribution is relatively low. An iterative scheme was discussed, whereby the initial signal is calculated assuming zero heavy flavor muons in Gap 3. Using the signal-to-background from Gap 4, we would then scale to the modified Gap 3 data, in this case $\approx 94\%$ of the Gap 3 yield. The heavy flavor in Gap 4 is then recalculated with this new scale factor. However, this method has not been applied at the current time. Future analysis of this data and/or new data may include this correction.

It is apparent that information that comes from closer to the collision vertex is helpful for this analysis. For this reason, the contributions that the FVTX could provide, aside from vertex measurements, were investigated. The FVTX serves as a vertex detector first and foremost, but it is also able to some tracking as well. Tracks within the Muon Arms can be matched to tracks in the FVTX. Unfortunately, the stipulation that Muon arm tracks must have a match in the FVTX causes a huge reduction in the data, approximately 37 percent in the South arm and 28 percent in the North arm. The statistical hit was too much to bear to make these cuts worthwhile in this analysis; however, better tracking and more data in future runs may allow for such a cut to be beneficial.

4.6.3 $p\delta\theta$ Distributions

The absorber material in front of the Muon arms causes multiple scattering of the particles before they reach the muon arm. As discussed in Section 4.4, the average scattering angle is inversely proportional to the momentum of the particle. Therefore, the product of the

momentum with the scattering angle, $p\delta\theta$, is expected to form a Gaussian distribution rather than a delta function, since the scattering is stochastic process. In PPG117, it was found that for tracks where the projected z vertex disagreed with the measured z vertex, the $p\delta\theta$ distribution was not Gaussian. These tracks include ghost tracks as well as tracks with misreconstructed momentum. In this analysis, the problem has been addressed by taking advantage of the improved vertex measurement and refitting to the vertex, discussed in the previous section. After applying the refitting, the tail found at large values of $p\delta\theta$ has all but disappeared. A loose cut is applied to get rid of the tracks with a large $p\delta\theta$.

4.7 Acceptance and Efficiency Correction

The spectra measured in this analysis must be corrected due to the non-ideal acceptance and efficiency of the detector. A Monte Carlo simulation of muons is used to estimate the acceptance-efficiency correction factor, $A\epsilon$. Much like the hadron cocktail simulation used to estimate the background, the muon simulation involves throwing a realistic muon spectra and propagating them through the detector via GEANT4. The tracks are embedded in events with varying centralities to estimate $A\epsilon$ for the different centrality bins. The correction factor, $A\epsilon$, is then the fraction of fully reconstructed track spectra over the input spectra:

$$A\epsilon(p_T) = \frac{N^{reco}(p_T)}{N^{thrown}(p_T)}. \quad (4.8)$$

Figures 4.19 and 4.20 show the correction factor as a function of p_T for various centrality bins for the south and north arms, respectively. A clear centrality dependence emerges which is expected due to the lowered efficiency of the detector at high multiplicities.

The drop in tracks-per-event over the course of the full Cu+Au run, discussed earlier in the chapter, is also due to the lowered efficiency at high multiplicities. It was observed in Section 4.2 that the drop coincided with a dramatic increase in collision rate. In order to be sure that this effect is understood, $A\epsilon$ is calculated before the drop, part A, and after the drop, part B.

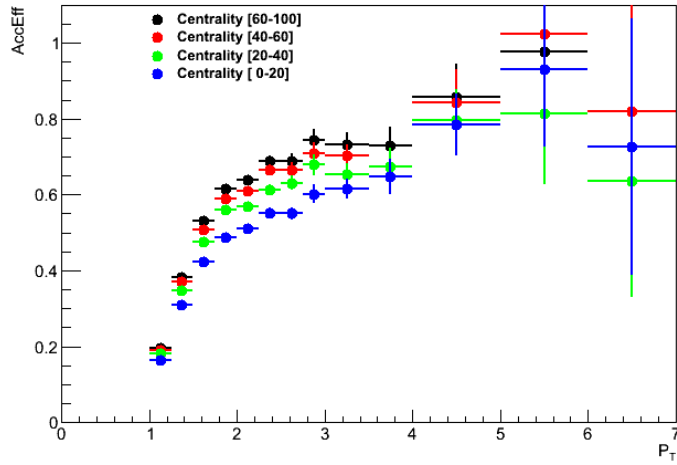


Figure 4.19: Acceptance times efficiency correction in the south arm.

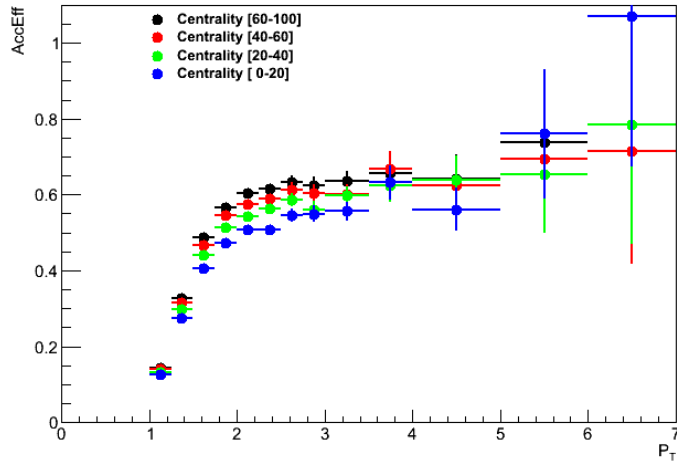


Figure 4.20: Acceptance times efficiency correction in the south arm.

Figures 4.21 and 4.22 show the percent drop in $A\epsilon$ as a function of p_T . The drop in tracks per event is around 8 and 10 percent for the south and north arm, respectively, while the percent drop in $A\epsilon$ is lower. The percent drop also exhibits a p_T dependence. The dependence is also seen in data, with higher p_T tracks showing a larger drop.

Ultimately, the drop in efficiency due to increased luminosity is not sufficient to account for the drop in tracks per event entirely. The remaining discrepancy is treated as a systematic error on the measurement and is not corrected further.

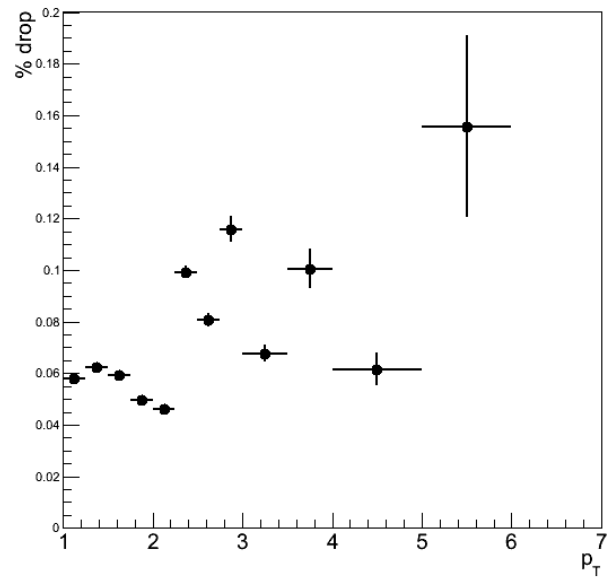


Figure 4.21: Tracks-per-event percent drop in the south arm between part A and part B of the Cu+Au run.

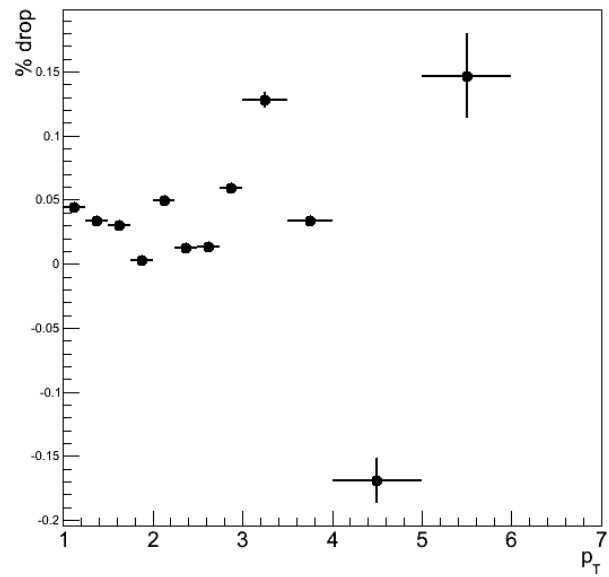


Figure 4.22: Tracks-per-event percent drop in the north arm between part A and part B of the Cu+Au run.

4.8 Heavy Flavor Signal

The heavy flavor signal is extracted by subtracting the final hadron cocktail output from the inclusive Gap 4 yield and applying the acceptance-efficiency correction to the result:

$$\frac{d^2N^{HF}}{2\pi p_T dp_T d\eta} = \frac{1}{2\pi p_T \Delta p_T \Delta\eta} \frac{N^{inc} - N^{cocktail}}{A\epsilon} \quad (4.9)$$

where N^{inc} represents the inclusive Gap 4 spectra, $N^{cocktail}$ represents the final tuned cocktail, and $A\epsilon$ represents the acceptance-efficiency correction. The cocktail is subtracted for each p_T bin. Figure 4.23 shows the heavy flavor single muon yield for the south and north arms.

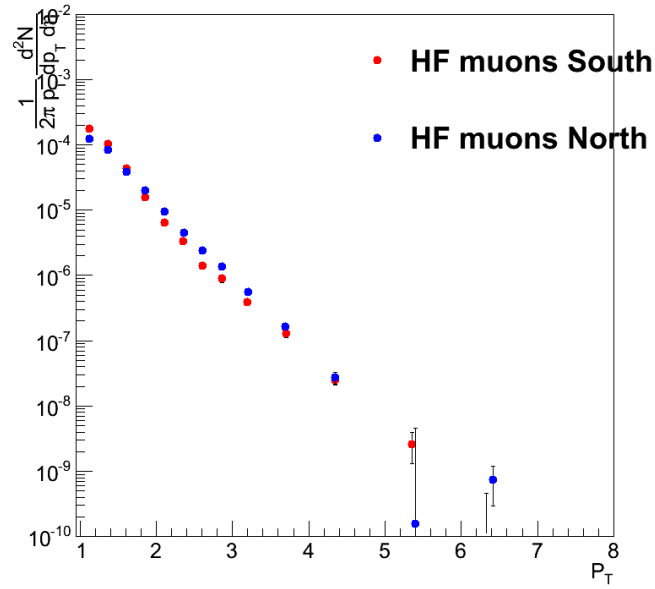


Figure 4.23: Heavy flavor signal, uncorrected for acceptance and efficiency.

Chapter 5

Azimuthal Anisotropy

5.1 Overview

The azimuthal anisotropy coefficients can be measured using various techniques. The measurements presented in this thesis use the “Event Plane Method” [15]. The inclusive v_2 measurement is a weighted sum of the various components’ v_2 :

$$N^{inclusive} v_2^{inclusive} = N^{HF} v_2^{HF} + N^{DM} v_2^{DM} + N^{PT} v_2^{PT} \quad (5.1)$$

where N^{HF} represents the number of heavy flavor single muons within the sample, N^{DM} represents the number of decay muons within the sample, and N^{PT} represents the number of punchthrough hadrons within the sample. These values are determined with the method described in the previous chapter. In order to measure the heavy flavor v_2^{HF} , one must be able to measure or estimate the v_2 of the decay muons and the punchthrough hadrons.

The punchthrough hadrons can be estimated by measuring the v_2 of tracks which stop in Gap 2 or 3 of the MuID. This has been done in previous PHENIX analyses [49]. The decay muons present a more complicated source of background to the v_2 measurement. As discussed in Chapter 1, the azimuthal angle of the decay muons is well correlated with the direction of the parent hadron. However, the muons only carry a fraction of the parent hadron momentum. Therefore, the decay muon v_2 as a function of transverse momentum, p_T , may be shifted towards lower p_T . The magnitude of the shift can be determined using

simulations similar to the ones used in the previous chapter. The downside to this approach is the large systematic error that is introduced. However, it is the only effective method available.

5.2 Event Plane Method

This section is meant to summarize the Event Plane Method of measuring the flow coefficients. The method uses the anisotropic flow of the out-going particles to determine the event plane. Consider the raw azimuthal distribution of the particle yield. Due to the periodicity of the distribution, the particle yield with respect to the lab angle, ϕ , can be expanded in a Fourier series as:

$$\frac{dN}{d\phi} = \frac{x_0}{2\pi} + \frac{1}{\pi} \sum_{n=1}^{\infty} [x_n \cos(n\phi) + y_n \sin(n\phi)]. \quad (5.2)$$

The coefficients x_n and y_n are found in the usual way in Fourier analysis, by multiplying both sides of the equation by $\cos(n\phi)$ or $\sin(n\phi)$ and integrating, and taking advantage of the orthogonality of the cosine and sine terms.

$$\begin{aligned} x_n &= \int_0^{2\pi} \frac{dN}{d\phi} \cos(n\phi) d\phi, \\ y_n &= \int_0^{2\pi} \frac{dN}{d\phi} \sin(n\phi) d\phi \end{aligned} \quad (5.3)$$

For finite multiplicity events, the integrals become sums over the particles:

$$\begin{aligned} x_n &= \sum_{i=1}^N \cos(n\phi_i), \\ y_n &= \sum_{i=1}^N \sin(n\phi_i). \end{aligned} \quad (5.4)$$

The coefficients above are the x and y components of the “Q-vectors” used to reconstruct the event plane, and N is the number of tracks being summed over. From this construction, it is clear that the measured event plane corresponds to the average angle of emission of tracks. The event plane is given by:

$$\begin{aligned}
x_n &= Q_n \cos(n\Psi_n), \\
y_n &= Q_n \sin(n\Psi_n), \\
n\Psi_n &= \tan^{-1}\left(\frac{y_n}{x_n}\right).
\end{aligned} \tag{5.5}$$

With the estimated event plane in hand, now consider the azimuthal distribution with respect to this event plane, Ψ_n . In the same way as before, this distribution can be expanded in a Fourier series.

$$\frac{dN}{d(\phi - \Psi_n)} = \frac{a_0}{2\pi} + \frac{1}{\pi} \sum_{k=1}^{\infty} [a_{kn} \cos(kn(\phi - \Psi_n)) + b_{kn} \sin(kn(\phi - \Psi_n))] \tag{5.6}$$

with

$$\begin{aligned}
a_{kn} &= \int_0^{2\pi} \frac{dN}{d(\phi - \Psi_n)} \cos(kn(\phi - \Psi_n)) d(\phi - \Psi_n) = \sum_{i=1}^N \cos(kn(\phi_i - \Psi_n)), \\
b_{kn} &= \int_0^{2\pi} \frac{dN}{d(\phi - \Psi_n)} \sin(kn(\phi - \Psi_n)) d(\phi - \Psi_n) = \sum_{i=1}^N \sin(kn(\phi_i - \Psi_n)).
\end{aligned} \tag{5.7}$$

Here, the particle distribution is evaluated with respect to the measured event planes, Ψ_n , rather than the true reaction plane, Ψ_r . The relationship between Ψ_r and Ψ_n depends on the physics of the expanding medium. For example, Ψ_2 can take values of Ψ_r or $\Psi_r + \Pi/2$. $\Psi_2 = \Psi_r$ indicates that the major axis of the ellipse in momentum space lies within the reaction plane, while $\Psi_2 = \Psi_r + \Pi/2$ indicates that the major axis of the ellipse is perpendicular to the reaction plane. The latter situation is known as “squeeze-out flow” [55].

The Fourier coefficients can be evaluated with an event plane such that the harmonic of the event plane is less than or equal to the harmonic of the coefficient being evaluated and is a divisor of the harmonic of the coefficient being evaluated. For example, Ψ_2 can be used to evaluate v_2 , v_4 , etc. Ψ_3 can be used to evaluate v_3 , v_6 , etc. The sum over k in equation 5.6 ensures that the correct terms are present in the expansion.

When $n = 0$, we get $a_0 = N$. Then factoring the $\frac{N}{2\pi}$ out of both terms in the Fourier expansion above we get:

$$\frac{dN}{d(\phi - \Psi_n)} = \frac{N}{2\pi} [1 + \sum_{k=1}^{\infty} \left[\frac{2a_{kn}}{N} \cos(kn(\phi - \Psi_n)) + \frac{2b_{kn}}{N} \sin(kn(\phi - \Psi_n)) \right]] \quad (5.8)$$

and

$$\begin{aligned} \frac{a_{kn}}{N} &= \frac{\sum_{i=1}^N \cos(kn(\phi_i - \Psi_n))}{N} = \langle \cos(kn(\phi - \Psi_n)) \rangle, \\ \frac{b_{kn}}{N} &= \frac{\sum_{i=1}^N \sin(kn(\phi_i - \Psi_n))}{N} = \langle \sin(kn(\phi - \Psi_n)) \rangle. \end{aligned} \quad (5.9)$$

The collision geometry will be symmetric with respect to the true reaction plane, defined by the impact parameter and the beam axis. If the measured event plane, defined as the average angle of emission of the tracks, is a good approximation of the true reaction plane then the average sine term will be zero within some statistical deviations due to reflection symmetry [15]. The average cosine terms are the flow coefficients, $v_n = \langle \cos(n(\phi - \Psi_n)) \rangle$. If the anisotropy in the particle yield at low p_T is not due to the collective expansion of the fireball, then the average angle of emission of tracks will not necessarily coincide with the true reaction plane, and the cosine terms will be small. If we assume that the sine terms are zero, then the equation reduces to:

$$\begin{aligned} \frac{dN}{d(\phi - \Psi_n)} &= \frac{N}{2\pi} [1 + \sum_{k=1}^{\infty} [2v_{kn} \cos(kn(\phi - \Psi_n))]], \\ v_{kn} &= \langle \cos(kn(\phi - \Psi_n)) \rangle. \end{aligned} \quad (5.10)$$

One may also measure the flow coefficients by examining particle correlations in ϕ . This method is not described here. The low multiplicity of tracks in the muon arms does not allow for a statistically meaningful measurement with this method [17].

In order to measure the particle distribution with respect to the true reaction plane, Ψ_r , the event plane resolution must be taken into account, such that

$$v_n^{true} = \frac{v_n^{observed}}{\langle \cos(n(\Psi_n - \Psi_r)) \rangle}. \quad (5.11)$$

This is because the event plane measurements are hindered by the finite multiplicity of particles within an event. Equation 5.11 is derived as follows:

$$\begin{aligned}
v_2^{raw} &= \langle \cos(2(\phi - \Psi^{meas})) \rangle, \\
&= \langle \cos(2(\phi - \Psi^{meas} + \Psi^{true} - \Psi^{true})) \rangle, \\
&= \langle \cos(2(\phi - \Psi^{true} + d\Psi)) \rangle, \\
&= \langle \cos(2(\phi - \Psi^{true})) \cos(2(d\Psi)) - \sin(2(\phi - \Psi^{true})) \sin(2(d\Psi)) \rangle, \\
&= \langle \cos(2(\phi - \Psi^{true})) \cos(2(d\Psi)) \rangle, \\
&= v_2^{true} Res(\Psi).
\end{aligned} \tag{5.12}$$

The resolution is found by comparing the correlations of different event plane detectors. For the case that the different detectors have different acceptance, and therefore different multiplicity, as well as the case that the detectors may have different resolution, one needs three different detectors to determine the resolution [15]. The resolution is calculated for detectors a , b , and c as:

$$\langle \cos(n(\Psi_m^a - \Psi^{true})) \rangle = \sqrt{\frac{\langle \cos(n(\Psi_m^a - \Psi_m^b)) \rangle \langle \cos(n(\Psi_m^a - \Psi_m^c)) \rangle}{\langle \cos(n(\Psi_m^b - \Psi_m^c)) \rangle}}. \tag{5.13}$$

5.3 Data Quality Assurance

The data used in the azimuthal anisotropy measurement is subject to the same high standards discussed in the previous chapter. One of the key differences of the anisotropy measurement is the use of the FVTX detector for event plane measurements. Run-12 marked the inaugural run for the FVTX detector. As such, it was subject to some issues which made some of the data unsuitable for analysis. This section outlines the QA checks done on the FVTX data to ensure a meaningful measurement.

In heavy-ion collisions, the event plane distribution is expected to be isotropic. However, the FVTX detector displayed a large number of dead areas during the run; this led to an anisotropic detector acceptance. Furthermore, the dead areas of the detector were not consistent throughout the run, though a trend can be seen in the data. Figures 5.1 and 5.2

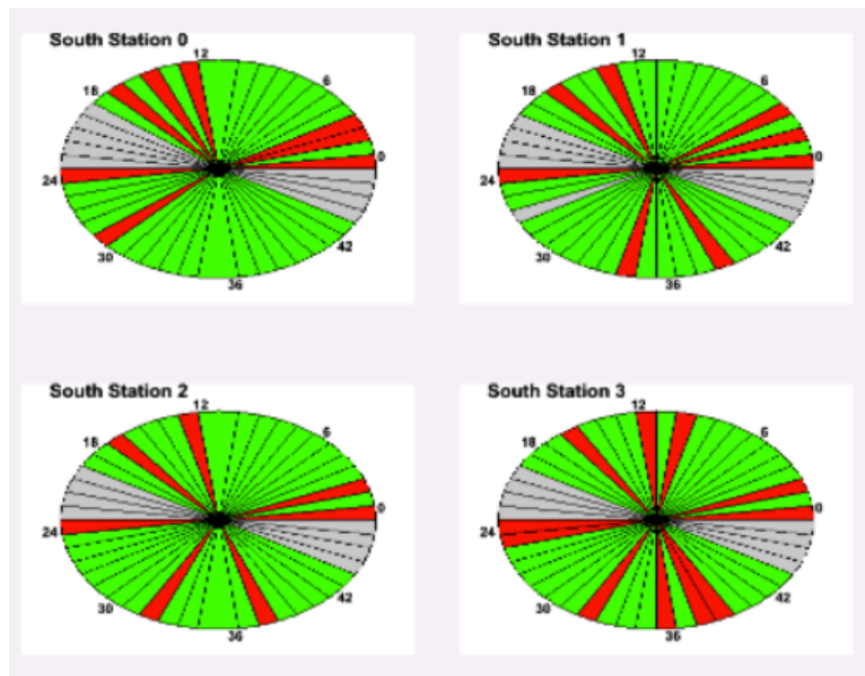


Figure 5.1: FVTX south dead map for run 373139.

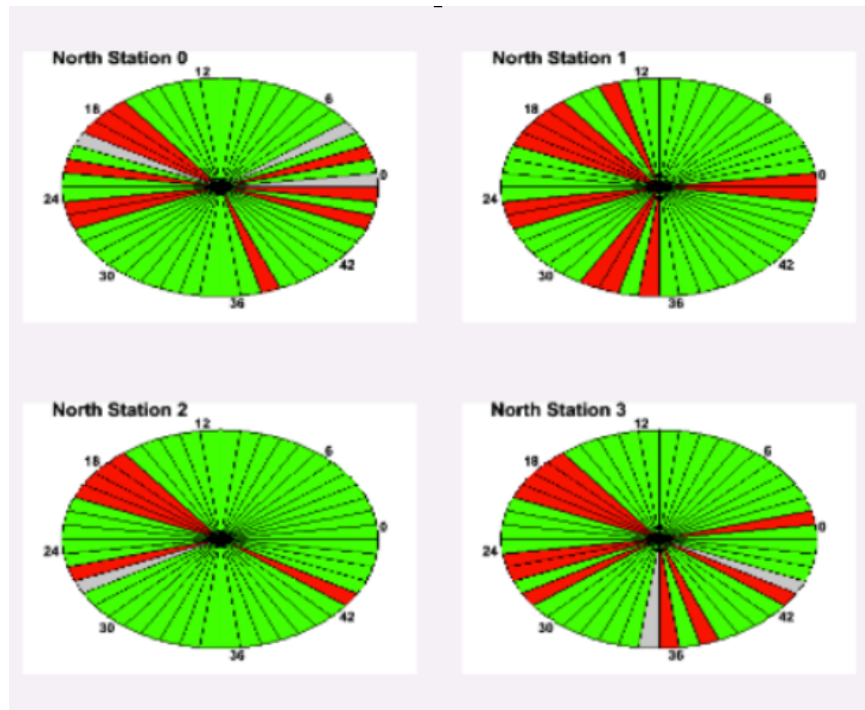


Figure 5.2: FVTX north dead map for run 373139.

show examples of dead maps of each station within the FVTX, south and north respectively, for a run. The green slices represent live detector area with nominal hit rates. The red slices represent detector area with hit rates which are too high or too low. The grey area represents detector area which is disabled.

Due to the dead areas in the detector, the measured event plane distribution is not isotropic. However, this can be addressed by applying a flattening procedure. In this procedure, the event planes are shifted by a correction factor determined by Equation 5.14. [15]:

$$n\Delta\Psi_n = \sum_{k=1}^{k_{max}} [- \langle \sin(kn\Psi_n) \rangle \cos(kn\Psi_n) + \langle \cos(kn\Psi_n) \rangle \sin(kn\Psi_n)]. \quad (5.14)$$

Here, the averages refer to the average over the entire distribution. The value k_{max} is generally taken to be $4/n$ [15] in these shifts. After this shift is applied, the resulting event plane distributions are expected to be flat. Figure 5.3 shows the raw versus calibrated event plane distributions for a run segment.

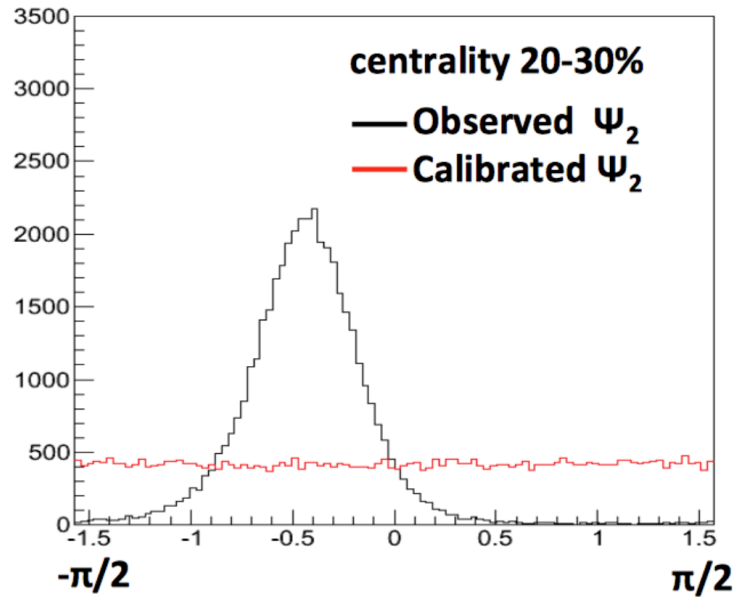


Figure 5.3: FVTX raw versus calibrated event plane distributions for run 373139, segment 5 [43].

After the event planes have been flattened, further checks are applied to ensure the distributions are indeed isotropic. If they are isotropic, then the average cosine and sine of the event plane distributions, $\cos(n\Psi_n)$ and $\sin(n\Psi_n)$, should be zero. A non-zero value indicates that the detector had enough dead area so as to skew the distribution. While the above method is a good first attempt at determining this, another method is applied which inspects the distribution in finer detail.

The procedure is repeated run by run in order to determine a good run list for the analysis using the following method. The cosine and sine average terms are determined for every 5000 events in a run. These are then plotted such that the y-axis is the average cosine or sine, and each bin on the x-axis represents 5000 events. The values should be close to zero within some statistical fluctuations. Figure 5.4 shows an example of a good run on the left and an example of a bad run on the right.

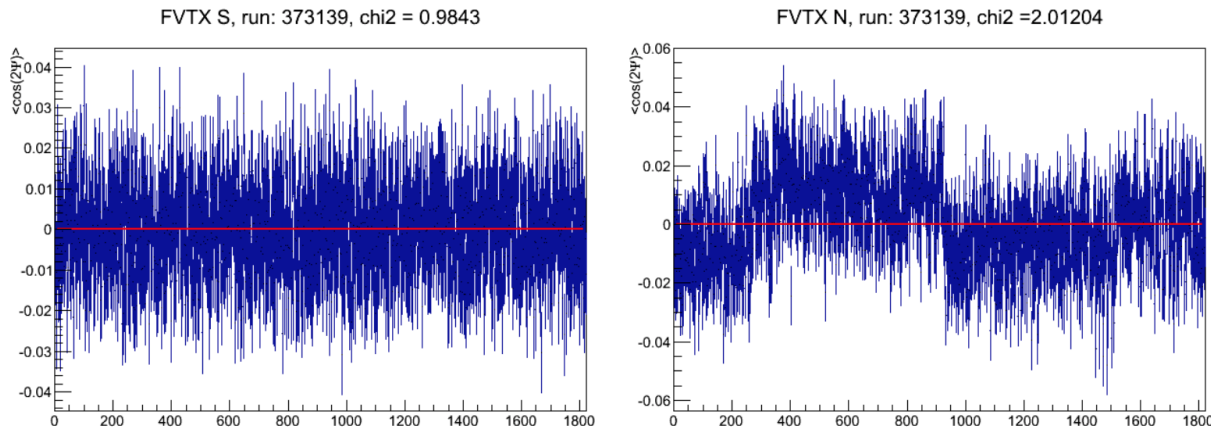


Figure 5.4: FVTX event plane QA plot for a good run (left) and a bad run (right).

The resulting distribution is fit to a horizontal line at $y = 0$ and the χ^2/NDF is determined. These χ^2/NDF are plotted against run number, as shown in Figure 5.5. These χ^2/NDF versus run number plots are then projected on to the y-axis to show the χ^2/NDF distribution, which ideally would be Gaussian distributions centered at 1. These projections are shown in Figures 5.6 and 5.7. Finally, based on these χ^2/NDF distributions, a cut is applied on χ^2/NDF which determines the good run list. Based on these distributions, a cut of $0.85 < \chi^2/NDF < 1.15$ ($0.85 < \chi^2/NDF < 1.6$) is applied in the south (north) arm.

It is clear from these plots that the FVTX South performed more accurately than did the FVTX North. Investigation of many of the dead maps from different runs indicates that the FVTX North had much more dead area than did the FVTX South for most of Run-12. The extent to which the performance of the event plane measurement affected the final v_2 measurement is addressed in the systematic error.

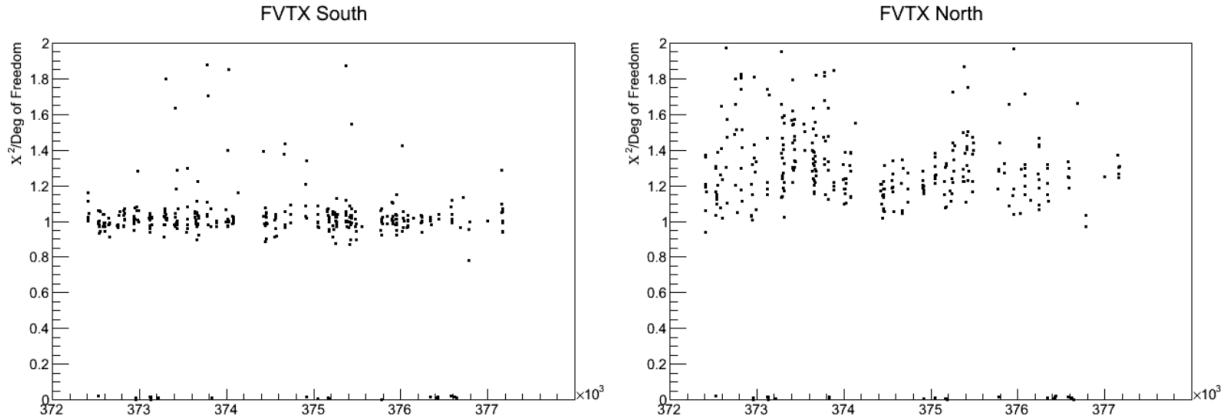


Figure 5.5: χ^2/NDF versus run number for FVTX South (left) and FVTX North (right).

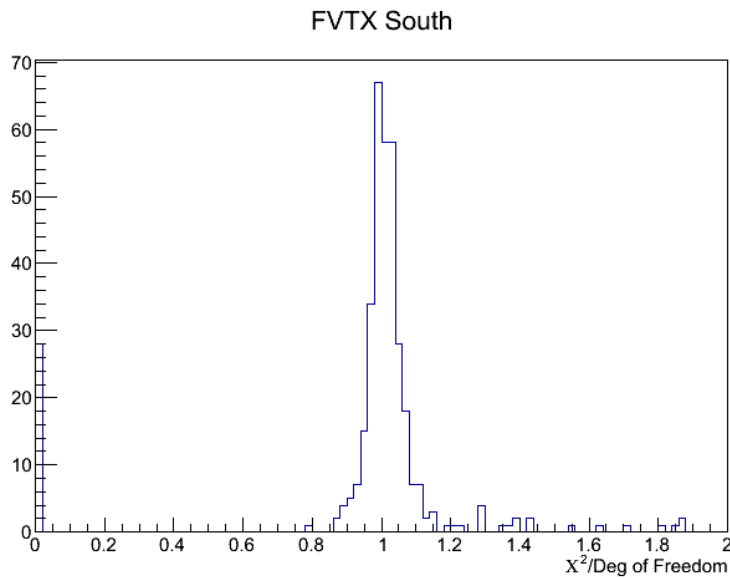


Figure 5.6: χ^2/NDF distributions for FVTX South.

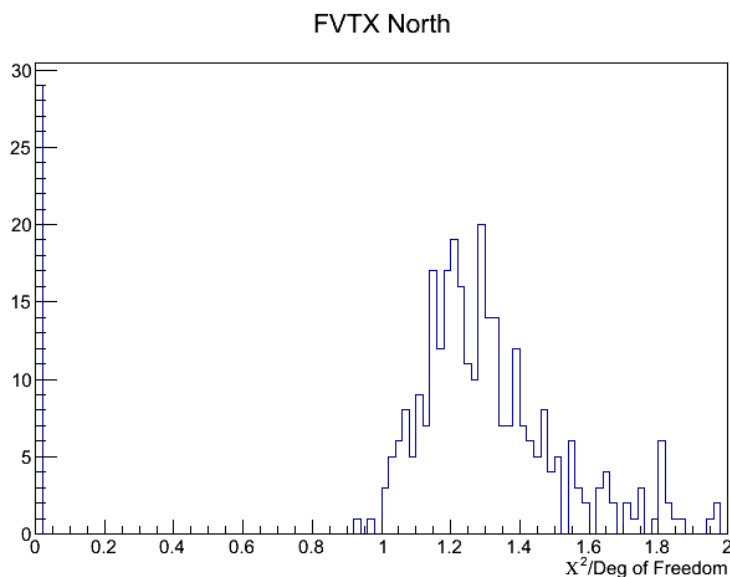


Figure 5.7: χ^2/NDF distributions for FVTX North.

5.4 Fitting Azimuthal Distributions

The anisotropy coefficients are determined from fits to distributions of ϕ with respect to the event plane for each p_T bin. Equation 5.10 is used for the fit, where all the coefficients, $v_{n \neq 2}$, are set to zero and v_2 is a free parameter. The fit determines the value, and the error on the fit is the statistical error.

Figures 5.8 and 5.9 show an example of these fits.

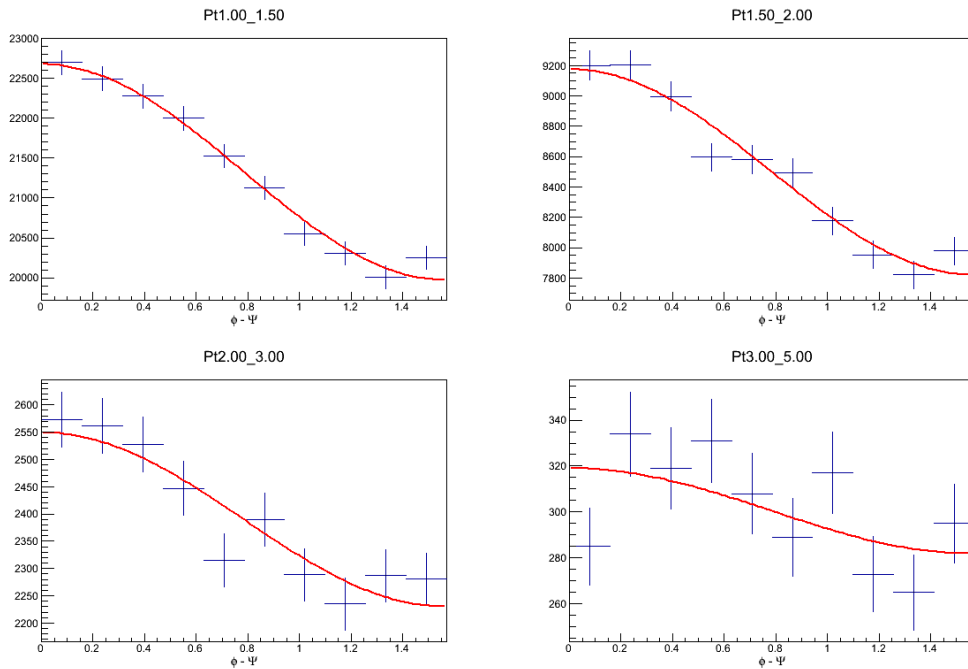


Figure 5.8: $\phi - \Psi$ fits for different p_T bins, Gap 4 North, EP: FVTX S, centrality 10%–15%.

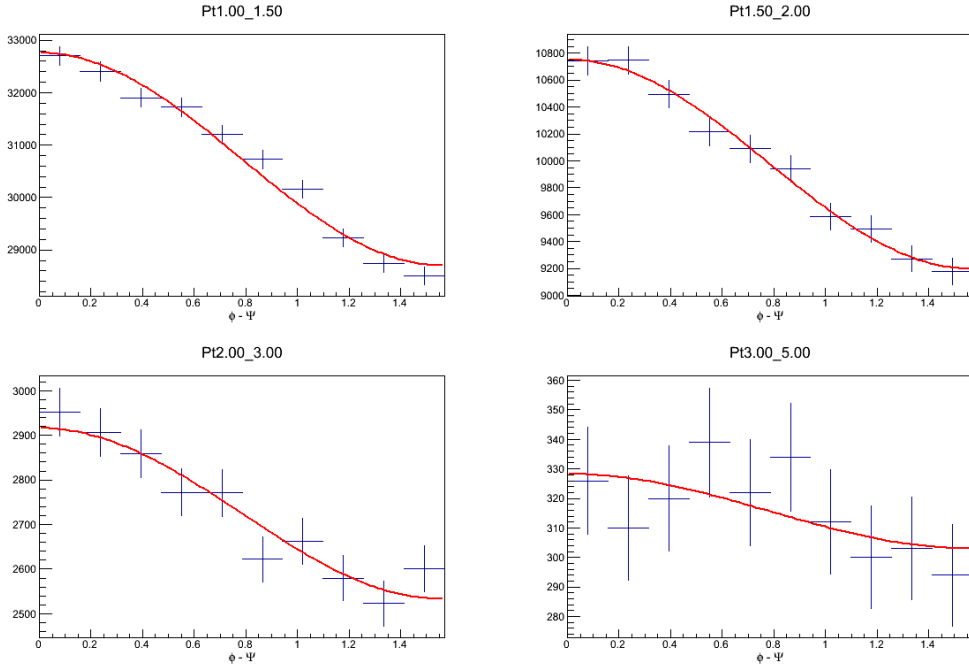


Figure 5.9: $\phi - \Psi$ fits for different pT bins, Gap 4 South, EP: FVTX N, centrality 10%–15%.

5.5 Hadron Flow

In order to estimate the background component of the inclusive v_2 , one must first estimate or measure the v_2 for hadrons. The background is exactly the same as in the heavy flavor yield analysis. That is, there is some combination of decay muons and punchthrough hadrons. This analysis measures the hadron v_2 in the shallow gaps in order to estimate the decay muon v_2 in Gap 4, the dominant source of background. Figures 5.10 and 5.11 shows the v_2 for stopped tracks in Gaps 2 and 3.

Gap 2 and Gap 3 tracks v2 South, Cent 20-40, $|BBC\ Z|<10$

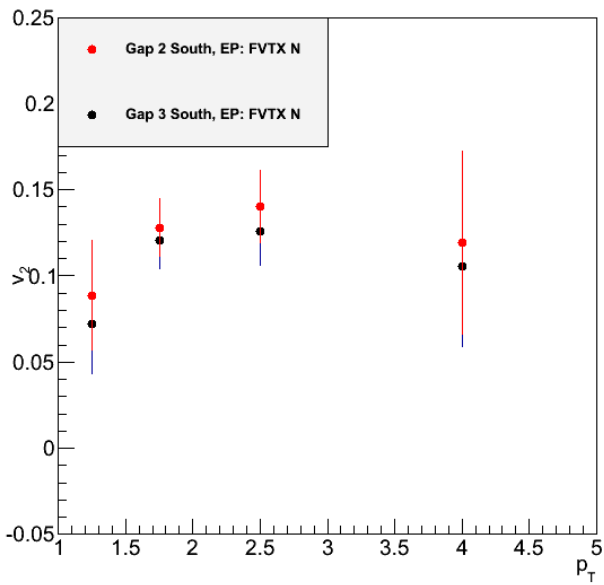


Figure 5.10: Momentum distribution of v_2 for Gap 2 and Gap 3 tracks, South Arm.

Gap 2 and Gap 3 tracks v2, Cent 20-40, $|BBC\ Z|<10$

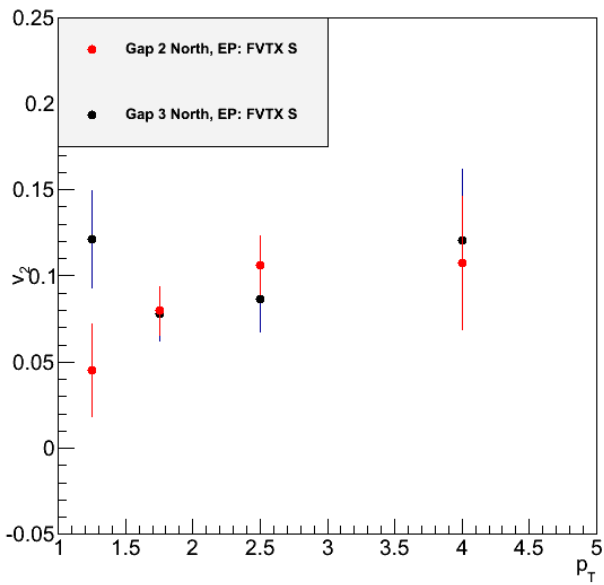


Figure 5.11: Momentum distribution of v_2 for Gap 2 and Gap 3 tracks, North Arm.

5.6 Background Subtraction

The inclusive v_2 measured in the muon arms is a weighted sum of the constituent components' v_2 . The major contributions come from the punchthrough hadrons, decay muons, and the heavy flavor signal. In order to separate out the contributions, the ratios of the various components are needed. This determines the weights, N , used in Equation 5.1. These are determined in the heavy flavor yield analysis, outlined in the previous chapter. In addition, the v_2 for each of the background components is required. Therefore, the anisotropy analysis requires measurement or estimation of the v_2 for the punchthrough hadrons as well as the decay muons. As discussed in the previous chapter, Gaps 2, 3, and 4 contain differing ratios of punchthrough hadrons, decay muons, and heavy flavor signal. Gap 2 contains mostly punchthrough hadrons after the previously described cut on longitudinal momentum is applied, while Gap 3 contains a significant amount of both punchthrough hadrons as well as decay muons.

In the rest frame of a given parent hadron, the decay angle distribution of the daughter muon is isotropic. In the lab frame, the rest frame is Lorentz boosted due to the large momentum of the parent hadron. Therefore, the decay angle distribution in the lab frame is heavily skewed towards the direction of propagation of the parent hadron. In the lab frame the muon continues on in the direction of the parent hadron, meaning the azimuthal anisotropy is approximately preserved. However, the muon only receives a fraction of the parent hadron momentum. In this case, the v_2 as a function of p_T will be shifted towards lower p_T . In order to estimate the shift, a Monte Carlo simulation of hadron decay is used.

The simulation is used to determine to what extent the decay muon v_2 matches the punchthrough v_2 . For the case that the shift between the two is small, we may consider the punchthrough v_2 a proxy for decay muon v_2 with some associated systematic error. In this case, Equation 5.1 becomes:

$$N^{inclusive} v_2^{inclusive} = N^{HF} v_2^{HF} + N^{BG} v_2^{BG} \quad (5.15)$$

Figures 5.12 and 5.13 show the simulated punchthrough and decay muon v_2 as a function of p_T .

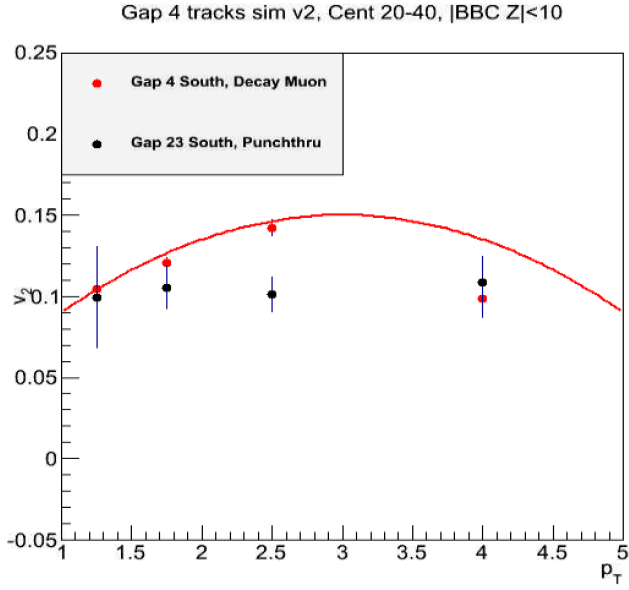


Figure 5.12: Momentum distribution of v_2 for Decay Muons and Punchthrough Tracks in Gap 2 and Gap 3, South Arm centrality 20%–40%.

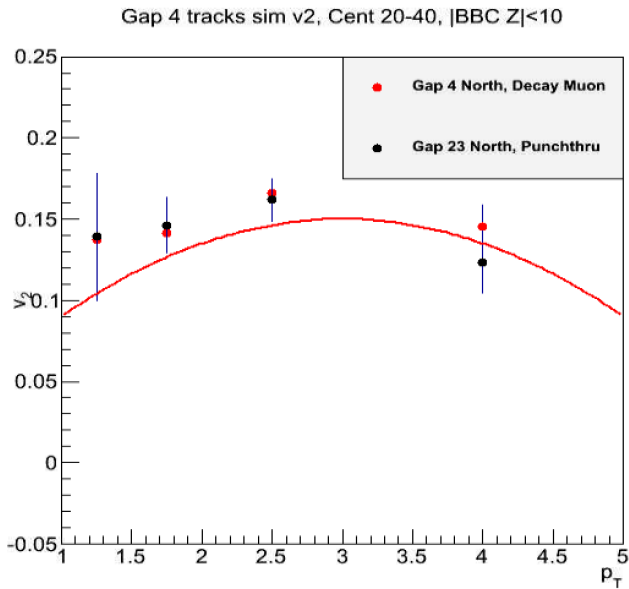


Figure 5.13: Momentum distribution of v_2 for Decay Muons and Punchthrough Tracks in Gap 2 and Gap 3, North Arm centrality 20%–40%.

In order to test the validity of the simulation, the v_2 of the reconstructed tracks is compared to the v_2 of the input. Figure 5.14 shows the v_2 for the input distribution of tracks and the v_2 for the reconstructed tracks in Gap 4.

The measured v_2 in Gaps 2 and 3 serve as the background component of the inclusive v_2 . The signal-to-background ratio determined in the previous chapter allows us to extract the heavy flavor v_2 signal.

5.7 Heavy Flavor Flow

The final heavy flavor measurement is given by:

$$v_n^{HF} = \left(1 + \frac{1}{S/B}\right)v_n^{inc} - \frac{1}{S/B}v_n^{BG} \quad (5.16)$$

where S/B is the signal-to-background ratio from the previous chapter.

Figure 5.15 shows the inclusive Gap 4 v_2 measurement with the combined Gap 2+3 v_2 measurement. Figure 5.16 shows the heavy flavor single muon v_2 . An overview of the systematic error (represented by the colored bands) analysis is presented in the next section.

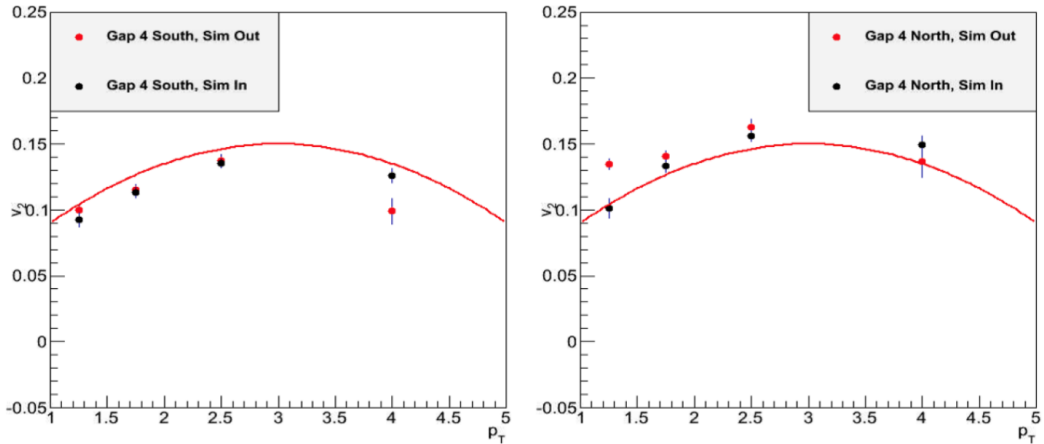


Figure 5.14: Momentum distribution of v_2 for input and reconstructed distributions of tracks, South Arm (left) and North Arm (right) centrality 20%–40%.

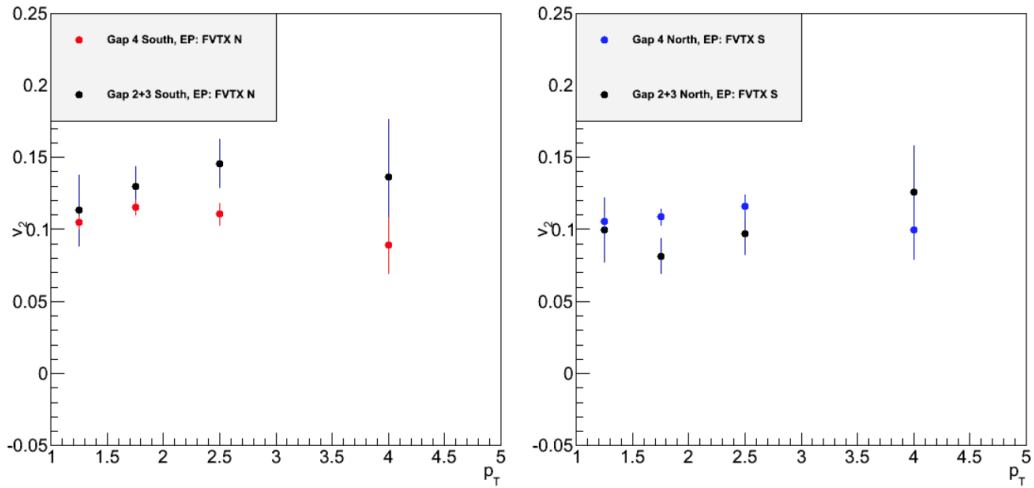


Figure 5.15: Momentum distribution of v_2 for Gap2+3 and Gap 4 tracks, South arm (left) and North arm (right) centrality 20%–40%.

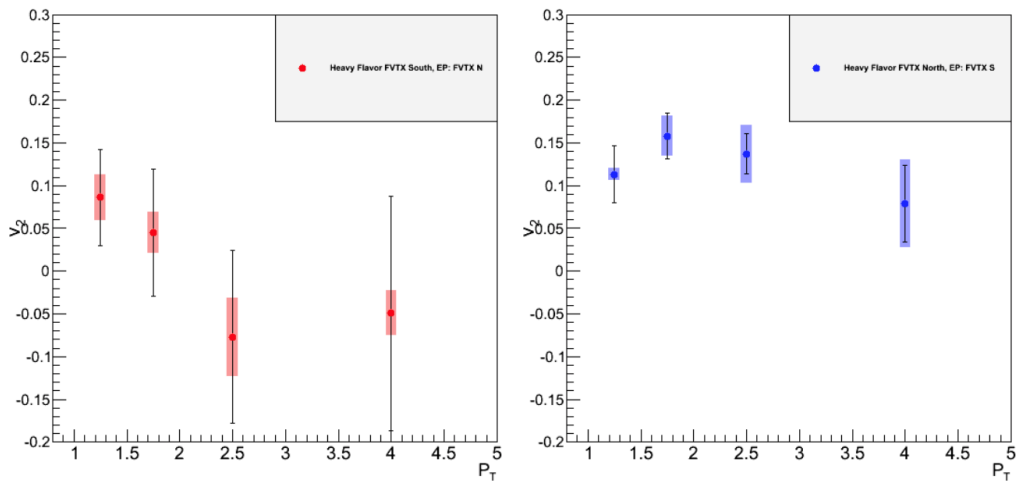


Figure 5.16: Heavy Flavor Single Muon v_2 , South arm (left) and North arm (right) centrality 20%–40%.

Chapter 6

Systematic Errors

6.1 Uncertainty in Single Muon Yield

The uncertainties in this measurement consist of statistical fluctuations as well systematic uncertainties associated with the measurement and the analysis method. The heavy flavor single muon yield can be expressed as:

$$\frac{d^2N^{HF}}{2\pi p_T dp_T d\eta} = \frac{1}{2\pi p_T \Delta p_T \Delta\eta} \frac{N^{inc} - N^{cocktail}}{A\epsilon} \quad (6.1)$$

where N^{HF} is the number of heavy flavor single muons, N^{inc} is the inclusive gap 4 yield, $N^{cocktail}$ is the background predicted by the cocktail method, and $A\epsilon$ is the correction due to acceptance and efficiency. The total systematic uncertainty(σ^{HF}) in N^{HF} is due to uncertainties(σ^{inc} , $\sigma^{cocktail}$, and $\sigma^{A\epsilon}$) in N^{inc} , $N^{cocktail}$, and $A\epsilon$. The total error associated with the measurement consist of three seperate types of uncertainty (Types A, B, and C). Type-A uncertainties are uncorrelated point-to-point. The points can move within the error bars independent of each other. For this analysis, the only Type-A uncertainty is due to the statistical fluctuations of the data. Type-B uncertainties are correlated between bins to some degree. The points move together within the error bars in a correlated manner, e.g., if the value in one bin goes up then the value in all bins goes up, though not necessarily by the same amount. Type-C uncertainanies represent a global uncertainty on the measurement. In this case, all the bins will move together in a highly correlated manner. The values may

Table 6.1: Table of Type B Point-to-Point Systematic Uncertainties in Single Muon Yield, Centrality 0%–20%.

Systematic	Type	$1.5 < p_T < 1.75$ South (North)	$3.5 < p_T < 4$ South (North)
σ^{tune}	$N_{cocktail}$	11.77 (1.08) %	7.9 (47.26) %
$\sigma^{K/\pi}$	$N_{cocktail}$	15 %	15 %
$\sigma^{A\epsilon_{reco}}$	$A\epsilon_{reco}$	0.37 (0.36) %	4.7 (4.5) %

Table 6.2: Table of Type C Global Systematic Uncertainties in Single Muon Yield.

Systematic	South (North)
$\sigma^{run-to-run}$	9.1 (7.9) %
σ^{trig}	3 (3) %
$\sigma^{zvtx_{cut}}$	4 (2) %
σ^{MuID}	2 (2) %
σ^{MuTr}	2 (2) %
σ^{p_T}	5 (5) %
Total	15 (14.3) %

move by a relative error, for example, 10%, and the absolute error will depend on the value on the y-axis. The difference between Type-B and Type-C, then, is that Type-B errors may be a different relative error bin to bin. These consist of errors associated with only N^{inc} , $N_{cocktail}$, or $A\epsilon$. Type-C errors are associated with the final heavy flavor yield, and are applied globally. Tables 6.1 and 6.2 list the different uncertainties and some typical values (the values will vary in different centrality and p_T bins).

6.1.1 Type-B Systematics

The largest source of uncertainty is due to the background estimation. The K/π ratio of the input spectra and the weights used to tune the cocktail both contribute to the total systematic uncertainty.

In order to estimate the effect of the K/π ratio on the final single muon yield, the ratio is varied by $\pm 30\%$ [36]. The extent to which the signal varies due to the variation of the K/π ratio is taken as the uncertainty due to this ratio, $\sigma^{K/\pi}$. The heavy flavor yields vary by less than $\approx 15\%$ in all centrality bins. Therefore, a conservative uncertainty of 15% is attributed to the measurement.

Similarly, the effect of the reweighting is estimated by comparing two different reweighting optimizations. As described in Section 4.6.1, the parameters in Equation 4.6 are varied to estimate the systematic uncertainty on the cocktail tuning. Figures 6.1 (South arm) and 6.2 (North arm) show the ratio for two different tunings, one using the ratio 1:1:1 and one using 1:1:2, of the final weighted spectra in the 20 – 40% centrality bin. The percent difference is taken as the one standard deviation value of the uncertainty due to the reweighting. The quadratic sum of these two uncertainties is the uncertainty on the cocktail.

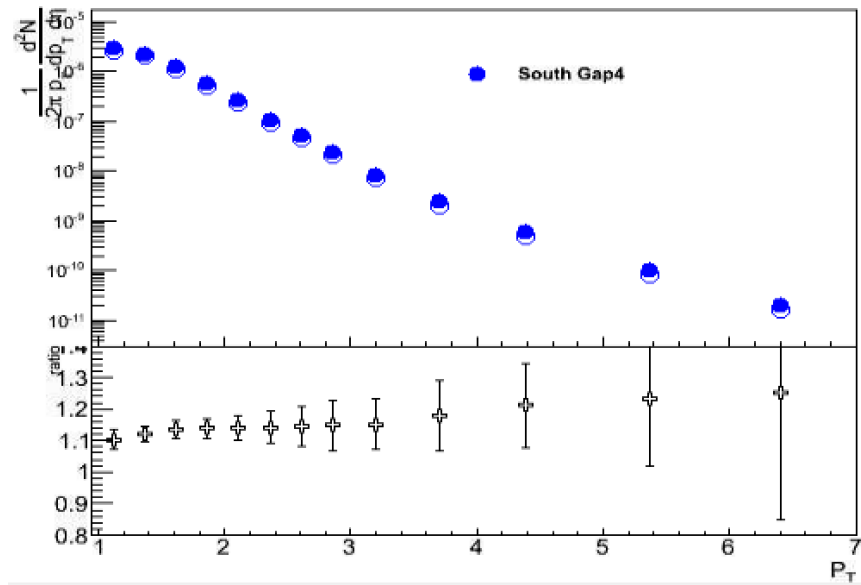


Figure 6.1: Tuned cocktail using different reweighting parameters in the south arm. Open points are made using a relative ratio of 1:1:1 for parameters a:b:c. The closed points use a relative ratio of 1:1:2 for parameters a:b:c. The ratio in the bottom panel is the closed points divided by the open points.

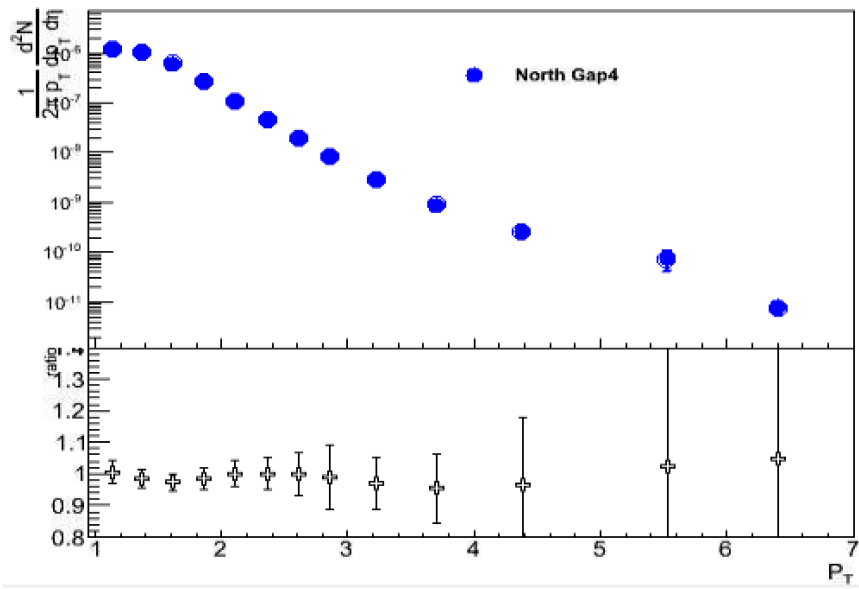


Figure 6.2: Tuned cocktail using different reweighting parameters in the north arm. Open points are made using a relative ratio of 1:1:1 for parameters a:b:c. The closed points use a relative ratio of 1:1:2 for parameters a:b:c. The ratio in the bottom panel is the closed points divided by the open points.

Once the uncertainty on the background is estimated, it must be propagated through the calculation in order to find the relative uncertainty, F_{HF} on the heavy flavor yield. The number of heavy flavor muons in a p_T -bin is the difference between the inclusive yield and the background prediction (Equation 6.2). The squared uncertainty then is just the sum of the squares of the uncertainties on the two components (Equation 6.3). In order to write the relative uncertainty on the heavy flavor yield, multiply each term in Equation 6.3 by N_{xx}^2/N_{xx}^2 to yield Equation 6.4.

$$N_{HF} = N_{inc} - N_{cocktail} \quad (6.2)$$

$$\sigma_{HF}^2 = \sigma_{inc}^2 + \sigma_{cocktail}^2 \quad (6.3)$$

$$N_{HF}^2 \left(\frac{\sigma_{HF}}{N_{HF}} \right)^2 = N_{inc}^2 \left(\frac{\sigma_{inc}}{N_{inc}} \right)^2 + N_{cocktail}^2 \left(\frac{\sigma_{cocktail}}{N_{cocktail}} \right)^2 \quad (6.4)$$

Here it is assumed that the uncertainty on the inclusive spectra is negligible, $\frac{\sigma^{inc}}{N^{inc}} = 0$ [31]. It is then just a matter of rearranging the terms to show that the relative error on the heavy flavor yield is the relative error on the cocktail multiplied by the inverse of the signal-to-background ratio, as seen in Equation 6.5.

$$\frac{\sigma_{HF}}{N_{HF}} = F_{HF} = \frac{N_{cocktail}}{N_{HF}} F_{cocktail} = (S/B)^{-1} F_{cocktail} \quad (6.5)$$

The relative systematic uncertainty on the heavy flavor yield due to the cocktail, F_{HF} , is then added in quadrature with the statistical uncertainty on the acceptance*efficiency correction factor. The result is the Type-B systematic uncertainty on the measurement.

6.1.2 Type-C Systematics

The global uncertainty in the heavy flavor yield comes from a variety of sources. The trigger efficiency, detector efficiencies (MuID and MuTr), intrinsic momentum resolution of the MuTr, run to run variation (Figure 4.2) in tracks per event, and the z-vertex cut used on the data all contribute. The trigger efficiency, detector efficiencies, and intrinsic momentum resolution have all been estimated in previous analyses [32, 24]. Those values have been used in this analysis.

In this analysis, the z-vertex range is restricted to ± 10 cm, as opposed to the ± 25 cm range used in previous analyses [36, 31, 28]. This is due to the addition of the FVTX detector, which restricts the range to ± 15 cm, as well as the PHENIX collaboration’s choice to use a narrow vertex trigger to optimize for events with ± 10 cm. The previous analyses were then able to apply a ‘near-side cut’ on the data. This cut was used to reject events that were far from the detector in question. Therefore, the south arm measurement was performed using events in the range $-25 < z < 0$ and the north arm measurement with events in the range $0 > z > 25$. The restricted range in the Cu+Au data set precludes a near side cut in this analysis. However, as was discussed previously, the z-vertex distribution is shifted away from the south arm, creating an effective far-side cut in the south arm, and near-side cut in the north arm. The heavy flavor signal is sensitive to the z-vertex cut used. In particular, a cut at ± 15 cm introduces a background component which is unexplained by simulation. This

Table 6.3: Table of Systematic Uncertainties in R_{AA} .

Systematic	Type	Value
$\sigma^{N_{coll}}$	Type C	12 %
σ^{pp}	Type B	10 %
$\sigma_{R_{AA}}$		15 %

can be seen in the dramatic rise of the z-vertex slopes when using this cut. The dependence of the slopes on this cut is minimized with a narrow vertex cut. An even tighter cut of ± 8 cm has little effect on the slopes, relative to the ± 10 cm cut. The narrow 10 cm cut is used in this analysis, and the extent to which the heavy flavor yield changes with this cut is taken as an asymmetric systematic uncertainty. A wider (than 10 cm) z-vertex cut tends to overestimate the background component and underestimate the signal. Conversely, a narrower cut has little effect on the signal.

6.2 Uncertainty in Nuclear Modification Factor

The calculation of the nuclear modification factor, R_{AA} , introduces an additional uncertainty due to the statistical error associated with the glauber models estimation of N_{coll} as well as the statistical and systematic uncertainty on the $p + p$ reference [36]. Table 6.3 shows the value of these errors for the 20-40% centrality bin.

6.3 Uncertainty in R_{CP}

The observable R_{CP} offers some benefits and drawbacks compared to the nuclear modification factor, R_{AA} . R_{CP} is defined as the fraction with heavy flavor spectra in central collisions in the numerator and the same spectra in peripheral collisions in the denominator. In the most peripheral collisions there are few nucleon-nucleon interactions and the system approximates a proton-proton collision.

The value R_{CP} benefits from the fact that the numerator and denominator are measured in the same analysis. For this reason, the Type-B systematics are correlated to some degree, while the Type-C systematics mostly cancel (with the exception of Type-C systematics which

Table 6.4: Table of Systematic Uncertainty in Azimuthal Anisotropy.

Systematic	Type	$1 < p_T < 1.5$ South (North)	$3 < p_T < 5$ South (North)
σ^{BGv_2}	Type B	4.7 (1.1) %	10.3 (15.2) %
$\sigma^{S/B}$	Type B	30 (2.5) %	49 (6.5) %
σ^{EP}	Type B	9.1 (5.4) %	18.7 (63.3) %
$\sigma^{FakeTracks}$	Type C	10 %	10%

are arm dependent). Since the uncertainty due to the K/π ratio is centrality independent, this uncertainty cancels as well. In order to estimate the level at which the cocktail tuning affects R_{CP} , the percent difference between R_{CP} 's measured using the different tuning parameters is taken as a one standard deviation systematic uncertainty. The reason the errors for the two centrality bins are not simply added in quadrature is that they are highly correlated, though not so much that they completely cancel.

6.4 Uncertainty in Azimuthal Anisotropy

The systematic uncertainty in the azimuthal anisotropy measurement is primarily due to the uncertainty in the signal-to-background measurement in the muon spectra analysis. Equation 5.1 can be written as:

$$v_2^{HF} = \left(1 + \frac{1}{S/B}\right)v_2^{inc} - \frac{1}{S/B}v_2^{BG}. \quad (6.6)$$

The uncertainty also has contributions from the event plane measurement, the uncertainty in the estimated background v_2 , and the contribution of fake tracks within the data set. The relative contributions are shown in Table 6.4.

The uncertainty in the signal-to-background ratio are the statistical and systematic error of the measured signal-to-background measured in the previous chapter added in quadrature. The uncertainty from the event plane determination is described by the extent to which the v_2 measurement differs when different detectors are used for the event plane. In this analysis, the BBC and FVTX detectors both provide an event plane measurement. Figures 6.3 and 6.4 show the inclusive Gap 4 v_2 for different event plane detectors.

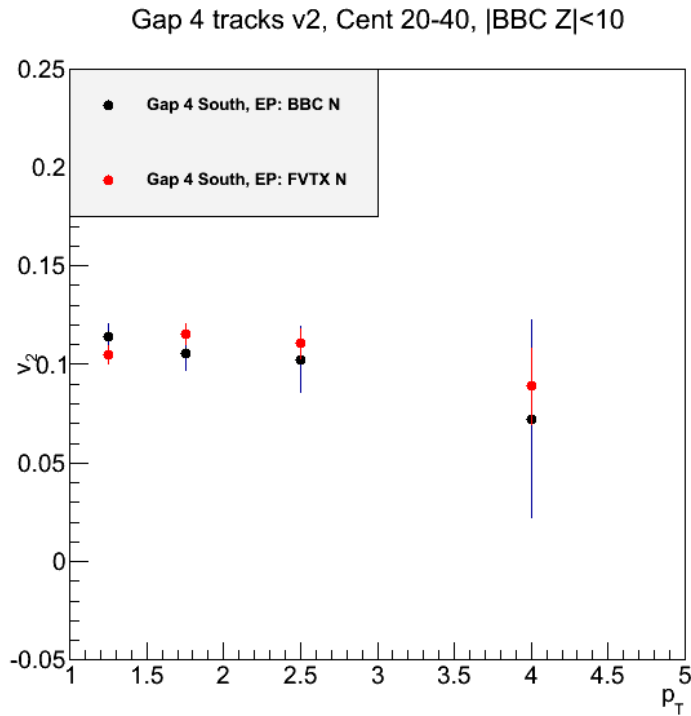


Figure 6.3: Momentum distribution of v_2 using BBC and FVTX event planes, South arm.

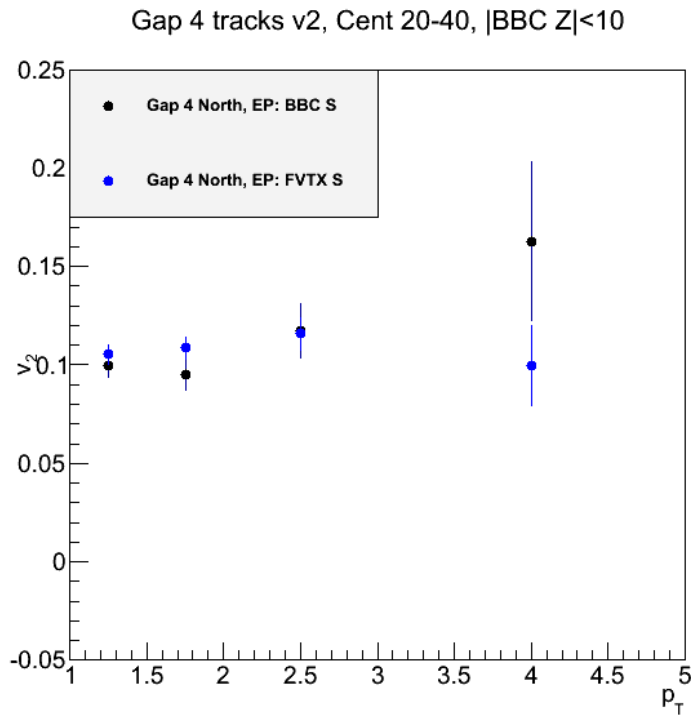


Figure 6.4: Momentum distribution of v_2 using BBC and FVTX event planes, North arm.

In order to estimate the background associated with the background v_2 measurement, the v_2 of punchthroughs and decay muons are compared to the reconstructed Gap 2+3 v_2 in simulation. The decay muons are the largest component of the background, so the extent to which the reconstructed v_2 in Gaps 2 and 3 matches the decay muon v_2 is used as a one standard deviation uncertainty.

Finally, to estimate the contribution of fake tracks to the inclusive v_2 measurement, the various cuts used in the single muon yield analysis are varied. The percent difference between “loose” and “tight” cuts are used as a one standard deviation uncertainty. The fake tracks are assumed to have a non-negligible v_2 . The tracking efficiency shows a dependence on multiplicity, and may be lower in-plane as opposed to out-of-plane. On the other hand, the higher multiplicity in-plane will lead to more fake tracks in plane. This effect was considered in detail previously in a muon arm flow analysis in Au+Au collisions[49]. Figure 6.5 shows the effect of the correction applied from said previous analysis. The correction brings the v_2 from the two arms together, which is to be expected in the symmetric $Au + Au$ collisions. It is unclear what to expect from the asymmetric Cu+Au collisions. While the effect is non-negligible in the cited analysis, it is far below the other systematic uncertainties in this analysis. Therefore, a conservative estimate of 10% is taken as the one standard deviation value of the uncertainty due to fake tracks.

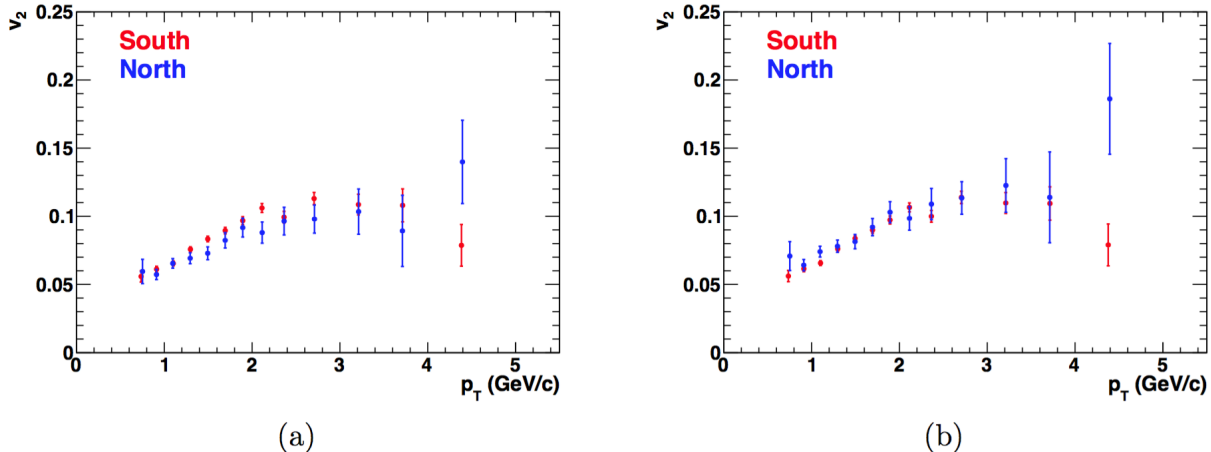


Figure 6.5: The left hand panel shows v_2 before the correction is applied. The right hand panel shows the corrected v_2 . [49]

Chapter 7

Results and Discussion

The heavy flavor single muon invariant yield and azimuthal anisotropy coefficient, v_2 , has been measured at forward angles ($1.4 < |\eta| < 1.9$) in Cu+Au collisions at a center-of-mass energy of 200 GeV per nucleon. This analysis expands upon previous analyses completed at the University of Tennessee and elsewhere [11, 6]. In particular, this analysis takes advantage of the new FVTX detector in order to make accurate event plane measurements which allow a more meaningful anisotropy measurement to be included, as well as benefitting from the installation of additional absorber material which provides additional hadron rejection. In addition, the single muon code framework has been overhauled in an attempt to make the analysis code less cumbersome and more accessible.

7.1 Heavy Flavor Single Muon Spectra

Figures 7.1 and 7.2 show the heavy flavor single muon invariant yield for the 0-20% and 20-40% and centrality bins. A consistent trend is immediately noticeable in that the South arm (Au-going) exhibits a systematically lower yield in all but the most central collisions, while the North arm exhibits a lower yield for most p_T bins in the most central collisions. In contrast, the inclusive candidate spectra shows higher multiplicity in the Au-going direction in all centralities. The larger inclusive yield in the south arm is due, in large part, to the increased background in the south arm due to the z-vtx shift of the event distributions,

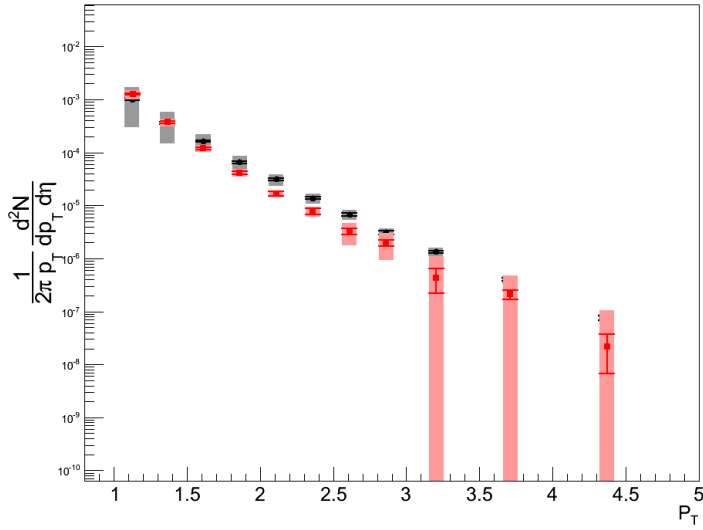


Figure 7.1: Heavy flavor single muon invariant differential yields for south (black) and north (red) arms (Centrality 0-20%). Error bars represent the Type-A statistical uncertainty. Error bands represent the Type-B systematic uncertainty. A Type-C global uncertainty of $\approx 15\%$ underlays the measurement.

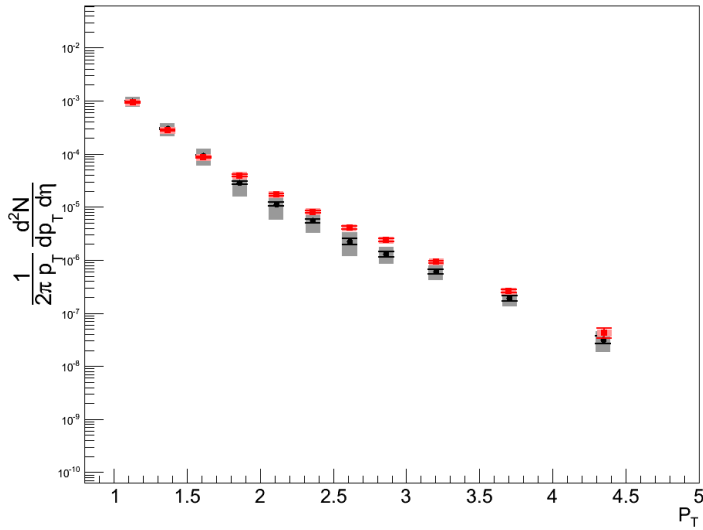


Figure 7.2: Heavy flavor single muon invariant differential yields for south (black) and north (red) arms (Centrality 20-40%). Error bars represent the Type-A statistical uncertainty. Error bands represent the Type-B systematic uncertainty. A Type-C global uncertainty of $\approx 15\%$ underlays the measurement.

which lead to relatively larger decay muon yields in the Au-going direction, as compared to the Cu-going. This effect is reflected in the size of the systematic uncertainties associated with each arm. Specifically, the systematic uncertainties increase significantly as the signal-to-background decreases. The number of heavy flavor muons is the difference between the inclusive yield and the background prediction, therefore the uncertainty on the heavy flavor muons is proportional to the absolute, rather than relative, uncertainty of the background. When the background is accounted for, the Au-going direction then shows significant suppression relative to the Cu-going arm in the three most peripheral bins (see Figures 7.2, 7.3, and 7.4). The larger energy density at backwards rapidity may lead to a hotter medium at backwards rapidities, though the increased suppression in the Cu-going direction in the most central collisions seems to suggest that cold nuclear matter effects are an important factor as well.

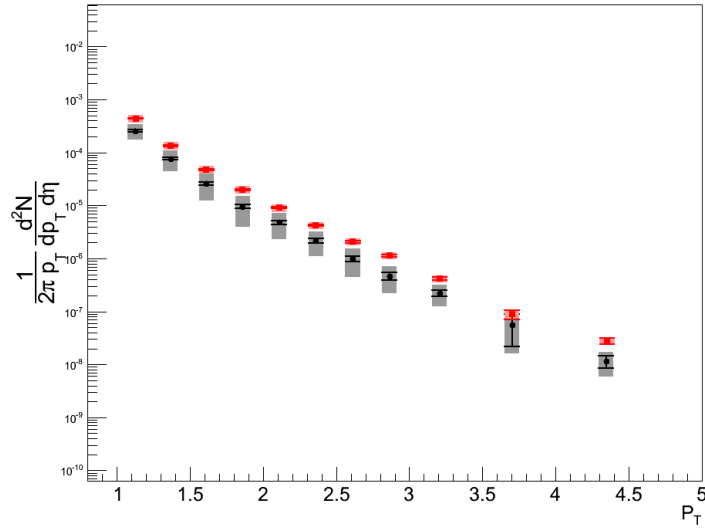


Figure 7.3: Heavy flavor single muon invariant differential yields for south (black) and north (red) arms (Centrality 40-60%). Error bars represent the Type-A statistical uncertainty. Error bands represent the Type-B systematic uncertainty. A Type-C global uncertainty of $\approx 15\%$ underlays the measurement.

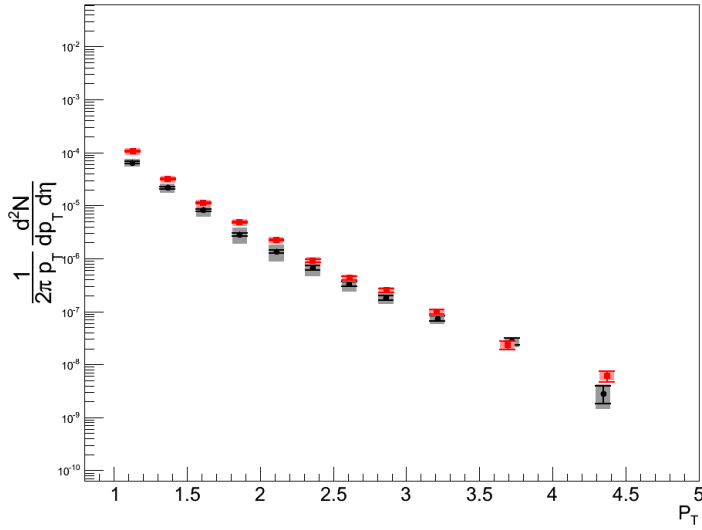


Figure 7.4: Heavy flavor single muon invariant differential yields for south (black) and north (red) arms (Centrality 60-93%). Error bars represent the Type-A statistical uncertainty. Error bands represent the Type-B systematic uncertainty. A Type-C global uncertainty of $\approx 15\%$ underlays the measurement.

7.2 Heavy Flavor Single Muon R_{AA}

Figures 7.5-7.8 show the heavy flavor single muon R_{AA} for the various centrality bins. The pp -reference [6] is taken from a previous analysis, and as such, all uncertainties are uncorrelated with the Cu+Au measurement. Due to the fact that the normalization factor N_{coll} does not depend on rapidity, the same trends (north/south) seen in the heavy flavor spectra are seen in the nuclear modification factor. The most peripheral bin shows significant enhancement, albeit with very large systematics. Indeed, when considering all uncertainties, the R_{AA} is consistent with unity. Conversely, the most central bin shows significantly more suppression in the Cu-going direction, particularly for $p_T > 2$ GeV. Meanwhile, the modification factor in the Au-going direction is larger relative to the Cu-going direction. The most central bin is the only bin in which the Cu-going R_{AA} is smaller than the Au-going R_{AA} . It is clear that increasingly central collisions exhibit increasing levels of suppression for both the Cu-going and Au-going directions.

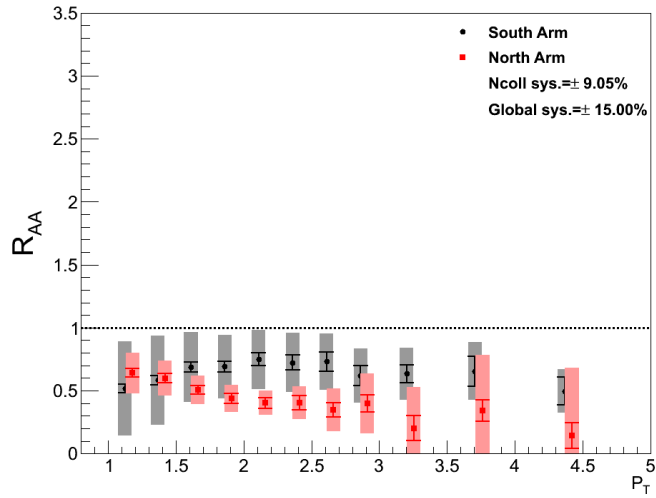


Figure 7.5: Heavy flavor single muon R_{AA} for south (black) and north (red) arms (Centrality 0-20%). Error bars represent the Type-A statistical uncertainty. Error bands represent the Type-B systematic uncertainty. A Type-C global uncertainty of $\approx 15\%$ (from the HF yield) and an uncertainty of $\approx 9\%$ due to the statistical fluctuations in N_{coll} underlay the measurement (indicated in legend).

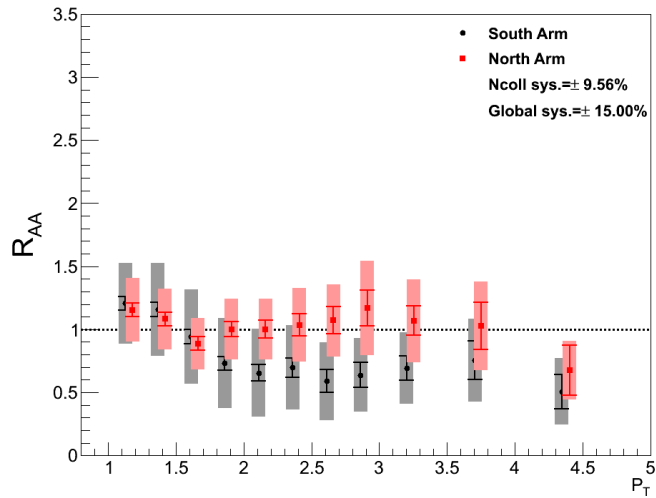


Figure 7.6: Heavy flavor single muon R_{AA} for south (black) and north (red) arms (Centrality 20-40%). Error bars represent the Type-A statistical uncertainty. Error bands represent the Type-B systematic uncertainty. A Type-C global uncertainty of $\approx 15\%$ (from the HF yield) and an uncertainty of $\approx 10\%$ due to the statistical fluctuations in N_{coll} underlay the measurement (indicated in legend).

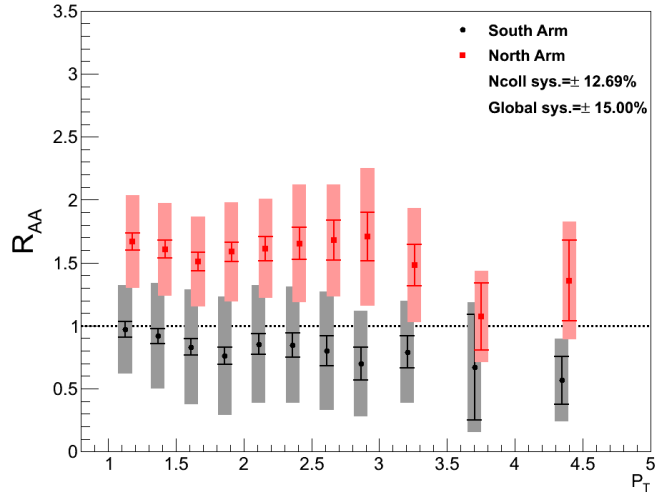


Figure 7.7: Heavy flavor single muon R_{AA} for south (black) and north (red) arms (Centrality 40-60%). Error bars represent the Type-A statistical uncertainty. Error bands represent the Type-B systematic uncertainty. A Type-C global uncertainty of $\approx 15\%$ (from the HF yield) and an uncertainty of $\approx 12\%$ due to the statistical fluctuations in N_{coll} underlay the measurement (indicated in legend).

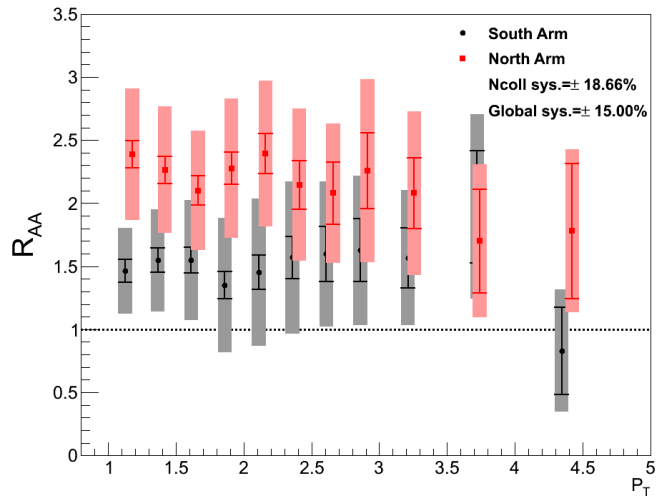


Figure 7.8: Heavy flavor single muon R_{AA} for south (black) and north (red) arms (Centrality 60-93%). Error bars represent the Type-A statistical uncertainty. Error bands represent the Type-B systematic uncertainty. A Type-C global uncertainty of $\approx 15\%$ (from the HF yield) and an uncertainty of $\approx 19\%$ due to the statistical fluctuations in N_{coll} underlay the measurement (indicated in legend).

7.3 Heavy Flavor Single Muon R_{CP}

Figures 7.9-7.11 show the heavy flavor single muon R_{CP} for the three most-central centrality bins. While the shape of R_{CP} for a particular arm and centrality bin resembles that of the R_{AA} in the same bin, the magnitude and ratio between north and south is quite different. In other words, the $\langle N_{coll} \rangle$ weighted heavy flavor spectra in peripheral collisions does not approximate the heavy flavor spectra for pp -collisions very well here.

Figure 7.12-7.15 show the ratio between the Au-going and Cu-going arms for the two most central bins. Notably, the ratios for R_{CP} and R_{AA} are consistent with each other for a particular centrality bin. It is interesting that the ratio is below one in the 0-20% centrality bin and above one for the 20-40% centrality bin. The implications of this is discussed in the following section.

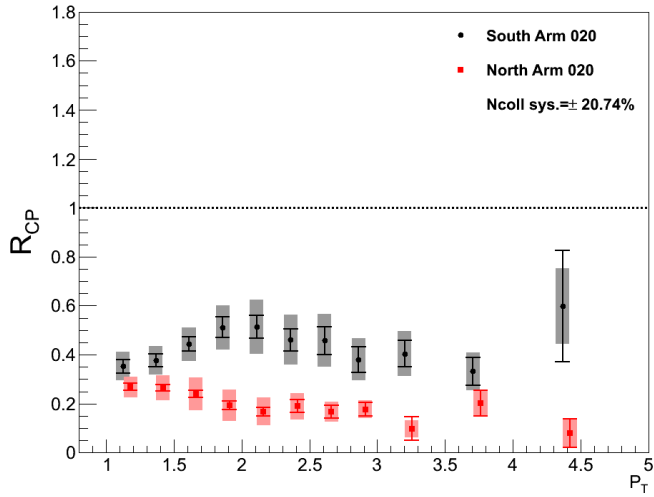


Figure 7.9: Heavy flavor single muon R_{CP} for south (black) and north (red) arms (Centrality 0-20%). Error bars represent the Type-A statistical uncertainty. Error bands represent the Type-B systematic uncertainty. A Type-C global uncertainty of $\approx 20\%$ due to the statistical fluctuations in N_{coll} underlay the measurement (indicated in legend).

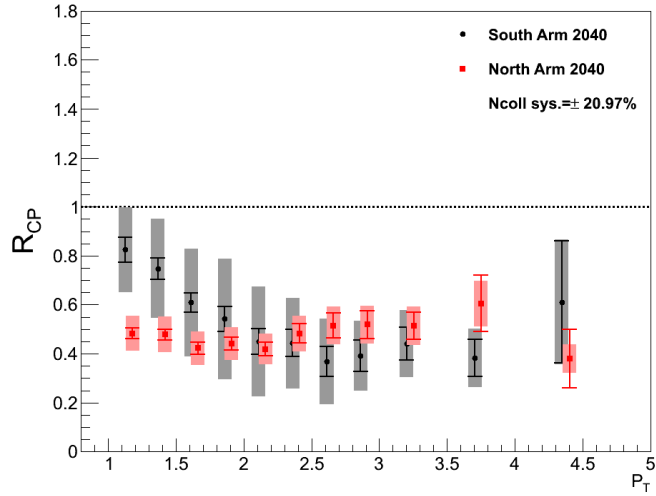


Figure 7.10: Heavy flavor single muon R_{CP} for south (black) and north (red) arms (Centrality 20-40%). Error bars represent the Type-A statistical uncertainty. Error bands represent the Type-B systematic uncertainty. A Type-C global uncertainty of $\approx 21\%$ due to the statistical fluctuations in N_{coll} underlay the measurement (indicated in legend).

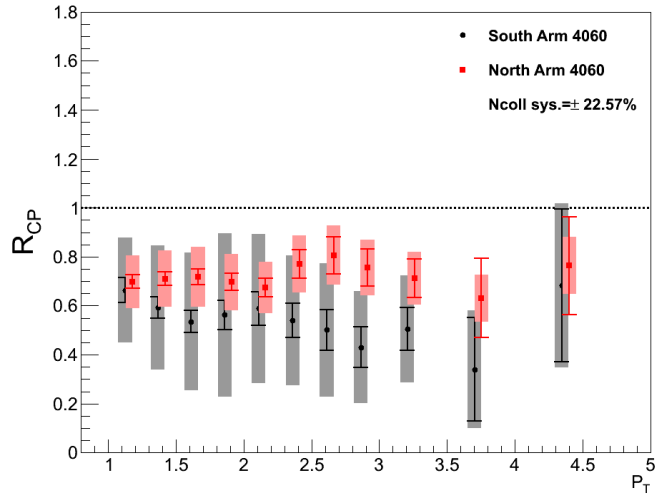


Figure 7.11: Heavy flavor single muon R_{CP} for south (black) and north (red) arms (Centrality 40-60%). Error bars represent the Type-A statistical uncertainty. Error bands represent the Type-B systematic uncertainty. A Type-C global uncertainty of $\approx 23\%$ due to the statistical fluctuations in N_{coll} underlay the measurement (indicated in legend).

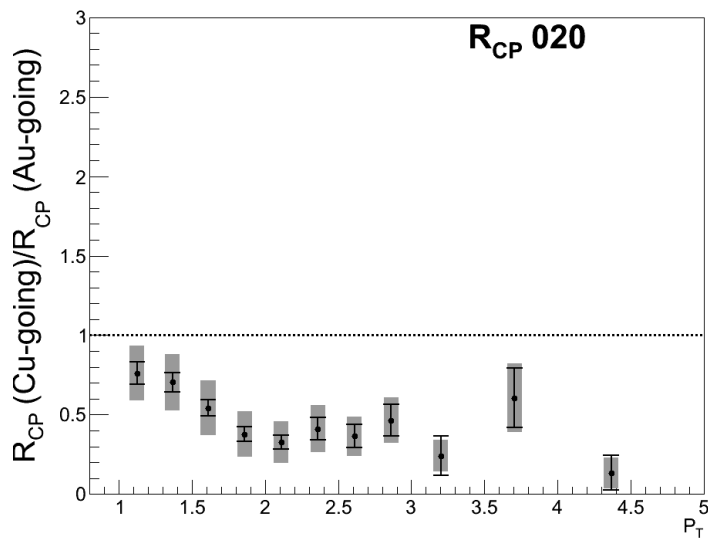


Figure 7.12: Ratio of $R_{CP}(\text{Cu-going})$ to $R_{CP}(\text{Au-going})$ (centrality 0%–20%).

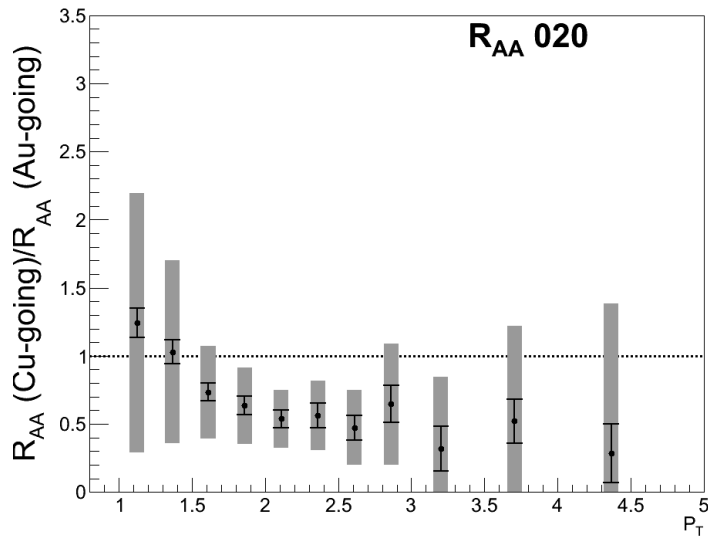


Figure 7.13: Ratio of $R_{CP}(\text{Cu-going})$ to $R_{CP}(\text{Au-going})$ (centrality 20%–40%).

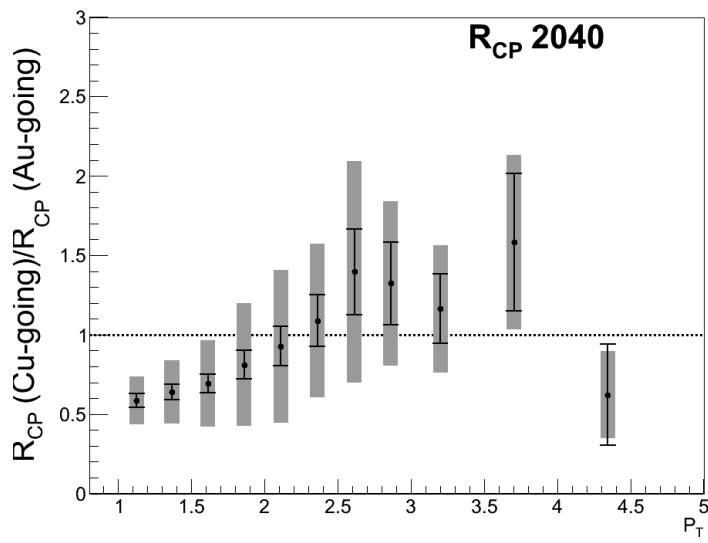


Figure 7.14: Ratio of R_{AA} (Cu-going) to R_{AA} (Au-going) (centrality 0%–20%).

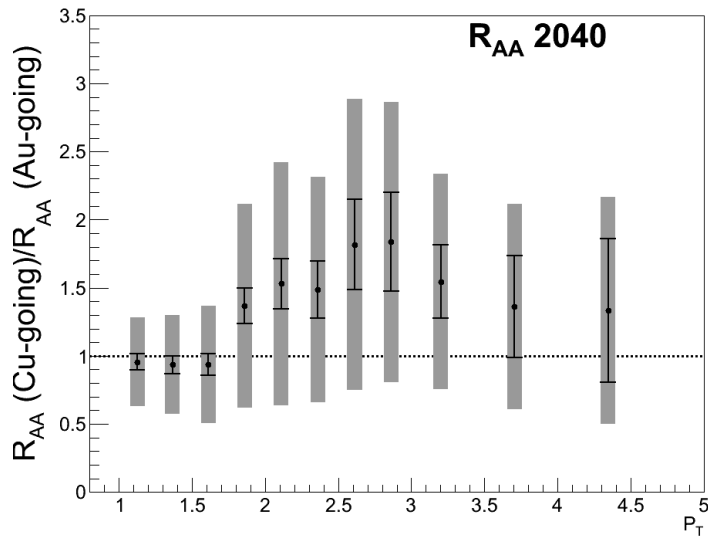


Figure 7.15: Ratio of R_{AA} (Cu-going) to R_{AA} (Au-going) (centrality 20%–40%).

7.4 Heavy Flavor Single Muon v_2

Figure 7.16 shows the heavy flavor single muon anisotropy coefficient, v_2 , as a function of p_T . Within the large error bars, v_2 in the Au-going direction is consistent with zero. In the Cu-going direction, however, the measured v_2 is consistent with a non-zero heavy flavor v_2 . The low signal-to-background ratio in the Au-going direction makes a heavy flavor measurement extremely challenging, as the signal makes such a small contribution to the inclusive measurement. This can be seen in the large statistical uncertainty associated with the measurement in the south arm. The propagated statistical uncertainty is proportional to the inverse square of the signal-to-background. For this reason, a heavy flavor flow measurement requires large statistics in both data and simulation in order to have distinguishing power between theories. Meanwhile, the north arm measurement is less affected by the signal-to-background, however, the systematics are much larger due to the missing octant in the MuTr N. Still, the measurement shows a finite non-zero v_2 .

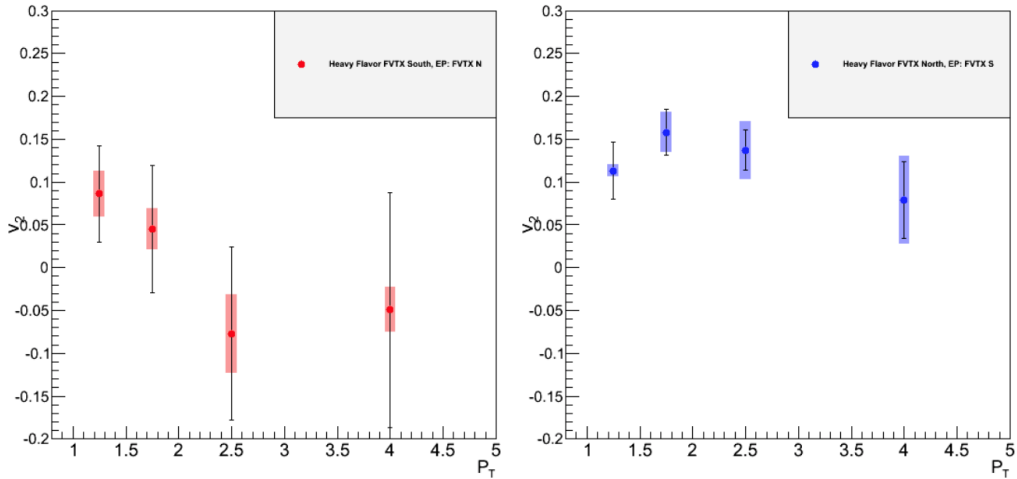


Figure 7.16: Heavy flavor single muon v_2 for the Au-going (left) and Cu-going (right) directions (centrality 20%–40%). Error bars represent the Type-A statistical uncertainty. Error bands represent the Type-B systematic uncertainty.

7.5 Heavy Flavor Single Muon v_3

Figure 7.17 shows the heavy flavor single muon anisotropy coefficient, v_3 , as a function of p_T . The v_3 measurement suffers from the same issues as the v_2 measurement, compounded by the fact that the statistical uncertainty is larger. Furthermore, v_3 is expected to be smaller than v_2 and therefore is more difficult to distinguish from zero. Both arms show a v_3 consistent with zero, though they are dominated by the large statistical uncertainty. Note the scale on the v_3 plots, which is much larger than the scale in the v_2 plots.

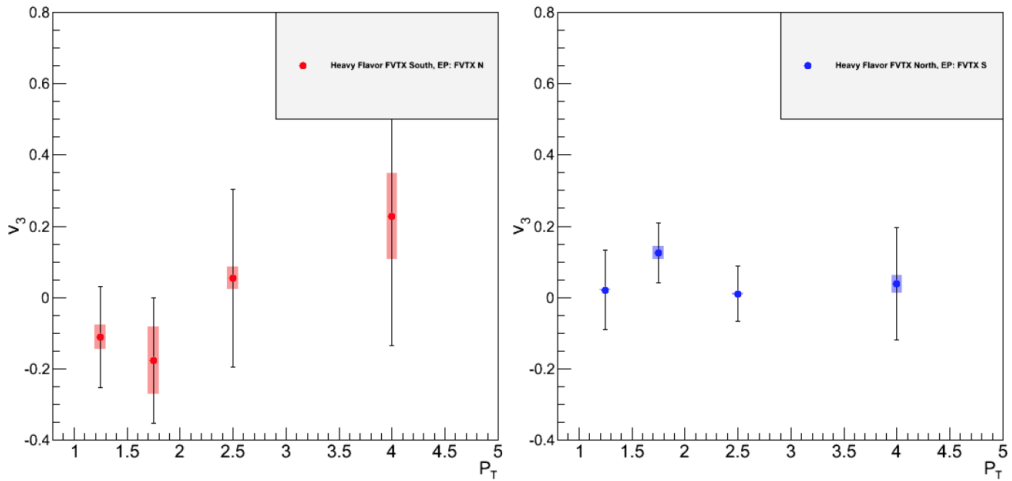


Figure 7.17: Heavy flavor single muon v_3 for the Au-going (left) and Cu-going (right) directions (centrality 20%–40%). Error bars represent the Type-A statistical uncertainty. Error bands represent the Type-B systematic uncertainty.

7.6 Discussion

7.6.1 Nuclear Modification Factor R_{AA}

As discussed in Chapter 2, PHENIX has measured heavy flavor single leptons in a variety of collision systems. The previous analysis by the University of Tennessee group measured heavy flavor single muons in Cu+Cu collisions at $\sqrt{s_{NN}} = 200$ GeV in the same kinematic range as in this analysis. Heavy flavor single electrons have been measured at mid-rapidity in the same collisions. Within the systematic uncertainties, the heavy flavor muon R_{AA} in Cu+Au agrees well with the heavy flavor muon R_{AA} in Cu+Cu (see Figures 7.18 and 7.20) , particularly in the Cu-going direction, for both of the most central bins [11]. In contrast, the heavy flavor muon R_{AA} in Cu+Au is more suppressed (see Figures 7.19 and 7.21) than the heavy flavor electron R_{AA} in Cu+Cu [7]. The Bjorken energy density is expected to be higher in Au+Au collisions, relative to Cu+Cu collisions [11]. It can therefore be assumed that the energy density in Cu+Au collisions is somewhere in between. The suppression seen in heavy flavor muons in Cu+Cu is greater than that seen in the heavy flavor electron measurement. This has been attributed to the cold nuclear matter (CNM) effects, particularly shadowing and initial state energy loss which may be more prevalent in lower energy density systems [7] [11]. Given the agreement between the Cu+Cu muon data and the Cu+Au muon data, one can conclude that CNM effects play a large role in the level of suppression seen.

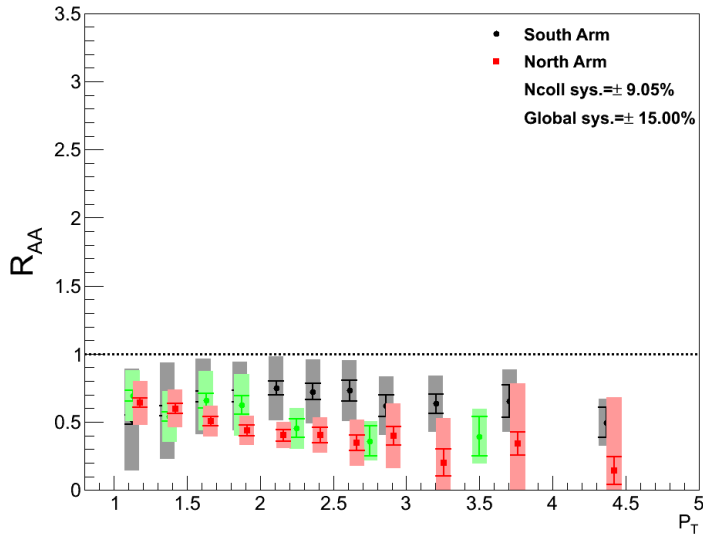


Figure 7.18: Heavy flavor single muon R_{AA} for south (black) and north (red) arms (centrality 0%–20%). The green points are results for heavy flavor muon production at forward rapidity in Cu+Cu collisions [11].

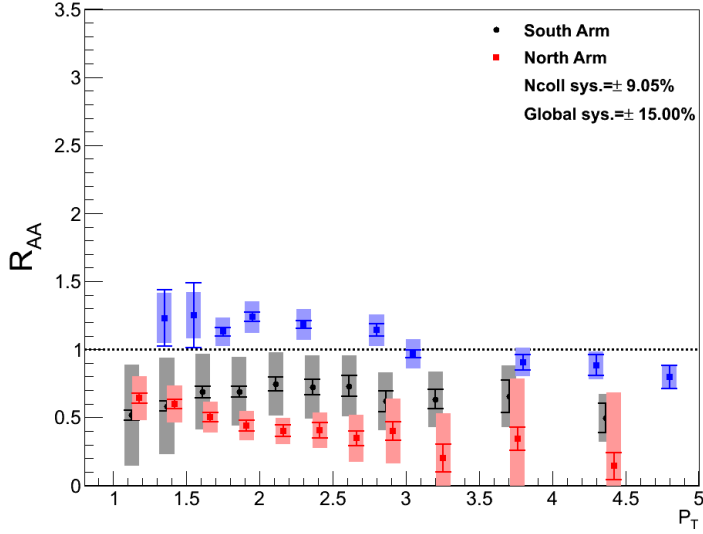


Figure 7.19: Heavy flavor single muon R_{AA} for south (black) and north (red) arms (centrality 0%–20%). The blue points are results for heavy flavor electron production at mid-rapidity in Cu+Cu collisions [7].

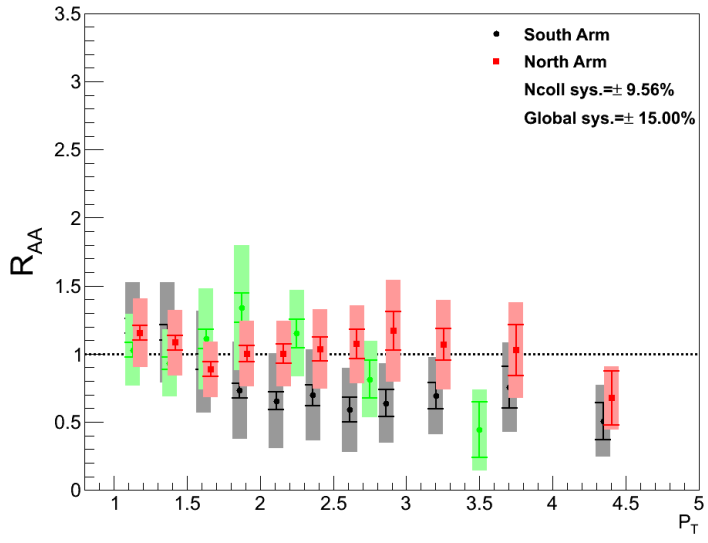


Figure 7.20: Heavy flavor single muon R_{AA} for Au-going (black) and Cu-going (red) directions (centrality 20%–40%). The green points are results for heavy flavor muon production at forward rapidity in Cu+Cu collisions [11].

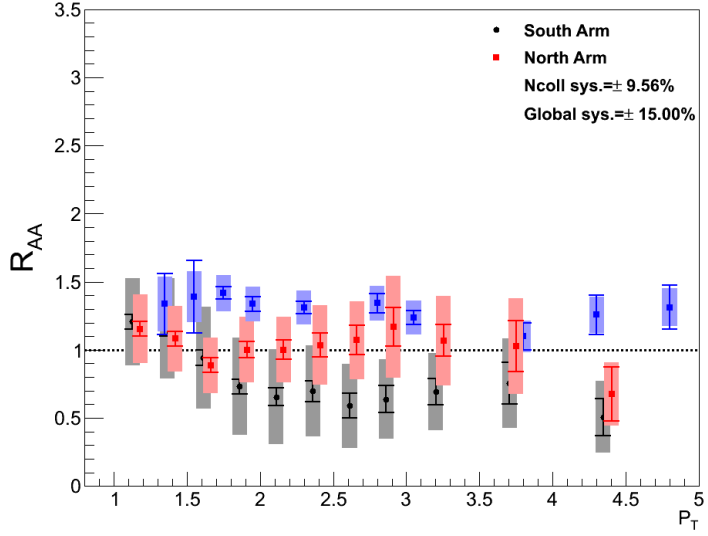


Figure 7.21: Heavy flavor single muon R_{AA} for Au-going (black) and Cu-going (red) directions (centrality 20%–40%). The blue points are results for heavy flavor electron production at mid-rapidity in Cu+Cu collisions [7].

On the other hand, one expects an asymmetric energy density in the asymmetric Cu+Au collisions, where the higher energy density is associated with the Au-going direction. In that case, it is reasonable to assume that CNM effects will be more prevalent in the Cu-going direction than the Au-going. Furthermore, one would expect the hot nuclear matter (HNM) effects, indicative of a QGP, to be more prevalent in the Au-going direction, and therefore lead to more suppression in that direction. However, the results presented in this analysis are at odds with that line of thinking. In the most central bin the Au-going suppression is *weaker* than the Cu-going, while in all other centrality bins the reverse is true. It would seem, then, that the system is not simply described by CNM effects which serve to suppress the heavy flavor yield. One must consider that there are some CNM effects which serve to enhance the yield, such as anti-shadowing, and that these effects may well be different in magnitude in the two directions.

The parton distribution functions (PDF) for the Cu and Au nuclei are not the same. The nature of the forward rapidity measurement ensures that the colliding parton from one nucleus will likely come from the shadowing region while the colliding parton from the other nucleus will likely come from the anti-shadowing region (See Figure 7.22). Since the parton distributions are not the same for the two nuclei, it may be that one colliding parton comes from a region of little shadowing while the other parton comes from a region of extreme anti-shadowing. For example, consider two partons colliding in a Cu+Au collision. If the parton in the Au-nucleus comes from a region of extreme anti-shadowing and the parton in the Cu-nucleus comes from a region of relatively little shadowing, the resulting particle production in the Au-going direction may show enhancement relative to the Cu-going direction.

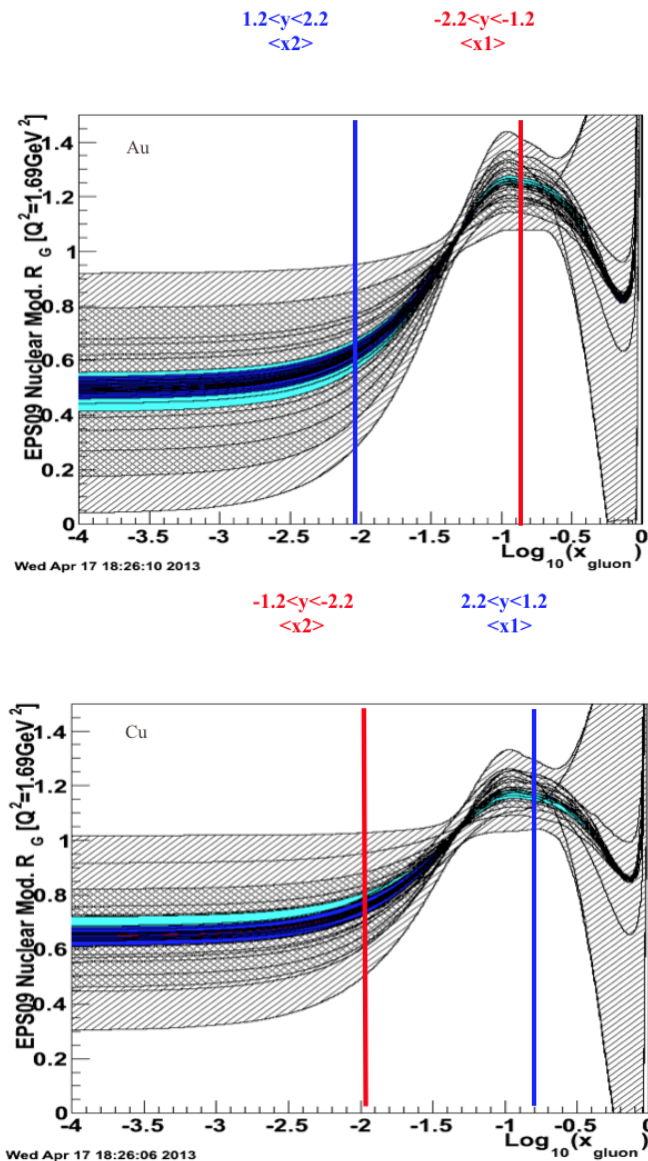


Figure 7.22: Illustration of the Bjorken- x regions of colliding partons within their respective nuclei [2].

However, one must also consider the large multiplicities in central Cu+Au collisions which indicate a higher background. The possibility of an increased source of fake tracks emanating from hadron showers at the back of the absorber in muon arm may play an important role. These showers deposit extra hits in the detector that may be clustered with a real track by the tracking algorithm, or with other hits from these showers creating a completely fake track. At some point, the multiplicity in the detector is so high that the tracking algorithm will not be able to distinguish between real and fake tracks with any reasonable efficiency. In the case that a hit is clustered with a real track (that it does not belong to), tracks may be categorized as having the wrong last gap. For example, a track which stops in Gap 3 may have a hit in Gap 4 which gets clustered with the track, thereby mis-labeling the track as a Gap 4 track, rather than Gap 3. In order to investigate this possibility, a full scale analysis of the PHENIX simulation code is necessary which is out of the scope of this analysis. Beyond that, the effective ‘far-side cut’ due to the shifted z-vtx distribution serves to increase the decay muon fraction in the Au-going direction, further increasing the background in this direction. These effects may account for the enhancement in the the Au-going direction in central collisions relative to the Cu-going direction.

In order to put these measurements on an equal footing with respect to the collision system, these results are also compared with a Phi meson R_{AA} measurement done using the same Cu+Au data set. Figure 7.23 shows the heavy flavor muon R_{AA} for the 20-40% centrality bin compared to the minimum bias phi measurement. In particuar, note the enhancement seen in the Au-going direction at low momentum. It should be noted, the phi meson is not considered a heavy flavor meson as it is composed of strange quarks. Therefore, the level of suppression seen here is not necessarily compareable. It is noteworthy that the south arm shows enhancement over the north arm.

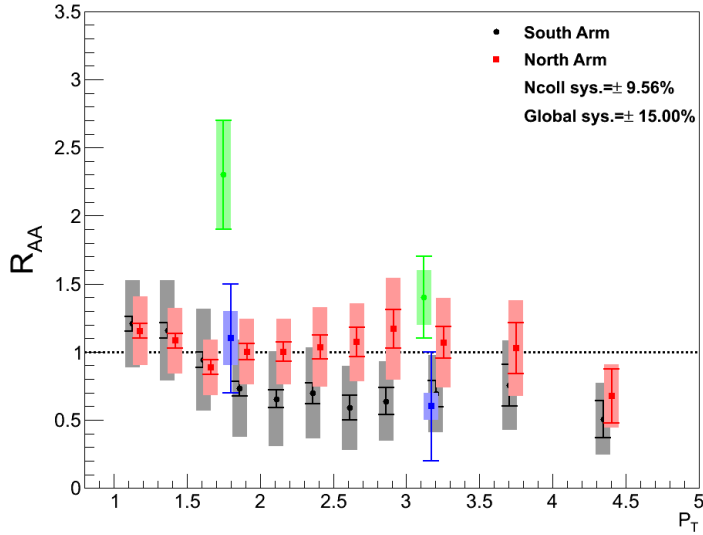


Figure 7.23: Heavy flavor single muon R_{AA} for Au-going (black) and Cu-going (red) directions (centrality 20%–40%). The green (Au-going) and blue (Cu-going) points are results for ϕ meson production at forward rapidity in Cu+Au collisions.

Theoretical calculations have been used for comparison in heavy flavor lepton measurements in Cu+Cu [48]. The theoretical comparisons in the muon analysis are for the most central bin only, and at $p_T > 2.5$ GeV. These calculations agree with the Cu+Cu data well, and similarly with the Cu+Au data. These calculations take into account both elastic and inelastic energy loss, as well as CNM effects relevant to open heavy flavor production such as the multiple scattering of incoming partons before the collision[11]. Figure 7.24 shows the theoretical prediction for the heavy flavor electron R_{AA} at mid-rapidity in both Cu+Cu and Au+Au collisions, as well as data from PHENIX and STAR from central Au+Au collisions. The calculations clearly predict a difference in suppression between Cu+Cu and Au+Au collisions. Therefore, heavy flavor muon measurements in Au+Au would be very useful in untangling the CNM and HNM effects.

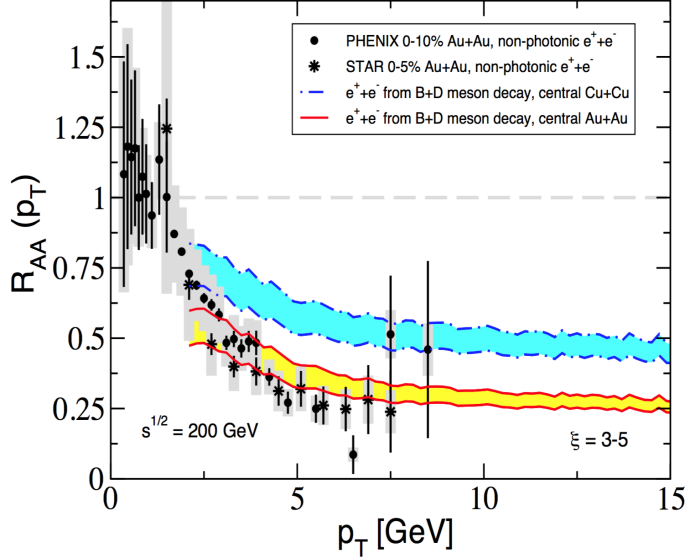


Figure 7.24: Nuclear modification for the single non-photonic electrons in central Au+Au and Cu+Cu collisions at RHIC. Data is from PHENIX and STAR collaborations [48].

7.6.2 v_2

The heavy flavor v_2 measured in this analysis has error bars so large that it is difficult to make any meaningful conclusions. However, it is informative to see what others have measured for heavy flavor v_2 recently. Figure 7.25 shows the heavy flavor single muon v_2 for 20-40% centrality collisions measured at ALICE, also shown in Chapter 2. The measurement is in 2.76 TeV *symmetric* Pb+Pb collisions at higher rapidity, and (mostly) higher p_T . The measurement is also done using 3 different methods, which are all plotted. The v_2 measured at ALICE is consistent with a non-zero v_2 using the cumulant methods (red and green), while the scalar product method shows a v_2 consistent with zero.

While the heavy flavor flow measurement does not have much distinguishing power, the hadron flow measurement that serves as a background is unaffected by the uncertainty in the signal-to-background. Figure 7.26 shows the hadron v_2 for the Au-going and Cu-going directions from this analysis (blue), respectively, with the hadron v_2 measured in a previous PHENIX combined-arms analysis (red) [49]. The previous measurement was made in the muon arm in 200 GeV symmetric Au+Au collisions, and in this case both arms are combined for one measurement.

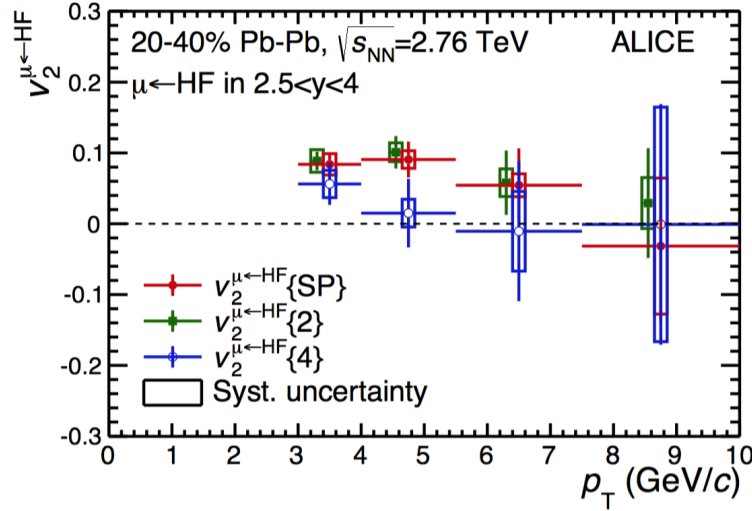


Figure 7.25: p_T -differential elliptic flow of muons from heavy-flavour decays in $2.5 < y < 4$ [19].

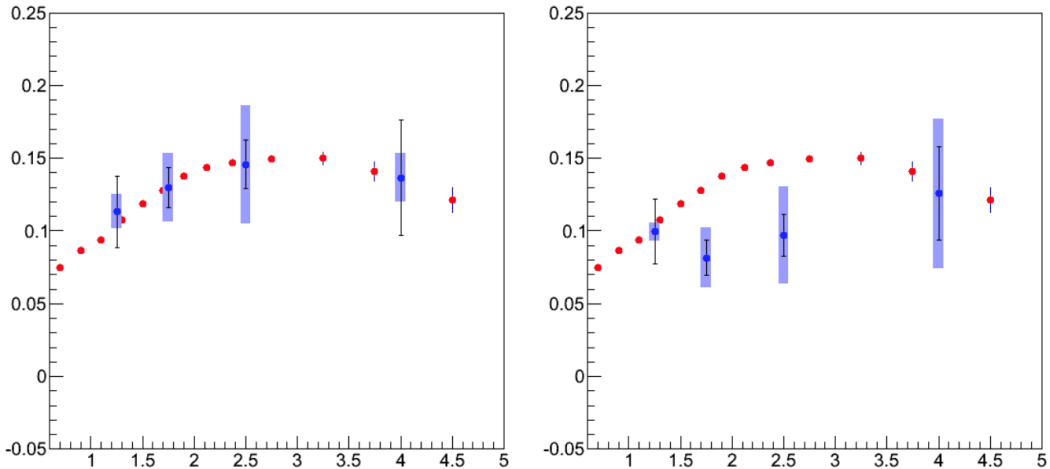


Figure 7.26: Hadron v_2 (blue) for the Au-going (left) and Cu-going (right) directions (centrality 20%–40%) and previous PHENIX combined-arms analysis (red). Error bars represent the Type-A statistical uncertainty. Error bands represent the Type-B systematic uncertainty.

Chapter 8

Summary and Conclusions

In this dissertation, the heavy flavor single muon invariant yields for multiple centrality bins (0-20%, 20-40%, 40-60%, and 60-93%) has been measured in Cu+Au collisions at a center of mass energy of 200 GeV per nucleon in the PHENIX experiment at the Relativistic Heavy Ion Collider at Brookhaven National Laboratory. The nuclear modification factor, R_{AA} and its analog, R_{CP} , have also been measured, with the pp -reference in R_{AA} taken from a previous analysis [6]. This dissertation presents a number of improvements on previous analyses. In particular, the azimuthal anisotropy coefficients v_2 and v_3 has been measured in the mid-central bins (v_2 and v_3 in 20-40% and v_2 in 40-60%). Furthermore, the implementation of GEANT4 within the PHENIX Monte Carlo package (PISA) has replaced the many different GEANT3 packages, simplifying the analysis and reducing the systematic uncertainty due to the various packages. Additional absorber has been installed in front of the muon arms, providing further hadron rejection. The inclusion of the FVTX detector has improved vertex measurements leading to improvements in both the invariant yield and the anisotropy analyses. And finally, exploration of an asymmetric heavy ion collision system provides important experimental data to challenge theoretical predictions.

The R_{AA} measurements show systematically increasing suppression with increasingly central collisions. The Au-going direction shows more suppression in the three most peripheral centrality bins, while the Cu-going direction shows more suppression in the most central collisions. The two most peripheral bins for Cu-going and the most peripheral bin for Au-going show enhancement, suggesting that cold nuclear matter effects, particularly

antishadowing, may be a dominant process in these collisions. However, due to the large systematic errors, the measured R_{AA} is also consistent with unity. Meanwhile, the two most central bins show varying levels of suppression. In particular, the ordering of the Cu-going and Au-going directions switches between the two most central bins. It is unclear at which point the hot nuclear matter effects begin to dominate the cold nuclear matter effects, and further, which effects (shadowing or antishadowing...) are the dominant sources. Heavy flavor single muon measurements in Au+Au may serve to help untangle these effects.

The azimuthal anisotropy measurements show a non-zero v_2 for hadrons at forward rapidity, consistant with previous muon arm anisotropy measurements. The heavy flavor v_2 measurements exhibit extremely large error bars, such that the measured v_2 is consistent with both zero and a v_2 which is relatively speaking, rather large. In short, they lack any realistic distinguishing power. The v_3 measurements have even larger uncertainties. In order to make accurate heavy flavor flow measurements, robust statistics are required. This is due to the low signal-to-background ratio in the heavy flavor yield analysis. The signal contributes such a small portion to the inclusive v_2 that it is very dificult to tease it out unless statistical errors are kept at a minimum.

In order to improve these measurements, a wide z-vertex distribution should be collected. This allows the application of a ‘near-side cut’ to reduce the decay muon contribution to the background. Furthermore, a symmetric vertex distribution is essential for precise asymmetry measurements in the forward and backward regions of any asymmetric collision system. Further improvements can be made with high quality data from the FVTX. The separation of charm and beauty remains an attainable, if challenging, goal for PHENIX in the near future. Meanwhile, azimuthal anisotropy measurements can benefit greatly from precision event plane measurements.

Bibliography

- [1] Brennan schaefer quark matter 2015. [ix](#), [30](#)
- [2] Personal correspondance, a. sen. [xvii](#), [136](#)
- [3] Personal correspondance, c. nattrass. [viii](#), [18](#)
- [4] Personal correspondance, s. lim. [xii](#), [72](#)
- [5] *PHENIX recent heavy flavor results*, 2014. [ix](#), [36](#)
- [6] PHENIX Collaboration A. Adare, et al. Cold-nuclear-matter effects on heavy quark production at forward and backward rapidity in d+au collisions at center of mass energy 200 gev. *Physical Review Letters*, 2014. [ix](#), [x](#), [34](#), [35](#), [36](#), [39](#), [120](#), [123](#), [141](#)
- [7] PHENIX Collaboration A. Adare, et al. System-size dependence of open-heavy-flavor production in nucleus-nucleus collisions at center of mass energy 200 gev. *Physical Review C*, 2014. [xvii](#), [132](#), [133](#), [134](#)
- [8] A. Adare et al. Inclusive cross section and double helicity asymmetry for π^0 production in $p + p$ collisions at $\sqrt{s} = 200$ GeV: Implications for the polarized gluon distribution in the proton. *Phys. Rev. D*, 2007. [22](#)
- [9] A. Adare et al. Scaling properties of azimuthal anisotropy in au+au and cu+cu collisions at center of mass energy = 200 gev. *Physical Review Letters*, 98:162301, 2007. [viii](#), [19](#), [20](#)
- [10] A. Adare et al. Heavy-quark production in $p + p$ and energy loss and flow of heavy quarks in au + au collisions at $\sqrt{s_{NN}} = 200$ gev. *Physical Review C*, 84:044905, 2011. [viii](#), [19](#), [20](#), [41](#)
- [11] A. Adare et al. Nuclear modification factor for open heavy-flavor production at forward rapidity in cu+cu collisions at center of mass energy = 200 gev. *Physical Review C*, 86:024909, 2012. [ix](#), [xii](#), [xvi](#), [xvii](#), [24](#), [32](#), [33](#), [34](#), [55](#), [67](#), [74](#), [76](#), [77](#), [78](#), [120](#), [132](#), [133](#), [134](#), [138](#)

- [12] S.S. Adler et al. Centrality dependence of direct photon production in center of mass energy = 200 gev au + au collisions. *Physical Review Letters*, 94:232301, 2005. [viii](#), [15](#), [16](#)
- [13] S. Agostinelli, J. Allison, K. Amako, J. Apostolakis, H. Araujo, P. Arce, M. Asai, D. Axen, S. Banerjee, G. Barrand, F. Behner, L. Bellagamba, J. Boudreau, L. Broglia, A. Brunengo, H. Burkhardt, S. Chauvie, J. Chuma, R. Chytracek, G. Cooperman, G. Cosmo, P. Degtyarenko, A. Dell'Acqua, G. Depaola, D. Dietrich, R. Enami, A. Feliciello, C. Ferguson, H. Fesefeldt, G. Folger, F. Foppiano, A. Forti, S. Garelli, S. Giani, R. Giannitrapani, D. Gibin, J.J. GÁmez Cadenas, I. GonzÁlez, G. Gracia Abril, G. Greeniaus, W. Greiner, V. Grichine, A. Grossheim, S. Guatelli, P. Gumplinger, R. Hamatsu, K. Hashimoto, H. Hasui, A. Heikkinen, A. Howard, V. Ivanchenko, A. Johnson, F.W. Jones, J. Kallenbach, N. Kanaya, M. Kawabata, Y. Kawabata, M. Kawaguti, S. Kelner, P. Kent, A. Kimura, T. Kodama, R. Kokoulin, M. Kossov, H. Kurashige, E. Lamanna, T. LampÁ©n, V. Lara, V. Lefebure, F. Lei, M. Liendl, W. Lockman, F. Longo, S. Magni, M. Maire, E. Medernach, K. Minamimoto, P. Mora de Freitas, Y. Morita, K. Murakami, M. Nagamatu, R. Nartallo, P. Nieminen, T. Nishimura, K. Ohtsubo, M. Okamura, S. O'Neale, Y. Oohata, K. Paech, J. Perl, A. Pfeiffer, M.G. Pia, F. Ranjard, A. Rybin, S. Sadilov, E. Di Salvo, G. Santin, T. Sasaki, N. Savvas, Y. Sawada, S. Scherer, S. Sei, V. Sirotenko, D. Smith, N. Starkov, H. Stoecker, J. Sulkimo, M. Takahata, S. Tanaka, E. Tcherniaev, E. Safai Tehrani, M. Tropeano, P. Truscott, H. Uno, L. Urban, P. Urban, M. Verderi, A. Walkden, W. Wander, H. Weber, J.P. Wellisch, T. Wenaus, D.C. Williams, D. Wright, T. Yamada, H. Yoshida, and D. Zschiesche. Geant4 simulation toolkit. *Nuclear Instruments and Methods in Physics Research Section A: Accelerators, Spectrometers, Detectors and Associated Equipment*, 506(3):250–303, 2003. [81](#), [87](#)
- [14] Aitchison and Hey. *Gauge Theories in Particle Physics, Volume 1: From Relativistic Quantum Mechanics to QED*. CRC Press, 2002. [4](#)
- [15] S.A. Voloshin A.M. Poskanzer. Methods for analyzing anisotropic flow in relativistic nuclear collisions. *Physics Review C*, C58(1671), 1998. [94](#), [97](#), [98](#), [100](#)

- [16] Siegfried Bethke. The 2009 world average of alpha, 2009. [viii](#), [5](#), [6](#)
- [17] J. Bok. Prompt muon elliptic flow in au+au 200 gev. Analysis Note 670. [97](#)
- [18] Sophie Bushwick. How low can rhic go, July 2010. [viii](#), [8](#)
- [19] ALICE Collaboration. Heavy-flavour decay muon v2 in pb–pb collisions. *Nuclear Physics A*, 931:530–534, 2014. [xi](#), [xvii](#), [43](#), [45](#), [140](#)
- [20] PHENIX Collaboration. [52](#)
- [21] PHENIX Collaboration. Measurement of single electron event anisotropy in au+au collisions at center of mass energy 200 gev. *Physical Review C*, 2005. [x](#), [40](#), [41](#), [42](#)
- [22] PHENIX Collaboration. Measurement of high-pt single electrons from heavy-flavor decays in p+p collisions at center-of-mass energy 200 gev. *Physical Review Letters*, 2006. [ix](#), [23](#)
- [23] PHENIX Collaboration. J/psi production in center of mass energy 200 gev cu+cu collisions. *Physical Review Letters*, 2008. [x](#), [36](#), [37](#), [38](#)
- [24] PHENIX Collaboration. Nuclear matter effects on j/psi production in asymmetric cu+au collisons at center of mass energy 200 gev. *Physical Review C*, 2014. [x](#), [39](#), [40](#), [115](#)
- [25] PHENIX Collaboration, 2017. [xi](#), [48](#)
- [26] B.L. Combridge et al. Associated production of heavy flavor states in pp and p anti-p interactions: Some qcd estimates. *Nuclear Physics B*, 151:429–456, 1979. [21](#)
- [27] Wikipedia contributors, June 2017. [viii](#), [3](#)
- [28] Irakli Garishvili. *Open Heavy Flavor Measurement at Forward Angles for Cu + Cu Collisions at Center of Mass NN Collisions Energy 200 GeV*. PhD thesis, University of Tennessee, 2009. [xi](#), [32](#), [56](#), [115](#)
- [29] M. Gyulassy. The qgp discovered at rhic, 2004. [13](#), [16](#)

- [30] Henrik Bohr H.B. Nielsen. Hadronic production from a boiling quark soup. *Nuclear Physics B*, 128(2):275–293, Spetember 1977. [31](#)
- [31] Donald Hornback. *A measurement of open charm using single muons at forward angles for p+p collisions at center of mass energy 200 GeV*. PhD thesis, University of Tennessee, 2008. [ix](#), [xi](#), [xii](#), [25](#), [32](#), [46](#), [64](#), [76](#), [88](#), [115](#)
- [32] Maggie Jezghani. *Measurement of Phi Meson Production and Nuclear Modification In Cu+Au Collisions at Center-Of-Mass Energy 200 GeV With The Phenix Detector at RHIC*. PhD thesis, Georgia Staate University, 2015. [xi](#), [58](#), [115](#)
- [33] PHENIX Collaboration K. Adcox, et al. Measurement of single electrons and implications for charm production in au+au collisions at center of mass energy 130 gev. *Physical Review Letters*, 2002. [31](#)
- [34] Frithjof Karsch. Lattice qcd at high temperature and density. arXiv:hep-lat/0106019, 2001. [viii](#), [7](#), [9](#)
- [35] H. Paukkunen K.J. Eskola and C.A. Salgado. Eps09 - a new generation of nlo and lo nuclear parton distribution functions. *Journal of High Energy Physics*, 2009, 2009. [viii](#), [11](#), [12](#)
- [36] Sanghoon Lim. *The measurement of nuclear modi cation factor RdA of single muons from open heavy- avor in d+Au collisions at center-of-mass energy 200 GeV*. PhD thesis, Yonsei University, 2014. [86](#), [112](#), [115](#), [116](#)
- [37] Michael R. Lomnitz. Measurement of d-meson azimuthal anisotropy in au+au 200 gev collisions at rhic. *arXiv:1601.00743v1*, 2016. [x](#), [41](#), [42](#)
- [38] Mike McCumber. *Measurement of Fast Parton Interactions with Hot Dense Nuclear Matter via Two-Particle Correlations at PHENIX*. PhD thesis, University of Colorado, 2009. [13](#)
- [39] L. McLerran. A brief introduction to the color glass condensate and glasma, 2008. [10](#)

- [40] Michael Miller, Klaus Reygers, Stephen Sanders, and Peter Steinberg. Glauber modeling in high energy nuclear collisions. *Annual Review of Nuclear and Particle Science*, 57:205–243, 2007. [xi](#), [10](#), [59](#), [60](#)
- [41] D. Molnar and M. Gyulassy. Saturation of elliptic flow and the transport opacity of the gluon plasma at rhic. *Nuclear Physics A*, 697, 2001. [13](#)
- [42] James Nagle and Berndt Muller. Results from the relativistic heavy ion collider. *Annual Review of Nuclear and Particle Science*, 56:93–135, 2006. [21](#), [22](#), [24](#)
- [43] Hiroshi Nakagomi. Personal correspondance, h. nakagomi. [xiii](#), [100](#)
- [44] Nobelprize.org. The nobel prize in physics 1990, October 2015. [4](#)
- [45] K.A. Olive et al. The review of particle physics. *Chin. Phys.*, C38, 2014. [7](#)
- [46] PHENIX. Proposal for a forward silicon vertex tracker (fvtx) for the phenix experiment. 2007. [56](#), [57](#)
- [47] Ringaile Placakyte. Parton distribution functions, 2011. [viii](#), [11](#), [12](#)
- [48] I. Vitev R. Sharma and B. Zhang. A light-cone wavefunction approach to open heavy flavor dynamics in qcd matter. *Physical Review C*, 2009. [xvii](#), [138](#), [139](#)
- [49] Eric Richardson. *Elliptic Flow at Forward Rapidity in Center-Of-Mass 200 GeV Au+Au Collisions*. PhD thesis, University of Maryland, 2012. [xiv](#), [94](#), [119](#), [139](#)
- [50] Satz Sarkar and Sinha, editors. *The Physics of the Quark-Gluon Plasma: Introductory Lectures*. Springer, 2010. [15](#)
- [51] Brennan Schaefer. *Measurements of directed, elliptic, and triangular flow of charged hadrons from Cu+Au collisions at center of mass energy 200 GeV with PHENIX at RHIC*. PhD thesis, Vanderbilt University, 2016. [x](#), [43](#), [44](#)
- [52] Brandon Kyle Schmoll. Pythia8 study concerning muon/d meson momentum correlations. Analysis Note 1009 for PHENIX, 2012. [ix](#), [27](#)

- [53] PHENIX Collaboration S.S. Adler, et al. Measurement of single muons at forward rapidity in p+p collisions at center of mass energy 200 gev and implications for charm production. *Phys. Rev. D*, 2006. [ix](#), [31](#), [32](#)
- [54] R. Thomas, B. Kampfer, and G. Soff. Gluon emission of heavy quarks: Dead cone effect. *Acta Physica Hungarica A*, 22:83–91, 2005. [23](#)
- [55] S. Voloshin and Y. Zhang. Flow study in relativistic nuclear collisions by fourier expansion of azimuthal particle distributions. *Z. Phys.*, C70, 1996. [96](#)
- [56] X.R. Wang. Prompt muons measurement in dau collisions at center-of-mass energy 200 gev at rhic. Analysis Note 412. [ix](#), [28](#), [29](#)
- [57] Matthew Wysocki. *J/Psi Production and Suppression in Au+Au collisions at center-of-mass energy 200 GeV*. PhD thesis, University of Colorado, 2011. [viii](#), [xi](#), [xii](#), [9](#), [10](#), [52](#), [64](#), [65](#), [69](#)

Appendices

Appendix A

Selected Data Tables

Table A.1: Table for Figure 7.1 (centrality 0%–20%)

Arm	p_T (GeV)	Yield	Stat. Error (%)	Sys. Error (%)
South	1.1259	0.00101857	0.0586936	0.704903
	1.3666	0.000364802	0.0503593	0.587715
	1.61146	0.000163145	0.0409315	0.370265
	1.85966	6.55133e-05	0.0452631	0.315276
	2.1099	3.13314e-05	0.0463172	0.250136
	2.36096	1.37897e-05	0.0484794	0.217108
	2.61109	6.77774e-06	0.0648918	0.211521
	2.86256	3.0931e-06	0.0732461	0.198636
	3.20249	1.34048e-06	0.0563769	0.181327
	3.70543	4.02762e-07	0.073171	0.16883
North	4.3662	7.60331e-08	0.0947106	0.163311
	1.12942	0.00126577	0.0431832	0.195451
	1.36892	0.000375382	0.0433532	0.161822
	1.61298	0.000119798	0.0542537	0.155035
	1.86037	4.16879e-05	0.0781298	0.157963
	2.1101	1.68532e-05	0.0906893	0.150573
	2.36095	7.73898e-06	0.124738	0.215244
	2.61125	3.21605e-06	0.134354	0.442168
	2.86252	1.99737e-06	0.134277	0.527817
	3.2042	4.27952e-07	0.486216	1.59909
	3.71174	2.10108e-07	0.190715	1.25622
	4.37085	2.1775e-08	0.685767	3.79583

Table A.2: Table for Figure 7.2 (centrality 20%–40%)

Arm	p_T (GeV)	Yield	Stat. Error (%)	Sys. Error (%)
South	1.12664	0.000980633	0.0289208	0.210984
	1.36681	0.0002988	0.0309256	0.272083
	1.61196	9.2436e-05	0.0429821	0.361509
	1.86049	2.86077e-05	0.0641604	0.45246
	2.11015	1.13032e-05	0.0867019	0.497313
	2.36038	5.4669e-06	0.0928374	0.417997
	2.61303	2.24947e-06	0.127076	0.476002
	2.86271	1.31293e-06	0.118138	0.361841
	3.20084	6.03087e-07	0.0977444	0.309223
	3.70462	1.91047e-07	0.121139	0.312148
North	4.34588	3.20059e-08	0.178996	0.416008
	1.12972	0.000937918	0.0318735	0.15018
	1.36884	0.000279477	0.0330663	0.15186
	1.61306	8.67698e-05	0.0436428	0.161056
	1.86056	3.91556e-05	0.0434696	0.152731
	2.11123	1.72828e-05	0.0485076	0.150005
	2.36109	8.12377e-06	0.053358	0.15001
	2.61178	4.08761e-06	0.0550269	0.150002
	2.86164	2.41077e-06	0.0653804	0.150289
	3.20346	9.3122e-07	0.0516156	0.151438
	3.69953	2.60437e-07	0.0766713	0.153779
	4.35271	4.26639e-08	0.21464	0.155757

Table A.3: Table for Figure 7.3 (centrality 40%–60%)

Arm	p_T (GeV)	Yield	Stat. Error (%)	Sys. Error (%)
South	1.1266	0.000255571	0.053747	0.32393
	1.36747	7.65843e-05	0.0565414	0.427933
	1.61174	2.63049e-05	0.0658719	0.522754
	1.86068	9.60653e-06	0.0818991	0.591768
	2.11108	4.7729e-06	0.0835601	0.516733
	2.36089	2.15445e-06	0.0943351	0.492092
	2.61273	9.89396e-07	0.125944	0.543411
	2.86335	4.66766e-07	0.15751	0.528861
	3.20734	2.23354e-07	0.127375	0.433856
	3.70141	5.4966e-08	0.601047	0.707831
North	4.34552	1.15664e-08	0.271459	0.491859
	1.1302	0.000438853	0.0234221	0.154371
	1.36911	0.000134129	0.0241954	0.162334
	1.61362	4.77918e-05	0.0277752	0.169329
	1.86102	2.00694e-05	0.0303998	0.164338
	2.11121	9.0167e-06	0.0332936	0.157041
	2.36146	4.19826e-06	0.0414216	0.151842
	2.61389	2.07086e-06	0.0438511	0.150028
	2.86321	1.1367e-06	0.049813	0.150453
	3.20852	4.1735e-07	0.0564934	0.151051
	3.70299	8.78561e-08	0.186434	0.151117
	4.35212	2.77456e-08	0.127856	0.152226

Table A.4: Table for Figure 7.4 (centrality 60%–100%)

Arm	p_T (GeV)	Yield	Stat. Error (%)	Sys. Error (%)
South	1.12621	6.4589e-05	0.0535856	0.168958
	1.36628	2.16795e-05	0.0498071	0.206113
	1.61214	8.24114e-06	0.050288	0.259988
	1.86044	2.86704e-06	0.0691152	0.348641
	2.11168	1.36122e-06	0.0781234	0.356918
	2.35949	6.69344e-07	0.0855769	0.30292
	2.60874	3.31227e-07	0.107313	0.285472
	2.86076	1.81933e-07	0.114995	0.22877
	3.21164	7.41372e-08	0.117435	0.212977
	3.72138	2.71092e-08	0.15358	0.211044
North	4.34583	2.84328e-09	0.367305	0.494381
	1.12911	0.000105398	0.0301232	0.150202
	1.37006	3.17112e-05	0.0310774	0.150626
	1.61381	1.11612e-05	0.0363637	0.155072
	1.86053	4.83289e-06	0.039991	0.154855
	2.11148	2.24423e-06	0.0454796	0.153256
	2.3609	9.1391e-07	0.0632528	0.150996
	2.61047	4.30881e-07	0.0831019	0.150118
	2.86327	2.52463e-07	0.0862366	0.152115
	3.2083	9.83979e-08	0.0955652	0.159879
	3.6909	2.33688e-08	0.175379	0.183595
	4.37106	6.09692e-09	0.227214	0.190678

Vita

Brandon Kyle Schmoll was born on June 7, 1985 in Atlanta, GA. He spent most of his youth growing up in Winthrop, MA where he graduated from high school in May 2003. Brandon attended the University of Massachusetts, Amherst, starting in September of 2003, completing his B.S. in Physics in May of 2009. He then spent a year working for Professor Andrea Pocar at UMass as a research assistant, where he would work on the EXO200 experiment in Carlsbad, NM.

In June 2010, Brandon moved to Knoxville to begin his graduate studies at the University of Tennessee. In his first year, he joined the Relativistic Heavy Ion Physics (RHIP) group and began his doctoral research within the PHENIX experiment under Dr. Kenneth Read's supervision. Brandon completed his Ph. D. dissertation in June of 2017. Shortly after, Brandon moved back to Massachusetts to take a job in software engineering.